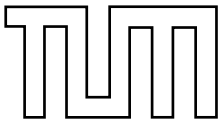

Fakultät für Informatik
Technische Universität München

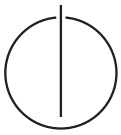

Visualization modes for CT-fluoroscopy guided RF liver ablation

Ruxandra Lasowski

Dissertation

Technische Universität München
Lehrstuhl für Informatikanwendungen

Visualization modes for CT-fluoroscopy guided RF liver ablations

Ruxandra Lasowski

Vollständiger Abdruck der von der Fakultät für Informatik der Technischen Universität München zur Erlangung des akademischen Grades eines

Doktors der Naturwissenschaften (Dr. rer. nat.)

genehmigten Dissertation.

Vorsitzender:	Univ.-Prof. G. J. Klinker, Ph.D.
Prüfer der Dissertation:	
1.	Univ.-Prof. N. Navab, Ph.D.
2.	apl. Prof. Dr. H.-P. Meinzer, Ruprecht-Karls Universität Heidelberg

Die Dissertation wurde am 31.03.2008 bei der Technischen Universität München eingereicht und durch die Fakultät für Informatik am 07.10.2008 angenommen.

Abstract

Radiofrequency ablation of the liver is a minimally-invasive procedure used for patients with lesions unsuitable for surgical resection. The intra-interventional 2D image guidance does not provide all important anatomical information to the interventional radiologist for insertion and positioning of the needle. Therefore, incorporation of additional pre-interventional 3D data, would improve the needle guidance.

The central aspect of this thesis is an optimized visualization of pre-interventional CT data based on CT-fluoroscopy (CT-fluoro) slices acquired during the intervention.

Three different visualization modes are developed to cope with the uncertainty in estimating the liver deformation caused by breathing. For this purpose, we apply the animation concept used in uncertainty visualization. We first introduce a subvolume visualization based on piecewise slice-to-volume registration. In the sequel, a sampling method on isosurfaces in the convergence basin of the employed cost function is used to retrieve the motion parameters which define the subvolume. In our last approach, the motion parameters are optimized to display a trajectory path along the 'valley floor' of the employed cost function. The last two modes address the visualization of the fuzzy or flat area of the cost function providing potential solutions.

These novel visualization modes based on a combination of rigid registration and adaptive visualization, allow for a better spatial orientation and neighborhood assessment of critical structures whilst performing the needle insertion.

The thesis also presents evaluations of the proposed visualizations by experienced interventional radiologists.

Keywords:
Visualization, Uncertainty Visualization, Slice-to-Volume Registration, abdominal Procedures, Interventions, RF ablation, Liver

Zusammenfassung

Die perkutane Radiofrequenz Ablation (RFA) der Leber ist eine interventionelle Methode für Patienten mit nicht-resezierbaren primären Lebertumoren oder Lebermetastasen. Die intra-interventionelle 2D-Bildgebung stellt nicht alle wichtigen anatomischen Informationen bereit, welche der Radiologe während einer Intervention braucht. Daher würden zusätzlich vorhandene 3D prä-interventionelle Daten die Nadelführung und Positionierung entscheidened verbessern.

Der zentrale Aspekt dieser Arbeit ist eine optimierte Visualisierung des CT-Volumens basierend auf intra-interventionellen aufgenommenen CT-Fluoroskopie (CT-Fluoro) Schichten.

Drei verschiedene Visualisierungsmodi werden in der Dissertation vorgestellt, welche die Unsicherheit der Leberdeformierung abschätzen können. Hierfür setzen wir das Konzept der Animation ein, das in der Visualisierung von Unsicherheit verwendet wird. Zuerst stellen wir eine Subvolumen Visualisierung basierend auf der stückweisen Registrierung der CT-Fluoro Schicht zum Volumen vor. Im Folgenden, basierend auf der Strukturanalyse der verwendeten Kostenfunktion, wird eine Sampling-Methode auf Isoflächen vorgestellt um die Bewegungsparameter, die das Subvolumen definieren, zu bestimmen. Im letzten Ansatz werden die Bewegungsparameter optimiert um eine Trajektorie entlang der Talsohle der Kostenfunktion anzuzeigen. Ziel der letzten zwei Visualisierungsmodi ist eine Visualisierung der 'fuzzy' oder flachen Bereiche der Kostenfunktion um in Frage kommende Lösungen zu präsentieren.

Diese neuen Visualisierungmodi basierend auf einer Kombination rigider Registrierung und adaptiver Visualisierung ermöglichen eine bessere Orientierung sowie eine Nachbarschaftsbeurteilung kritischer Strukturen während der Intervention.

Ausserdem werden in dieser Arbeit auch Evaluierungen der vorgeschlagenen Visualisierungsmodi präsentiert, die zusammen mit erfahrenen Radiologen erstellt wurden.

Schlagwörter:
Visualisierung, Visualisierung von Unsicherheit, stückweise Registrierung, Schicht zum Volumen Registrierung, abdominelle Prozeduren, Interventionen, RF Ablation, Leber

ACKNOWLEDGMENTS

The first person I would like to thank is Professor Nassir Navab who integrated me as an external PhD student in his group. Professor Navab and his group create a very fruitful environment at the TUM which always inspired me with ideas for my thesis. I thank Professor Navab for his guidance, his great ideas and his enthusiasm.

I thank Wolfgang Wein whose 2D-3D registration modules have provided the starting point and the basis for my work. Darko Zikic and Martin Urschler have provided the deformed ground-truth volume data which I am thankful for. My thanks also to Jakob Vogel for his performance as an assisting student working within his interdisciplinary project also with the math department of Professor Brokate. Many thanks to Professor Brokate and Christian Clason for their support and contributions.

It was a great pleasure to work with Selim Benhimane. I thank him for his math guidance and ideas that contributed a lot to my thesis.

Special thanks to Stefanie Demirci for her useful remarks and for the proofreading of my thesis.

I thank Siemens Medical Solutions for funding the research, in particular Dr. Rainer Graumann, Daniel Rinck, Dr. Michael Sühling and all my colleagues there, specially the other PhD students: Jan, Jens, Ulrike, Arne.

I very much enjoined the evaluations with our medical partners Tobias F. Jakobs (who's black humor always added a new perspective on a serious matter), Christoph J. Zech, and Christoph Trumm in the Klinikum Grosshadern.

I am deeply indebted to Verena Grail for her long friendship and for hosting me during my visits to Munich. Also for her hospitality I would like to thank Stefanie Demirci again.

I am very grateful to my mother Mihaela Eleonora Micu who strongly supported the idea of starting a PhD after four years of work in the industry. Unfortunately, my father Moise Micu could not live as long for seeing me graduating. And I am also very grateful for my awesome husband Ophir. His love, humor, black humor, support and surprises make me a happy person.

CONTENTS

Part I.

Introduction

CHAPTER

ONE

MOTIVATION

1.1. Radiofrequency Liver Ablation

RADIOFREQUENCY Ablation (RFA) [90] of the liver is an interventional procedure applied to patients with unresectable primary liver tumors (HCC - hepatocellular carcinoma) and metastases. This procedure involves the percutaneous insertion of needle-like electrodes into the lesion. Through the needle electrodes, an electrical current is then applied to the tumor, heating the tissue to temperatures over 50 degrees and leading to its destruction. The procedure is very attractive due it's minimal invasive nature, causing less complication risks. However, its success is depending on an accurate placement of the needle which is crucial for a precise distribution of heat throughout the tumor and an effective thermal coagulation necrosis procedure. Moreover, the existence of big arteries or veins next to the tumors should also be considered as it requires longer ablation due to a cooling effect of the blood-flow.

Different imaging systems like iMRI, Ultrasound, CT or CT fluoroscopy (CT-fluoro), [37, 34] are used to guide the insertion and positioning of the needle.

Each guidance system has its own advantages and drawbacks. The biggest advantage of performing a liver ablation under iMRI guidance is the use of non ionizing radiation. Not only that it is safe for patient and radiologist but also makes it possible to visualize the thermal distribution allowing to check whether the entire lesion was captured by the ablation procedure. Yet, special materials needed to be used in order not to interact with the magnetic field, make the use of this modality the most expensive. Moreover, the quality of the images are lower than standard MRI due to employment of low field magnets. A setup under iMRI for interventions for an open magnet design is shown in 1.3. A recently introduced MRI system provides better access to the patient through a bigger bore (see figure 1.3(c)).

The ultrasound (US) imaging modality provides a less expensive alternative solution for RF liver ablation and has the ability to provide images from different angles. However, its main disadvantage is the degradation of the generated images, caused by air bubbles which are created during the heating of the tissue.

CT and CT-fluoro have the common main drawback of ionizing radiation. In

contrast to CT, CT-fluoro is a relatively new data acquisition mode for the CT scanner that allows rapid image reconstruction and in-room image viewing during CT-guided interventional procedures. In order to reduce the radiation exposure especially for the physician, a lower dose is employed which results in a noisy CT-fluoro image. A technical review of image-guided procedures can be found in [132].

A setup of an intervention under CT-fluoro guidance is shown in figure 1.2.

(a) (b)

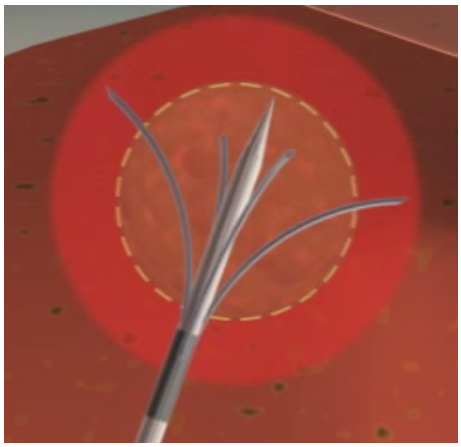

(c)

Figure 1.1.: RF equipment (courtesy of RITA Medical Systems): (a) Generator (b) Needle with temperature simulation along the electrode tips. The longer electrodes provide a $1cm$ safety margin for eliminating microscopic lesions.

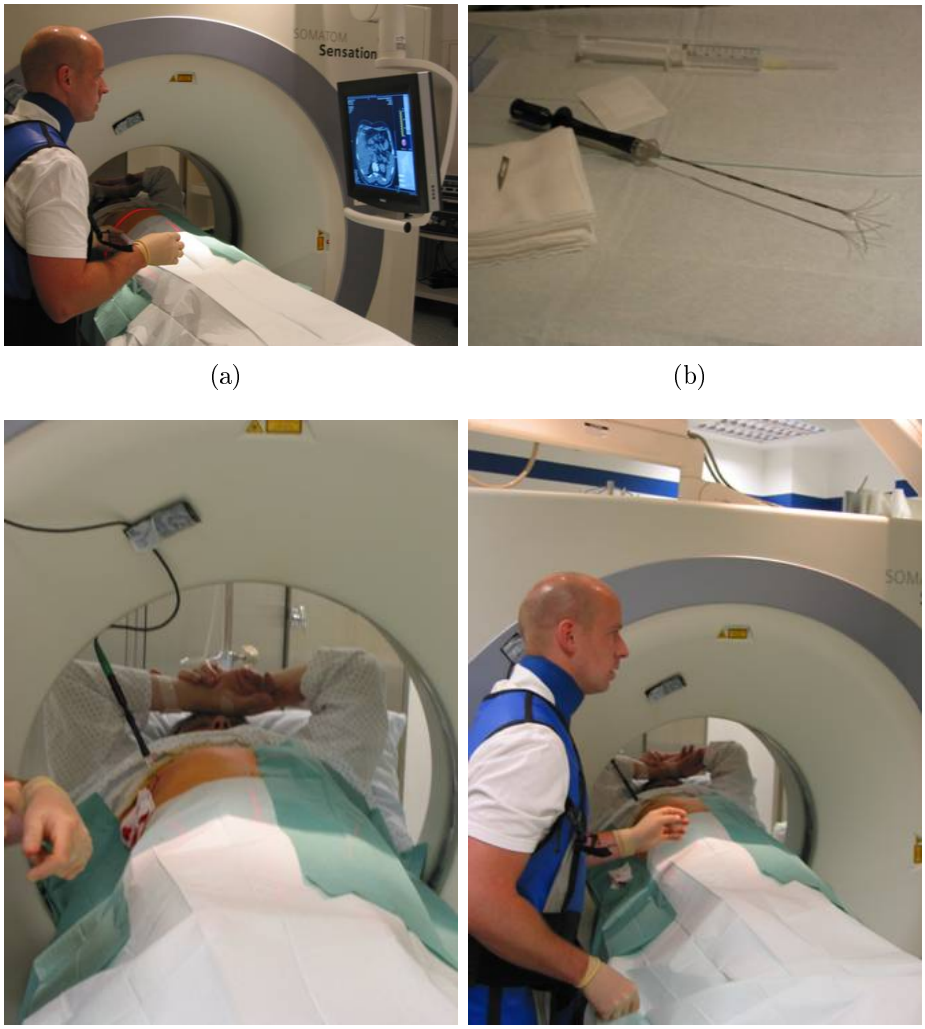

(a) (b)

(c) (d)

Figure 1.2.: Intervention setup (CT-fluoro guided): (a) Interventional radiologist, CT-fluoro image display and patient lying on the CT table. (b) Needle after extension (RITA Medical Systems). (c) During RF ablation. (d) CT-fluoro acquisitions (with foot pedal).

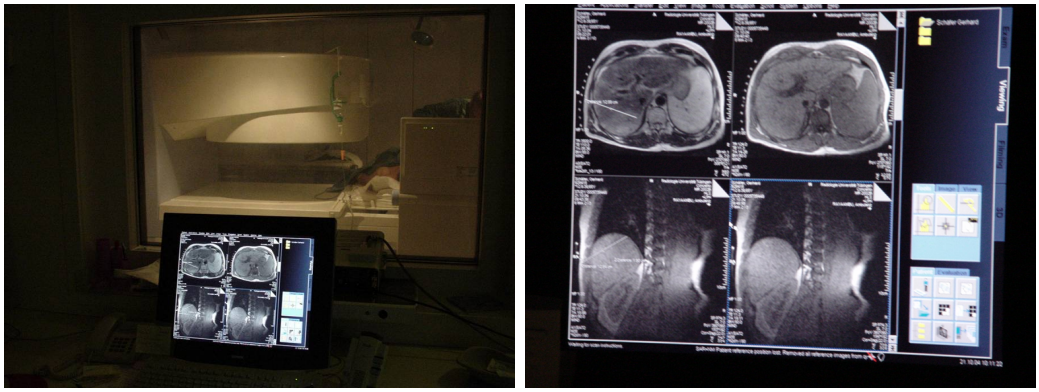

(a) (b)

(c)

Figure 1.3.: Setup of an intervention under iMRI guidance. (a) Magnetom Open, Siemens Medical Solutions, Erlangen, Germany. The MR scanner has an open magnet design where the access to the patient is from the side. (b) Planning on the workstation for trajectory path. (c) Magnetom Espree, Siemens Medical Solutions. New generation of MRI machine with a bigger bore to enable better patient access.

1.1.1. Workflow of Liver Ablation under CT-fluoro Guidance

We are analyzing the workflow of RF liver ablation under CT-Fluoro guidance, as performed by our clinical partners. First, a high resolution contrasted CT-volume data of the patient's liver is being acquired. The choice of cardiovascular phase depends on the type of tumor; HCC, breast cancer metastases, and renal cell carcinoma metastases are better visualized in the arterial phase, while for all other metastases, the venous phase is preferred. Based on this actual data, a rough planning of the needle insertion is performed[1]. The following stage of needle insertion is then performed using real-time CT-fluoro images which are generated with lower dose. At this stage, the attending interventional radiologist is required to register the volume in his mind, accounting for the liver contour, ligamentum falciforme, spleen, gallbladder or other patient specific anatomical landmarks, e.g. calcifications and previously introduced surgical clips. CT-fluoro images do not display all anatomical information contained by the pre-interventional volume data. The interventional radiologist only guesses where the actual needle position is placed in the pre-interventional volume. Since the needle trajectory is not always in-plane, only a small part of the needle is visible. The latter fact and the breathing motion pose additional difficulties to the interventional radiologists. The current set-up forces the interventional radiologists to leave the intervention room whenever they need to consult the pre-interventional volume. The data is usually accessible at separated workstations that are located outside the intervention room. Even if the volume is present on a second monitor throughout the intervention, only a registration between the interventional CT-fluoro slice and the pre-interventional volume would spare the search through the volume of the interventional radiologist. For that purpose, we are aiming at developing an interface of triggering an automatic registration process and presenting a high quality subvolume of the pre-interventional CT-volume in the intervention room. In addition, the table must often be lowered during the insertion in order to provide access for the needle insertion. Augmentation of the 'Field of View' (FOV) is performed to have better visibility in the CT-fluoro slice. All these changes need to be taken into account for a better initialization of the registration process. As last stage of the workflow, a post-contrast CT data is acquired after the ablation to assess the necrosis. A scheme of the workflow is shown below in figure 1.4.

1.2. Problem Statement

Our entry point in the current workflow (see figure 1.4) is the needle insertion task. We are investigating the registration of one CT-fluoro slice with the pre-interventional CT data-set (volume). Since the liver moves and deforms with the breathing, a non-rigid registration would be appropriate. However, to perform a deformable registration only based on the CT-volume and one slice without incor-

[1] Recent works of Kröger et al. [59] target to help the planning by simulating a trajectory of the needle with optimal heat dispersion

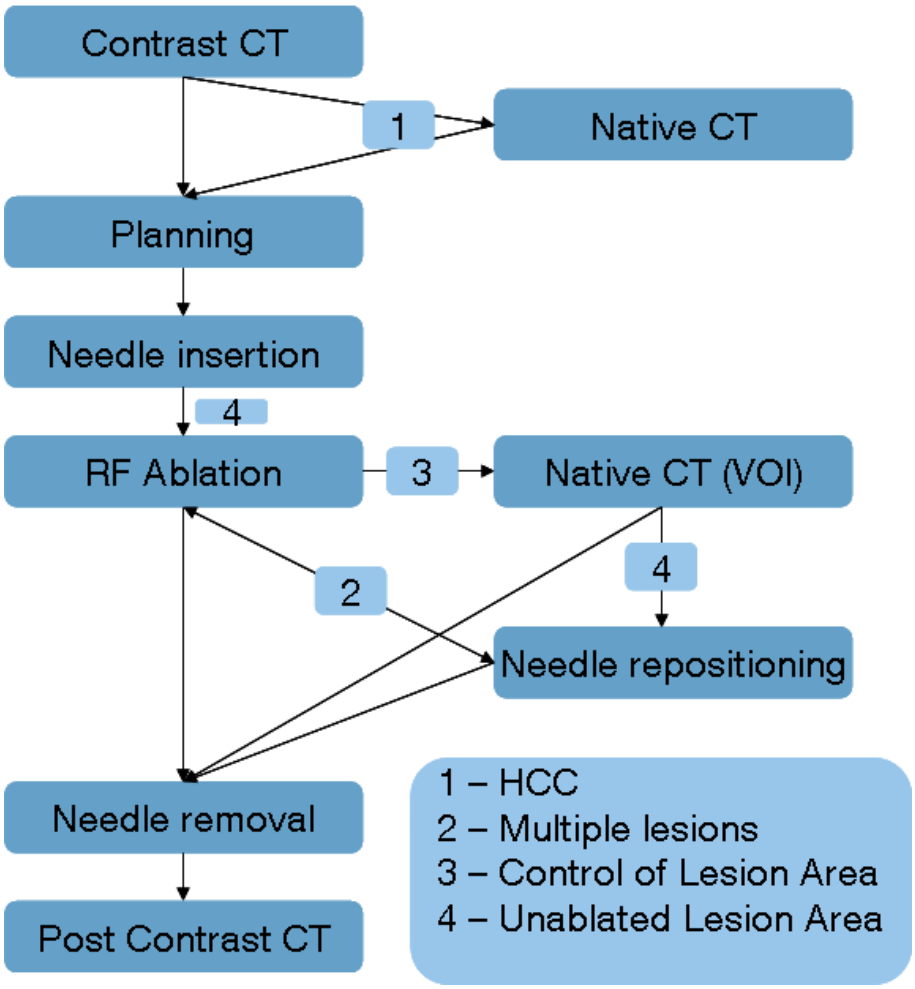

Figure 1.4.: Current workflow performed by our clinical partners for the CT-fluoro guided liver ablation.

porating any prior knowledge and present one deformed slice as a solution in the intervention room, is, for this application, very hard to achieve.

The reasons for this ill-posedness are listed below:

1. RFA is performed while the patient is breathing continuously, whereas the pre-interventional CT-volume is usually acquired during deep inspiration.Only in this breathing stage the pleura cavity can be appreciated to its full extension. Also, the patient can hold his breath for the imaging procedure more easily. Breathing instructions during the intervention are common. Once the needle is inserted into the target lesion, breathing is usually impaired due to moderate pain and/or psychological reasons. A review regarding liver motion and deformation due to respiration is published in [21, 9].

2. CT-fluoro slices have a lower signal-to-noise ratio compared to pre-interventional CT data due to the lower radiation dose applied (e.g. $59mA$ in Fluoro mode,

$260mA$ for diagnostic scan).

3. A single CT-fluoro slice provides much less information than an entire CT-volume. Furthermore it is thicker($4mm$ or $6mm$) than pre-interventional CT data ($3mm$ or $1mm$).

4. The only anatomical features that could be used for liver registration are the vessels. These are only seen in the contrast-enhanced pre-interventional CT scan. Neither intrahepatic vessels nor metastases can be appreciated using CT-fluoro slices. Since primary liver cancer (HCC) is usually pretreated using transarterial chemoembolization (TACE), the used radiopaque embolic agent can be visualized in the non-enhanced CT-fluoro scan.

5. Definitions of 'most similar' slices in the pre-interventional CT-volume by two experienced interventional radiologists showed that there is an inter-observer variance between the slices. This is expected since the deformation makes it impossible to have a single deterministic solution.

6. Registration needs to be done in real time.

Commercial solutions for needle guidance in abdominal interventions do not exist. A previously existing system CT-Guide 1010 (Ultraguide, Tirat Hacarmel, Israel) was retreated from the market. The system provided virtual navigation through electro-magnetic tracking of the needle and respiratory gating. Evaluations of the system as described in [50] showed that the accuracy was $2.2 \pm 2.1mm$ in 50 procedures. But higher deviations at the order of $20mm$ also occurred due to agitated or stronger breathing. Because of the real-time nature of the procedures, most systems assume rigidity which does not hold without a strict breathing gating technique or intubation. Intubation is very seldomly employed during RFA and only when medical indication is required. Strict gating techniques did not prove to be reliable in all cases either [6, 50]. The proposed non-rigid registrations mentioned above [8] are still under development due to the unsolved validation and huge time they require for calculations.

We believe that a visualization coping with the uncertainty introduced by the deformation and displaying slices of the volume without deforming the data, could be an alternative solution to a deformable slice-to-volume registration. We find that among the techniques of uncertainty visualization the animation is the most suitable for our application.

1.3. Contributions

In order to support the RF liver ablation procedure under CT-fluoro guidance, we target on displaying contrasted high resolution data corresponding to the actual CT-fluoro slice in the intervention room. This thesis proposes new optimized visualization modes for CT data based on interventionally acquired CT-fluoro slices.

The combination of registration and appropriate visualization provides a solution for the ill-posed deformable slice-to-volume registration. Three different visualization modes are developed that cope with the uncertainty in estimating the deformation. The modes consist in automatically displaying a subvolume next to the CT-fluoro slice in an animated sequence. The trajectory waypoints and their traversal in the CT-volume are optimized to allow for displaying only relevant information of the CT-fluoro slice. Furthermore, we provide a user interface to interact with the animation and to manually navigate through the resulting subvolume. We evaluate our proposed solutions on realistic synthetic slices constructed from patient data.

- The first contribution features a piecewise registration of the liver to detect for each piece the most corresponding slice in the entire CT-volume for each part of the liver, respectively [74, 75]. Starting with dividing the liver into its dorsal and ventral part in the first stage, we then increase the partition to six parts for better estimating the deformation. Since the visualization of a subvolume defined by more than two slices could cause perception difficulties to the interventional radiologists who are used to axial slices, we have also presented alternative visualization modes for comparison. A detailed presentation of this method is given in chapter 3.

- In the following, we address the definition of a set of solutions based on analysis of the cost surface in the convergence basin of the registration result [62, 61]. In this neighborhood, out-of-plane motion parameters samples, located on the isosurfaces of the minimized cost function are found using a line search strategy. This set of solutions will increase the confidence in the result and allows a smooth neighborhood exploration. The resulting volume takes into account in which projection parameters the registration is most sensitive. The method is presented in detail in chapter 4.

- Last but not least, similar to the previous approach, starting from the registration result, a trajectory along the valley floor of the cost surface is calculated. By moving along this trajectory, we capture the parameters for which the change in the similarity measure is minimal, i.e. the parameters which impose most uncertainty when searching for a solution in the CT-volume. In order to find this valley, we adapt algorithms from computational chemistry, as well as a newly developed adaptive eigenvector step method. The method is presented in detail in chapter 5.

All approaches are evaluated on synthetic CT-fluoro slices derived from patient data. Routinely acquired CT-fluoro slices are used for evaluation and assessment by experienced interventional radiologists.

The visualization of a subvolume in the pre-interventional volume brings much more intuitive information to the interventional radiologist than one single slice. This information includes the vessels as well as lesion spread and distribution. The needle guidance toward the lesion is therefore improved. In addition, this could result in less radiation dose for the patient and examiner.

CHAPTER

TWO

STATE OF THE ART

2.1. Slice-to-Volume Registration

In order to show anatomy which is only visible in the high quality pre-interventional acquired volume, the image slices acquired during the intervention must be related to the pre-interventional volume through a slice-to-volume registration. As stated in [5, 6, 17], slice-to-volume registration is different than 2D-3D registration [89, 88, 46, 126]. The X-ray projection images represent each the 2D image. The digitally rendered radiographs (DRR), generated via ray-casting or light fields [104] from the 3D CT-volume, are compared with the 2D projection image[1] for the 2D-3D registration. Procedures of the slice-to-volume category utilize several image-guidance workflows. Detailed analysis of iMRI/MRI are given in [29], US/MRI in [87, 8], US/CT in [127, 128], CT/CT in [80], CT-fluoro/CT in [130, 131, 6, 5, 133].

2.1.1. Intensity-based rigid Slice-to-Volume Registration

In [130], piecewise slice-to-volume registration is used to infer the location of the target lesion into the CT-fluoro image for robotically assisted lung biopsy. The tracking of circular sections is based on the tracking of the lung texture, the bronchi, and vessels. In [131], the same registration is used for reconstruction of a 4D CT lung and deformation estimation for respiration motion compensation.

In [29], rigid slice-to-volume registration is applied to align iMRI interventional slices to a pre-interventional MRI volume for radiofrequency ablation of prostate cancer. Different cost functions are used at different resolutions. Sufficiently accurate results are achieved for transversal slice acquisitions in order to aid image-guided therapy.

In [6], the authors compare different similarity measures for registering CT-fluoro to CT. The cross-correlation is found to be the optimum measure. However, the success of the employed cost functions and optimization algorithms has been reported by the authors to be highly depended on the breathing motions artifacts. In

[1] also called X-ray fluoroscopy image

[5], the authors introduce a novel similarity measure, stochastic rank correlation, to overcome the assumption that there is a linear relationship between the intensities of the images to be registered.

2.1.2. Intensity-based non-rigid Slice-to-Volume registration

For a similar application to ours, namely the CT-fluoro guided lung ablation, a non-rigid intensity based slice-to-volume registration algorithm is employed by Yaniv et al. [133]. In particular, Thirion's DEMONS [115] algorithm is evaluated on a synthetic dataset and is found to be unsuitable for recovering even very small deformations (less than $4mm$).

2.1.3. Feature-based rigid Slice-to-Volume Registration

Augmented reality guided radio frequency ablation is proposed in [77]. Based on radio-opaque fiducials, an extended 3D/2D criterion, incorporating error prediction, is used to register a 3D patient model including skin, liver, and tumor(s) generated from pre-operative CT data to the patient. Evaluations of this system on real patients is presented in [80].

During interventions under CT/CT-fluoro guidance, the radiologists are also exposed to radiation by the system itself and scattered radiation from the patient. Therefore, robotic systems are proposed for overcoming this problem. Robotic assisted spine and kidney interventions are reported in [85]. The same robotic system has also been used in a randomized patient study for liver biopsies [84]. The final insertion has been done by an interventionalist based on the system calculations with the outcome of a shorter time, better accuracy, and less irradiation of physician and patient.

2.1.4. Combined Methods for non-rigid Slice-to-Volume Registration

Integration of vessel feature in intensity based methods for registering US slices to preoperative MR volumes also for RF liver ablation is reported in [87]. Their work is extended by Blackall et al. [8] to a patient specific breathing model incorporating deformations. By using the motion models, the authors drastically reduce the degrees of freedom (DOF) of a non-rigid registration. However, the model does not take into account the deformation induced by the needle pressure and relies on previously acquired MR volumes in different breathing stages. A review of active models for image guided interventions can be found in [43]. Some authors propose an insertion of fiducial markers into the liver for updating and estimating its deformation in real-time during the intervention. Also, technical guidance like electro-magnetic [120] or optical tracking [71, 70] is employed for updating a deformable model of the liver. These systems have been evaluated during CT-guided in-vitro studies of a liver phantom and in-vivo animal studies.

2.2. Uncertainty Visualization

Uncertainty visualization is a wide area and topic of many research activities in the field of visualization. Different approaches have been developed and proposed depending on the application and the data types. For one dimensional data, error bars are common, whereas for two dimensional data glyphs like arrows, balls, cones, ellipses, boxes, and lines. Also different forms of surfaces (fuzzy, blurred, transparent, colors, overlays) and animations belong to the arsenal of uncertainty visualization. The last two approaches are also used for three dimensional data. An overview of uncertainty visualization can be found in [83, 53]. In the context of medical uncertainty visualization, the work of Simpson et al. [110] visualizes the registration uncertainty on a linear path for a surgical task. The method consists of rendering a path distribution volume to aid the instrument placing. Recent work of Lundstrom et al. [66] proposes a probabilistic animation to visualize the uncertainty in medical volume rendering for tissue classification. There, the authors offer different animation modes with user interaction in order to help the diagnostic decision support which is routinely very tedious task, since the radiologists manually explore adjustments of the transfer functions provided for the tissue classification.

Part II.

Visualization Modes for CT-Fluoro guided RF Liver Ablation

CHAPTER

THREE

SUBVOLUME VISUALIZATION BASED ON PIECEWISE SLICE-TO-VOLUME REGISTRATION

3.1. Introduction

THIS chapter presents a visualization which is based on piecewise rigid/affine registration of the CT-fluoro slice to the CT-volume. Rigid/affine models do not capture the deformation [21]. However, by dividing the liver into different parts and searching for each part in the whole CT-volume separately, we expect to estimate the deformation volume. With an adequate visualization of the volume of interest, the interventional radiologist can orientate further without interrupting his work. This will also reduce the number of interventionally acquired slices resulting in less radiation for patient and physician. The visualization is a side-by-side 2D display as in figure 3.14 and additional 3D displays with 3D coronal and sagittal views of the registration results and segmented liver as shown in figure 3.16. The 3D visualization provides information on how the oblique views are located in the liver.

The derivation of clinical ground truth (GT) data by incorporating by incorporating fiducial markers as proposed in [103] is due to the minimal-invasive nature of this procedure very difficult.

We therefore generate a synthetic data set allowing precise analysis and testing of the registration solutions. For this purpose, approximated fluoro slice simulations are obtained from the pre-interventional CT-volume to evaluate registration algorithms. The creation of this synthetic data is described in section 3.5.1.

We have also have asked two experienced interventional radiologists to independently define planes in the pre-interventional CT-volume that they consider to be the best approximation to the corresponding fluoro slices. An inter-observer variation in the definition of corresponding slices has been clearly observed (see table 3.1). Partner physicians believe that also intra-observer variation is highly possible, in case one interventionalist is asked to redefine the slices at a later time. We are using the manually selected slices to quantitatively and qualitatively evaluate the registration results on real CT-fluoro data.

3.2. Methods

3.2.1. Registration Details

The registration is purely intensity based. Vessel features are not visible in CT-fluoro slices in order to be used for the registration. We employ a robust similarity measure f as described in [126, p.14]. This choice is justified by the low signal-to-noise ratio of the CT-fluoro slices, the intensity differences between contrasted volume and not contrasted CT-fluoro slice, and presence of needle in the 2D CT-fluoro slices. Let a pixel in the 2D CT-fluoro slice (fixed image) be $\mathcal{X}$. Its intensity in this image is $\mathcal{I}^*(\mathcal{X})$. Further, let $\mathbf{T}$ be the transformation matrix defining a certain pose estimate $\mathbf{x}$ of the 3D CT-volume. When projected at this pose, the volume results in an image $\mathcal{I}\left(\mathbf{T}(\mathbf{x})\mathcal{X}\right)$.

$$f(\mathbf{x}) = \sum_{\mathcal{X}_i} \frac{1}{1 + \frac{\mathcal{I}^*(\mathcal{X}_i) - \mathcal{I}(\mathbf{T}(\mathbf{x})\mathcal{X}_i)}{\alpha^2}} \tag{3.1}$$

Here, α defines the sensitivity to outliers of the bell shaped function f. If it is chosen small, it results in a high rejection rate. Additionally, we constrain the rotation parameters $[b_l, b_u]$ that we deduced empirically by letting experienced interventional radiologists define slices in the pre-interventional volume being closest to the corresponding CT-fluoro slice. Also, the translation along the z-axis is constrained within the volume bounds. The barrier function, penalizing the involved parameters when approaching the limits, is thus the following:

$$b(\mathbf{x}) = \sum_{i=3}^{6} \exp(-\beta(x_i - b_l)(b_u - x_i)) \tag{3.2}$$

where β is a scaling factor controlling the U-shape of the exponential. It is chosen such that the barrier function is near zero inside the interval $[b_l, b_u]$ and very high when approaching the limits. The function to minimize becomes now:

$$f_{total}(\mathbf{x}) = f(\mathbf{x}) + \lambda b(\mathbf{x})) \tag{3.3}$$

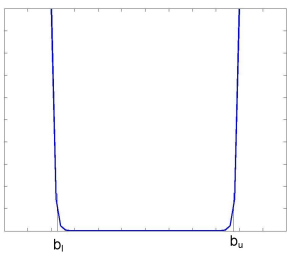

Figure 3.1.: Barrier function. Between the interval $[b_l, b_u]$ the barrier function is almost zero whereas outside it has a very high value.

For optimization, we use the Best Neighbor[1] optimizer in a multiresolution approach to avoid the local minima.

3.3. Subvolume Visualization based on piecewise rigid Registration

3.3.1. Two-Planes Visualization

The most simple approach to piecewise registration divides the liver into two parts, an upper part containing the ventral side of the liver and a lower containing the dorsal side of the liver. That way, rigid registration is expected to provide better results, since both parts undergo different level of movement and deformation. During expiration the rib cage volume decreases and, thus, increased pressure is applied to the ventral aspect of the liver. Each part is independently rigidly registered with the whole 3D CT-volume. The resulting two planes define a subvolume which can be smoothly displayed by interpolation. One possible way is to interpolate the rotations separately via SLERP [109] while the translation is recovered linearly. Another way to interpolate between the planes is the use of dual quaternions [26, 56, 123] which incorporate rotation and translation. Figure 3.2 (a) shows the two part division.

3.3.2. Four-, Six-Planes Visualization

In order to better estimate the deformation, it is necessary to increase the pieces to be registered from two to four and six. This improves the estimation of the minimum volume of deformation, but, at the same time creates new and challenging problems in term of visualization. Instead of a simple sweep in-between the two planes, we need to visualize a more complex volume in such a way that is perceptually acceptable for the interventional radiologists. The pieces should be big enough to contain liver borders, also spleen border, and kidney, if they are present in the image, so that the registration process will have enough information to converge. See figure 3.2 for a scheme and figure 3.4 for a real example. Each part is rigidly registered independently with the whole 3D CT-volume. The registration details are provided in section 3.2.1. The planes 3.14, 3.15 which result from optimal transformation matrices of the registrations define a volume. A minimal path that optimally connects between these planes is searched to display the volume in-between. This problem can be modeled as an undirected weighted complete graph, the planes as the graph nodes and the distances between barycenters as the weights of the graph edges. Dijkstra's algorithm [28] is used to sort the graph. We are calculating the barycenters of each plane and sort the graph according to the Euclidean distances between them. Due to the symmetries we have $(n^2 - n)/2$ distances to calculate. A graph example with six planes is shown in Figure 3.3. Planes with highest distance represent the bounds, so we have $(n^2 - n)/2 - 2$ planes to sort. Once the planes are

[1] Also known as Hill Climbing

sorted, we are visualizing the volume in an animation sequence. In [109, 25], the authors show why it is very useful to represent rotations with quaternions and use quaternion interpolation to interpolate rotations. Our approach is based on 'Spherical Cubic Interpolation' (SQUAD). It is analogous to Bézier curve but involves 'Spherical Linear Interpolation' (SLERP) which performs a great arc interpolation of the four dimensional quaternion sphere resulting in a rotation with constant angular velocity. Once the rotation is estimated the translation is recovered linearly.

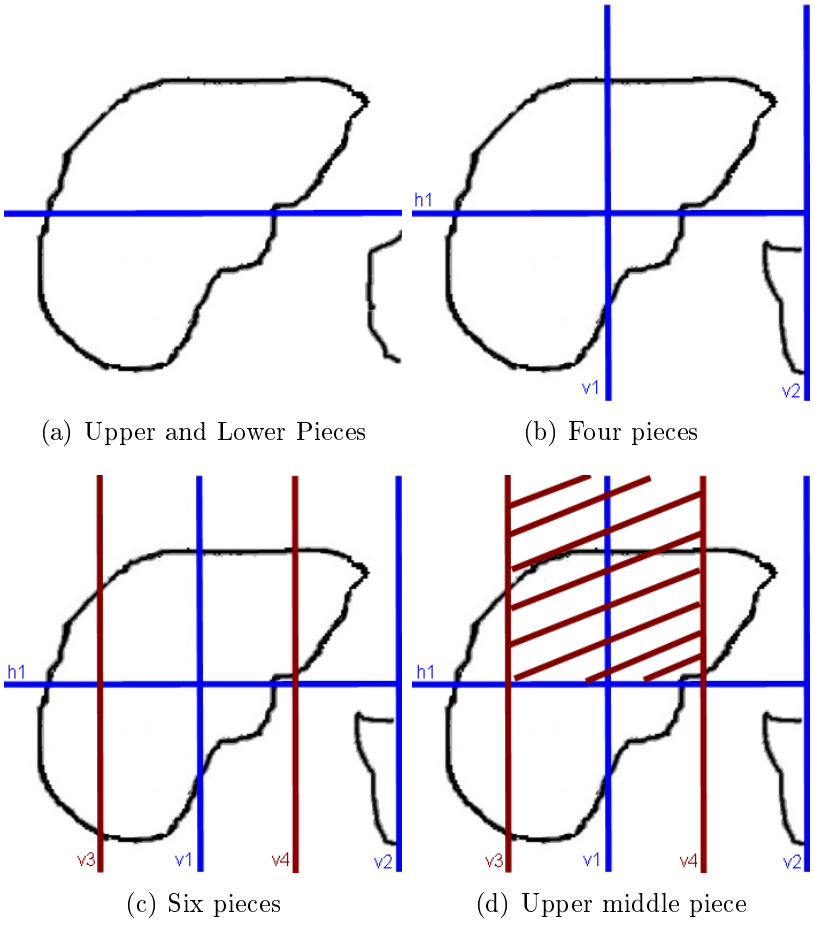

(a) Upper and Lower Pieces (b) Four pieces

(c) Six pieces (d) Upper middle piece

Figure 3.2.: Schematic piecewise division. (a) and (b) show the CT-fluoro slice on the left and the initial pose position inside the volume on the right, respectively. The blue horizontal and vertical lines divide the liver into four non-overlapping pieces. (c) shows the division of the liver into six pieces, four from (b) plus two overlapping pieces. The red lines include the two overlapping parts. (d) shows the upper middle piece of the six pieces division.

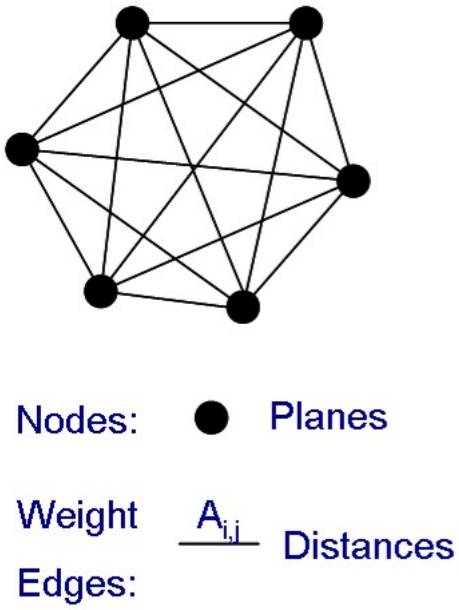

Figure 3.3.: Example of a graph represented by 6 planes. The nodes of the graph represent the planes and the edge weights represent the distances between the barycenters of the planes.

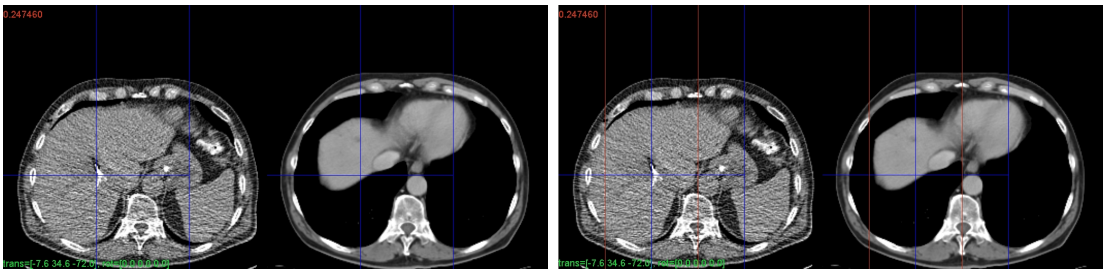

(a) Division into four pieces. (b) Division into six pieces

Figure 3.4.: Piecewise division on clinical images. (a) and (b) show each time on the left the CT-fluoro slice and on the right the initial pose position in the volume. The blue lines divide the liver into four not-overlapping pieces, while the red lines include two overlapping parts. The lines which are drawn in the CT-volume slice are only just for orientation, the registration process searches all the volume.

3.4. Simpler Visualization Modes

3.4.1. Axial-Planes Visualization

The first alternative approach is to visualize the axial slices around the globally registered plane. The motivation for this approach is that the interventional radiologists are used to axial slice representation. The globally registered plane is supposed to be in the area of interest. Axial slices going through two most outside corner points of the global registered plane represent the bounds of the new volume. This volume is interpolated along the z-axis. Figure 3.5 shows the configuration.

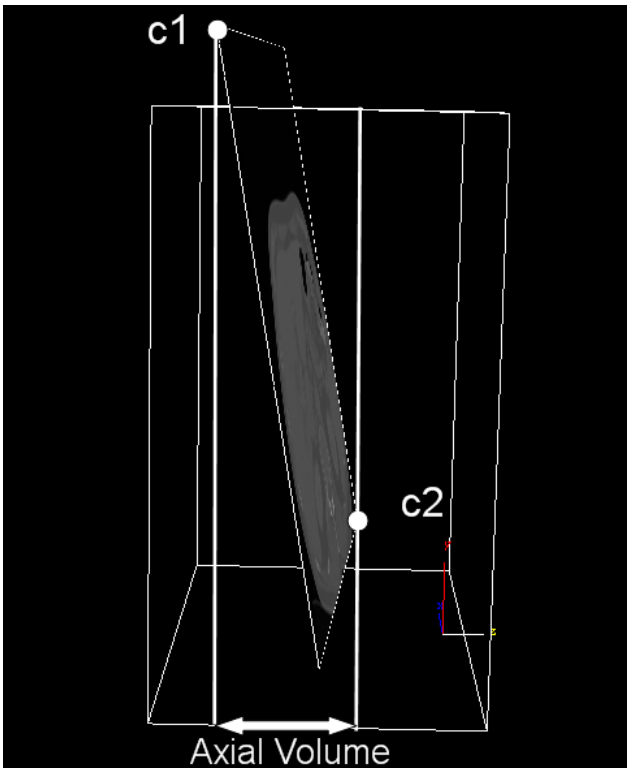

Figure 3.5.: The Axial Volume is defined by the axial slices going through the most outside corner points of the global registered slice.

3.4.2. Envelope-Planes Visualization

Another alternative approach for visualization is to define two envelope planes around the registered planes and display the volume in between these two planes in an animation sequence. The motivation for this approach is to provide an easier visualization since a simple sweep between two planes can be performed. Note that this volume will incorporate more information than needed by its definition. Each of these envelope planes is defined by the three most outside corner points of the registered planes in the z direction. These three points define the normal on the envelope plane, $\mathbf{z}_{envelope\ plane}$. In order to visualize the data properly, we need to define the new $\mathbf{x}_{new}$ axis as the most parallel to our Cartesian $\mathbf{x}$ axis. The new axis is given by

$$\mathbf{x}_{new} = \mathbf{x} - \operatorname{sgn}\left(\mathbf{x} \cdot \mathbf{z}_{envelope\ plane}\right) \mathbf{z}_{envelope\ plane} \tag{3.4}$$

Figure 3.6 shows the case where the angle between the x axis and the $\mathbf{z}_{envelope\ plane}$ is less than 90°. The derivation is done as following. Setting $\mathbf{z}_{envelope\ plane} = \mathbf{z}_{new}$ and considering first the case shown in Figure 3.6, we have

$$\mathbf{x} = \mathbf{x}_{new} + \mathbf{x}_{\|} \tag{3.5}$$

$$\begin{aligned} \mathbf{x}_{new} &= \mathbf{x} - \mathbf{x}_{\|} \\ &= \mathbf{x} - proj_{\mathbf{z}_{new}}\mathbf{x} \\ &= \mathbf{x} - d\mathbf{z}_{new} \end{aligned} \tag{3.6}$$

where

$$d = |\mathbf{x}| \cos\left(\theta\right) = |\mathbf{x}| \frac{\mathbf{x} \cdot \mathbf{z}_{new}}{|\mathbf{x}|\,|\mathbf{z}_{new}|} = \mathbf{x} \cdot \mathbf{z}_{new} \tag{3.7}$$

Thus, the new orientation of the envelope plane is given by the vector $\left(\mathbf{x}_{new}, \mathbf{y}_{new}, \mathbf{z}_{new}\right)^T$ with

$$\begin{aligned} \mathbf{x}_{new} &= \mathbf{x} - \left(\mathbf{x} \cdot \mathbf{z}_{new}\right) \mathbf{z}_{new} \\ \mathbf{y}_{new} &= \mathbf{z}_{new} \times \mathbf{x}_{new} \end{aligned} \tag{3.8}$$

If the angle between the x axis and the $\mathbf{z}_{envelope\ plane}$ axis is more than 90°, the vector $\mathbf{z}_{envelope\ plane}$ is flipped. $\mathbf{x}_{new}$ sums up the two components in equation 3.5. The translation is recovered by the intersection point of the z-axis and the plane.

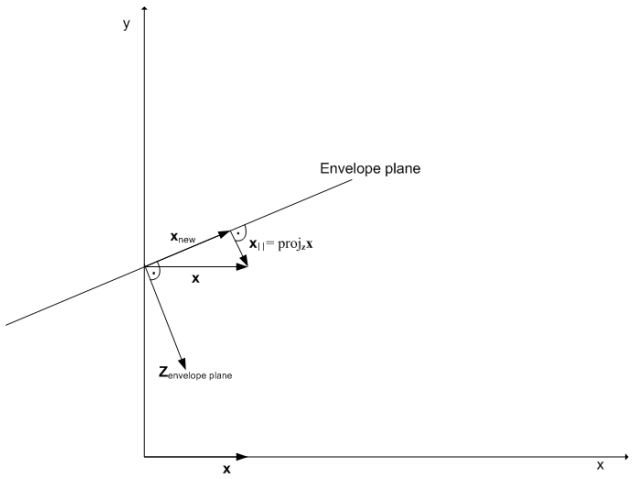

Figure 3.6.: Coordinate system definition of the envelope plane. $(\mathbf{x}, \mathbf{y}, \mathbf{z})$ represent the original coordinate system of the CT-volume. $(\mathbf{x}_{new}, \mathbf{z}_{envelope\ plane} \times \mathbf{x}_{new}, \mathbf{z}_{envelope\ plane})$ defines the new coordinate system for visualization.

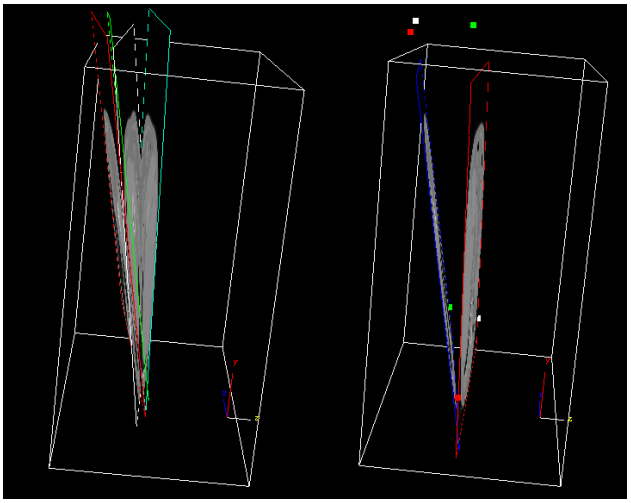

Figure 3.7.: Envelope Planes in 3D. The left image shows the four-planes and the right image is showing the envelope planes defined by the most outside points of the planes along the z direction.

3.5. Experiments and Results of Two-Planes Registration

3.5.1. Simulation Strategy

For the simulations, we take two routinely contrast-enhanced datasets acquired on a 4 detector-row CT (Siemens Somatom Sensation4) in deep inspiration breath-hold which have been acquired just prior to the interventional procedure. For one dataset (dataset1) raw data is provided. This raw data is twice reconstructed with Siemens Syngo IR Taskcard [116, 51]. The first time, the reconstruction is performed with the same DICOM header parameters as for the CT workstation in the hospital. The second time, the reconstruction uses the same parameters as previously, except for the current dose parameter which is decreased to generate a noisy volume. Thus both volumes have the same field of view. For the second dataset (dataset2) raw data is not available. Therefore, a software [129] is used to re-calculate the projections (raw data) of CT-data and to generate two CT volumes, one with noise and the other one without. Both datasets are downsampled in x, y from 512×512 to 256×256 to fit the fluoro slices, which have an image size of 256×256. For dataset1, the resulting volume size is: $256 \times 256 \times 208$ voxels with a voxel size of $1.32 \times 1.32 \times 1.00mm$, and for dataset2: $256 \times 256 \times 69$ with voxel size of $1.45 \times 1.45 \times 3.00mm$. Both volumes have a CT slice thickness of $3mm$.

The applied deformation is a simulated breathing deformation as proposed in [117]. A nonlinear transformation $T : \{B(x, y, z) = T(A(x, y, z))\}$ simulates the diaphragm and rib cage movement. Diaphragm movement is modeled as a translational force in the data sets' negative z direction. Nonlinearity is introduced by weighting the constant vertical translation t_v with a 2D Gaussian distribution that depends on the x, y coordinates of the data set, i.e. the further away from the center of the diaphragm surface a point is, the smaller the negative z translation. Mathematically, a displacement vector $\vec{d_1} = (0, 0, z')$ is applied to each point $(x, y, z)^T$ that maps it to $(x, y, z')^T$ with

$$z' = z - t_{vertical} e^{-\frac{(x-\mu_x)^2+(y-\mu_y)^2}{2\sigma^2}}$$

where (μ_x, μ_y) corresponds to the x, y coordinates of the center of gravity of the diaphragm points. σ is chosen such that points lying at the exterior of it nearly remain fixed. To simulate rib cage behavior during breathing, a radial, center-directed translation t_c is used to form a second displacement $\vec{d_2} = (x', y', 0)$ that maps points $(x, y, z)^T$ to $(x', y', z)^T$ with

$$\begin{pmatrix} x' \\ y' \end{pmatrix} = \begin{pmatrix} \mu_x \\ \mu_y \end{pmatrix} + t' * \frac{\vec{c}}{|\vec{c}|} \qquad where$$

$$\vec{c} = \begin{pmatrix} x - \mu_x \\ y - \mu_y \end{pmatrix} \qquad and \qquad t' = |\vec{c}| - t_{inplane} * (1 - e^{-\frac{(x-\mu_x)^2+(y-\mu_y)^2}{2\sigma^2}})$$

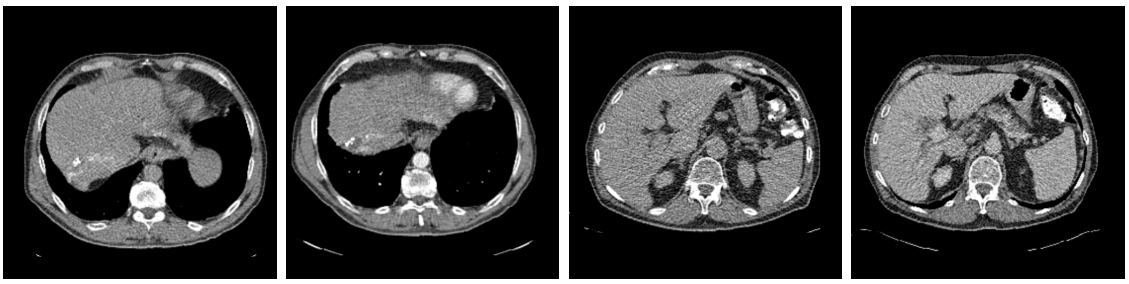

(a) real (b) sim. (c) real (d) sim.

Figure 3.8.: 2D CT-fluoro slices and simulations using a simple breathing model. (a) and (b) - dataset1, (c) and (d) - dataset2

Combination of $\vec{d_1}$ and $\vec{d_2}$ gives a total displacement $\vec{d}$ that is equivalent to the non-linear transformation $T : \{B(x, y, z) = A(x, y, z) + d(x, y, z)\}$. The two datasets were deformed with $t_v = 30mm$ and $t_c = 5mm$.

Thus, we simulate another volume in expiration stage, the rib cage is contracting, while the liver moves toward the heart.

Six axial slices are extracted from each noisy deformed volume, from all parts of the liver with $1cm$ spacing between. Figure 3.8 shows one example from each dataset of real and simulated fluoro slices.

3.5.2. Experiments on synthetic CT-fluoro Slices

The registration starts at an initial resolution of $64 \times 64 \times 52$, increases to $128 \times 128 \times 104$ and finishes at $256 \times 256 \times 104$. Dataset2 is downsampled only in x and y direction due to the lower resolution along z. Registration is performed first using all voxels of the 2D image. RMS error is calculated between all voxels in the CT-fluoro slice mapped back via the known displacement field in the original volume and the corresponding voxels mapped by the estimated parameters of the rigid and affine registration. Then, each slice is divided into lower and upper part. Tables 3.2, 3.3, 3.4 and 3.5 show the results of one plane versus the results of upper and lower plane. The RMS error between the CT-fluoro surface and the registered planes decreases by almost half except for Powell-Brent affine registration.

Figure 3.9 shows the rigid registration result planes of slice 2/dataset1 and 5/dataset1 with Best-Neighbor optimization. The resulting planes of the registration are intersecting the retrieved CT-fluoro surface. The upper and lower surface are better approximated by the 2 planes rather than by the one plane.

3.5.3. Experiments on clinical Data

Five CT-fluoro slices are selected from dataset2. They contain needle, the tumor and different parts of the liver which are often imaged during the intervention. For the five CT-fluoro slices (256×256, $1.48 \times 1.48mm$, slice thickness $4mm$), two

inverventional radiologists have defined the slices that they consider the closest to the respective CT-fluoro slices. The manual navigation has included 6 DOF, 3 for translation and 3 for rotation. This dataset has a significant liver motion and deformation, and it has posed difficulties even for experienced radiologists during manual registration. The other dataset which is used here, dataset3 ($256 \times 256 \times 158$, $1.29 \times 1.29 \times 1.5mm$), has been acquired in shallow breathing. The liver motion is not as significant as in dataset2. Three CT-fluoro slices are selected (256×256, $1.29 \times 1.29mm$, slice thickness $4mm$): one with needle and tumor, one with tumor, one with the liver next to the heart.

The variation between the slices defined by the interventional radiologists is shown below. Only liver voxels contribute to the RMS calculation. The cut dividing the liver into upper and lower part is set where the ligamentum falciforme is seen in the slice and is kept constant for all slices of one dataset, unless the intervention table has been moved down so that the physician has more space for needle insertion. The amount of voxels at each position $\mathbf{p}$ included in the volume of interest V defined by the upper plane: $\mathbf{n_u}, d_u$ and lower plane: $\mathbf{n_l}, d_l$, satisfy following inequality:

$$\left(\mathbf{p}\mathbf{n_l}^T - d_l\right)\left(\mathbf{p}\mathbf{n_u}^T - d_u\right) < 0$$

Tables 3.6, 3.7 and 3.8 show the percentage of the liver voxels included in the volume for the slices Def1, Def2 which are defined by the two radiologists. For real data, the rigid model with Powell-Brent optimization works best. In particular, slice 3 of dataset2 (ds2) poses difficulties for automatic registration due to a big rotation($\approx 12°$) about the x-axis compared to the initial pose. But visual inspection of the resulting registration and angle calculations of both defined slices to the next registered plane for this case (Def2: 0.77° and Def1: 1.96°) show that they lie very close to the volume. Figure 3.10 (a) shows this configuration and 3.10(b) shows an ideal configuration for slice 1. For slice 2 of dataset3 (ds3), we have also calculated the angles of the defined slices to the registered next plane. Additionally, the RMS error between liver voxels that are not included in the volume and the next registered plane has been calculated (Def1: 1.38°, RMS $1.92mm$, Def2: 2.52°, RMS $5.65mm$). Both RMS errors lie under RMS variation of Def1 and Def2 for this slice. This configuration is shown in figure 3.10 (d).

	Dataset2					Dataset3		
Slice	1	2	3	4	5	1	2	3
RMS[mm]	17.16	10.25	5.79	16.50	19.68	4.12	7.05	9.08

Table 3.1.: RMS[mm] for inter-observer variation.

	Best-Neighbor					
	Rigid			Affine		
Slice	one	lower	upper	one	lower	upper
1	12.98	5.90	4.35	8.27	5.59	4.95
2	11.08	5.77	4.61	9.86	5.83	4.95
3	9.61	5.84	4.76	10.52	5.84	5.02
4	9.69	5.95	4.90	9.72	6.17	4.89
5	9.59	6.19	10.59	9.60	6.22	5.10
6	8.20	6.53	4.73	9.51	6.43	4.85
Mean	10.19	5.84		9.58	5.49	

Table 3.2.: RMS[mm] for Best-Neighbor optimization. Dataset1 - $256 \times 256 \times 208$

	Powell-Brent					
	Rigid			Affine		
Slice	one	lower	upper	one	lower	upper
1	10.51	7.68	5.90	6.75	9.17	5.42
2	10.36	6.96	6.43	6.95	6.24	7.39
3	12.56	6.72	4.46	6.86	5.81	5.09
4	9.19	7.21	8.17	7.57	6.25	8.36
5	10.58	5.80	4.30	6.90	7.51	6.19
6	8.53	6.37	7.75	8.07	5.88	5.36
Mean	10.29	6.48		7.18	6.56	

Table 3.3.: RMS[mm] for Powell-Brent optimization. Dataset1 - $256 \times 256 \times 208$

	Best-Neighbor					
	Rigid			Affine		
Slice	one	lower	upper	one	lower	upper
1	10.66	6.78	8.69	11.19	6.70	5.46
2	15.97	12.89	12.23	16.64	7.46	7.52
3	15.04	7.90	9.32	15.68	6.94	9.04
4	10.25	6.594	4.87	13.51	6.57	5.66
5	11.55	8.50	6.86	18.48	8.35	5.84
6	10.20	7.72	5.59	10.08	7.59	6.53
Mean	12.28	8.15		14.26	7.00	

Table 3.4.: RMS[mm] for Best-Neigbor optimization. Dataset2 - $256 \times 256 \times 69$

	Powell-Brent					
	Rigid			Affine		
Slice	one	lower	upper	one	lower	upper
1	10.28	8.85	10.27	10.02	8.45	9.19
2	16.34	8.06	7.49	12.02	11.67	9.86
3	16.44	8.50	8.23	7.45	9.13	15.01
4	11.37	7.07	6.14	9.87	6.45	8.46
5	11.73	8.52	9.77	10.66	9.39	10.93
6	10.26	7.86	8.86	7.87	9.53	5.85
Mean	12.74	8.30		9.65	9.49	

Table 3.5.: RMS[mm] for Powell-Brent optimization. Dataset2 - $256 \times 256 \times 69$

	Percentage of voxels included in VOI					
	Rigid Powell-Brent					
Slice	1	2	3	4	5	Mean
%Def1	100	94.45	30.20	79.11	65.5	75.26
%Def2	100	96.09	0	74.52	11.81	60.01
	Rigid Best-Neighbor					
%Def1	72.55	73.57	44.00	71.00	78.81	68.95
%Def2	49.58	76.62	0	70.00	100	62.15

Table 3.6.: Dataset2 – percentage of included liver voxels for each defined slice in the subvolume

	Percentage of voxels included in VOI					
	Affine Powell-Brent					
Slice	1	2	3	4	5	Mean
%Def1	100	81.07	65.32	59.19	67.91	67.91
%Def2	96.12	87.87	2.82	61.17	14.13	55.73
	Affine Best-Neighbor					
%Def1	88.14	24.44	5.58	68.89	65.50	54.00
%Def2	72.69	27.75	7.77	70.14	19.91	41.21

Table 3.7.: Dataset2 – percentage of included liver voxels for each defined slice in the subvolume

	Percentage of voxels included in VOI							
	Rigid Powell-Brent				Affine Powell-Brent			
Slice	1	2	3	Mean	1	2	3	Mean
%Def1	99.60	78.93	100	91.37	98.88	100	45.63	79.96
%Def2	72.51	0	100	55.70	63.79	64.58	73.55	67.71
	Rigid Best-Neighbor				Affine Best-Neighbor			
%Def1	5.59	52.82	77.90	51.03	44.64	97.49	37.99	63.63
%Def2	69.45	0	83.16	48.66	69.3	6.22	53.09	39.77

Table 3.8.: Dataset3 – percentage of included liver voxels for each defined slice in the subvolume

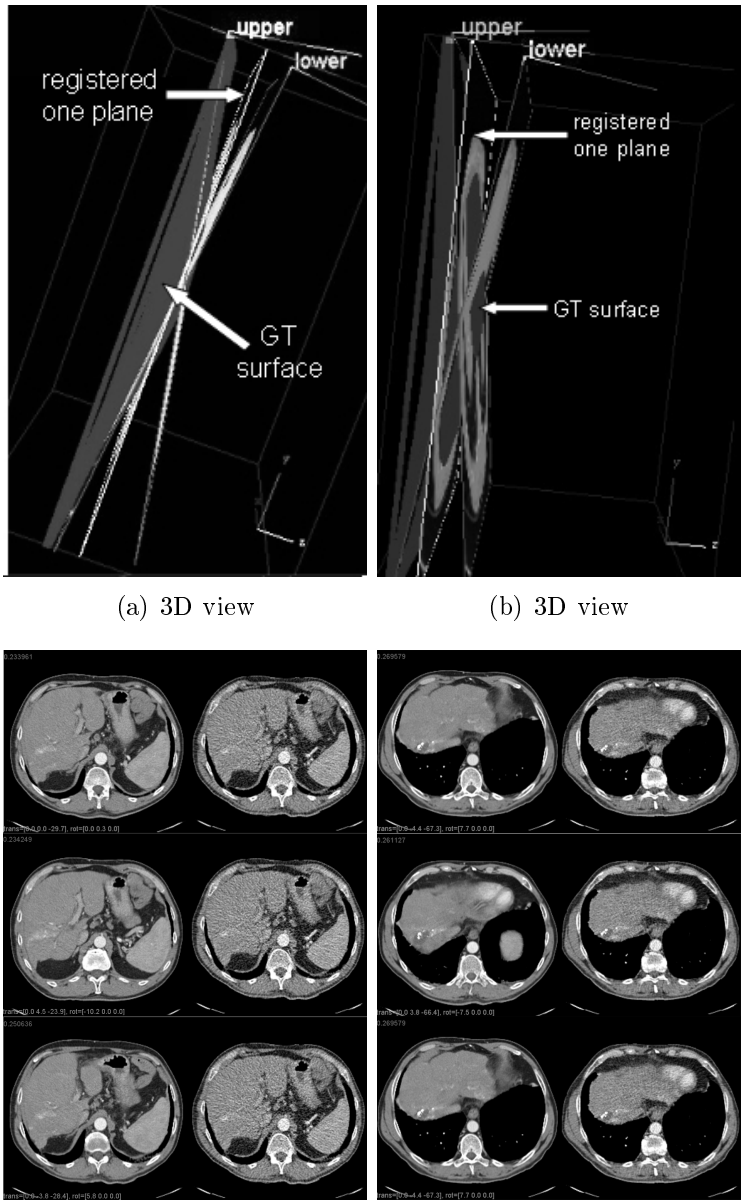

(a) 3D view (b) 3D view

(c) 2D views (d) 2D views

Figure 3.9.: Registration results for two-piece registration: 3D views showing the GT-surface and registered upper, lower and one plane. 2D views showing from top to bottom the registered one plane, upper and lower. (a) and (c) belong to dataset1, (b) and (d) belong to dataset2.

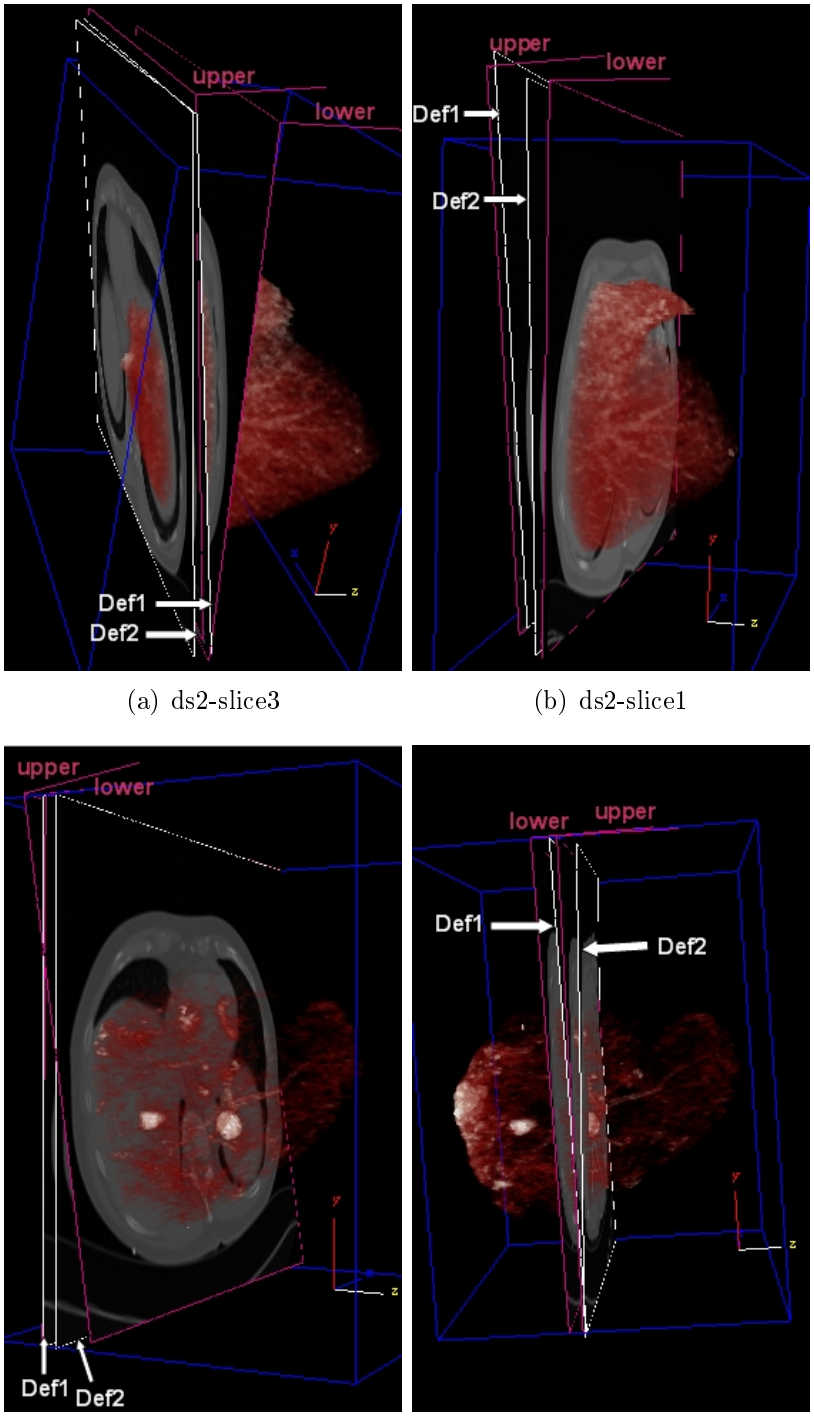

(a) ds2-slice3 (b) ds2-slice1

(c) ds3-slice1 (d) ds3-slice2

Figure 3.10.: Configurations of registered upper and lower plane, defined slices Def1, Def2 by the interventional radiologists and rendered liver surface for rigid registration with Powell-Brent optimization scheme. (a) Def1 30%, Def2 0% (b) Def1 100%, Def2 100% (c) Def1 100%, Def2 79% (d) Def1 79%, Def2 0%

3.6. Experiments and Results of Four-, Six-Planes Registration

3.6.1. Experiments on synthetic CT-fluoro Slices

In the previous section 3.5.1, we have derived synthetic slices according to a breathing model as described in [117]. There, we have shown that the division of the CT-fluoro slice into 2 pieces decreases the RMS error of the registration results by almost half. Here, for deriving synthetic 2D CT-fluoro slices that also include deformations, we take two CT-volumes of one patient, the pre- and the post-interventional datasets. The pre-interventional CT-volume (the template volume) is elastically [76, 136] registered to the post-interventional CT-volume (the reference volume). Since after the intervention, the patient is not able to achieve the full inspiration breath-hold as before the intervention, the registration of the pre-interventional to the post-interventional scan is mimicking a possible expiration movement. This post-interventional scan is not used for the next steps, only the deformed volume. The displacement field for the achieved deformation maps the voxels of the deformed volume into the pre-interventional scan. In this way, by extracting axial slices of this deformed volume, adding noise (cf. [129]), each of these slices represent hypothetical CT-fluoro slices. We choose the piecewise registration based on six pieces for precise evaluation since this has been the preferred mode for the interventional radiologists (see 3.7). Deformation models for two different patients are generated using, for each of them, the pre- and post-interventional volumes. Six axial slices are extracted from the deformed volume every $5mm$. Visual inspection for each slice has been carried out. The deformation surface is almost included into the subvolume (see figures 3.11(d), 3.11(e), 3.13(d), 3.13(e)). Only a maximum displacement of $3mm$ has been measured between the registered slices to the voxels of the deformation surface that are not included.

3.6.2. Experiments on clinical Data

For evaluation we use three routinely acquired datasets of three different patients. Two datasets are acquired with a 4 detector-row CT, Siemens Somatom Sensation4, one in deep inspiration breath-hold and the second in shallow breathing. The third one is acquired with a 16 detector-row CT, Siemens Somatom Sensation16. We select CT-fluoro slices being imaged routinely during the intervention. In total, eleven CT-fluoro slices are evaluated, five from one dataset, and three from the other datasets, respectively. Each slice is globally and piecewise (4- and 6-pieces) registered to the whole volume. The average time for the registration takes $27s$ on a notebook with 1.80GHz Intel Pentium processor and 1GB of memory. This time can be reduced to real time by parallelization of the piecewise registration on a more powerful machine. Figure 3.14 is showing the results of one real CT-fluoro slice.

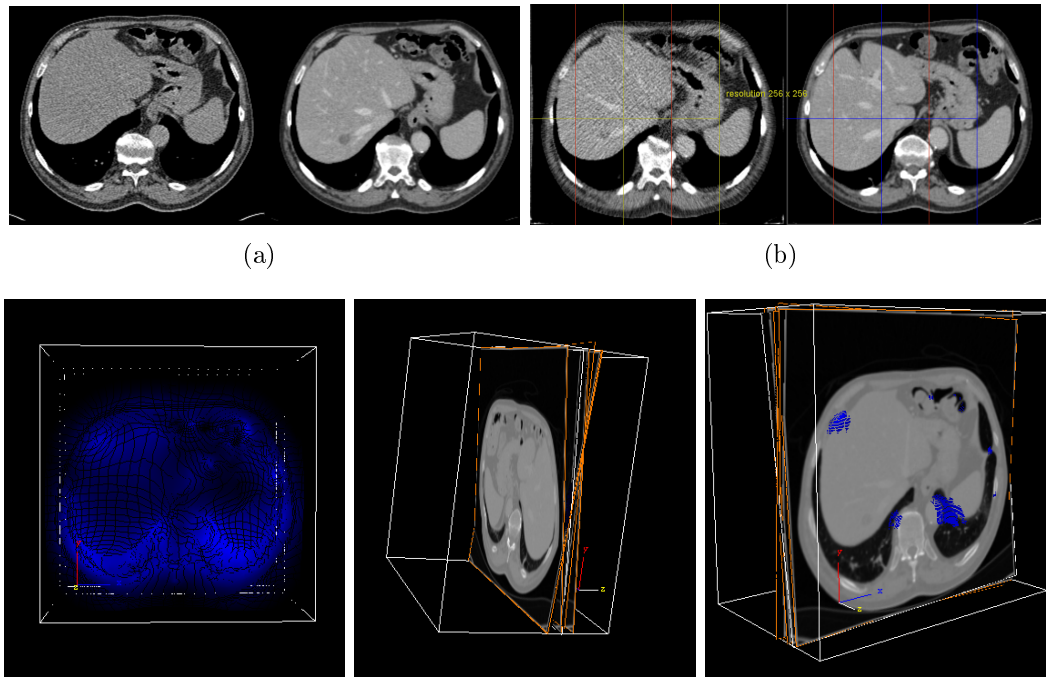

(a) (b)

(c) (d) (e)

Figure 3.11.: Simulations including deformations and noise. (a) is showing a real CT-fluoro and initial axial position in the pre-interventional volume. (b) is showing a synthetic simulated CT-fluoro slice on the left and initial axial position in the pre-interventional volume. The cranio-caudal depth is coded from dark to light. (d) and (e) are showing the 6 planes resulting from the piecewise registration from two perspectives. Most of the liver voxels are included in the volume. The liver voxels that are not included show a distance less than 3mm to the closest plane.

3.7. Evaluation

Two experienced interventional radiologists evaluated the visualizations modes. All visualization modes displayed the information contained in the CT-fluoro slice. The scale for the preference of visualization is qualitatively assessed:

- do not like it at all
- do not like it
- like it
- like it very much

To quantify the qualitative results, the preference has been translated to an integer scale from -2 up to 2 integer numbers. The diagram of the average of the grades

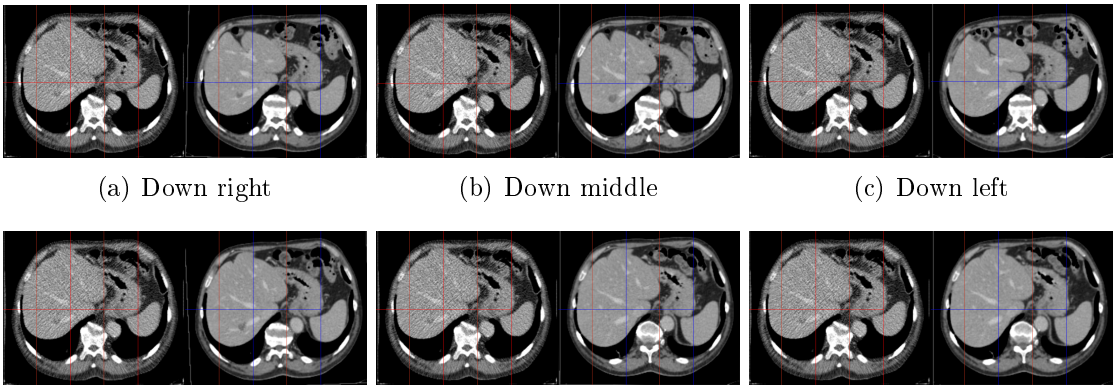

(a) Down right (b) Down middle (c) Down left

(d) Upper left (e) Upper middle (f) Upper right

Figure 3.12.: 2D views of six-pieces registration results for one synthetic slice. Right and left represent the right and left patient side.

for each mode is shown in figure 3.17. In the beginning of the evaluation of the visualization modes, the preference has been the axial volume. This is expected since the interventional radiologists are used to axial slices and other views need first some training to get used to it. After more evaluations, the preference turned toward the six-planes. The envelope-planes cover usually much more information than needed therefore it was also not preferable.

3.8. Discussion

In this chapter, we have proposed and evaluated the visualization of a minimum volume within the high resolution pre-interventional CT, by means of the registration of respectively, four and six sections of liver to the entire CT-volume. The liver is divided into multiple rectangular regions. We are opting for this choice because common anatomical divisions of the liver like the Couinaud [23] segments do not perform satisfactory for this slice-to-volume registration due to absence of enough information in some segments. In [130], the authors have chosen a circular shape for tracking the pulmonary texture since it better approximates the motion with respect to the surrounding area. For the liver application this is not the preferred choice. More importantly, it is to include organ borders since these are the main source of information due to the homogeneous tissue in the liver. The splitting is done automatically except of the width definition in the CT-fluoro slice. This can be done before the intervention starts and is kept constant for all time. More sections rather than six can be defined but results on the synthetic and clinical data showed that this number is enough for providing the required information.

In the experiments on synthetic CT-fluoro slices including deformation, we have observed that the deformation is included within the volume defined by the slices. For the qualitative assessment of the visualization, we have introduced alternative

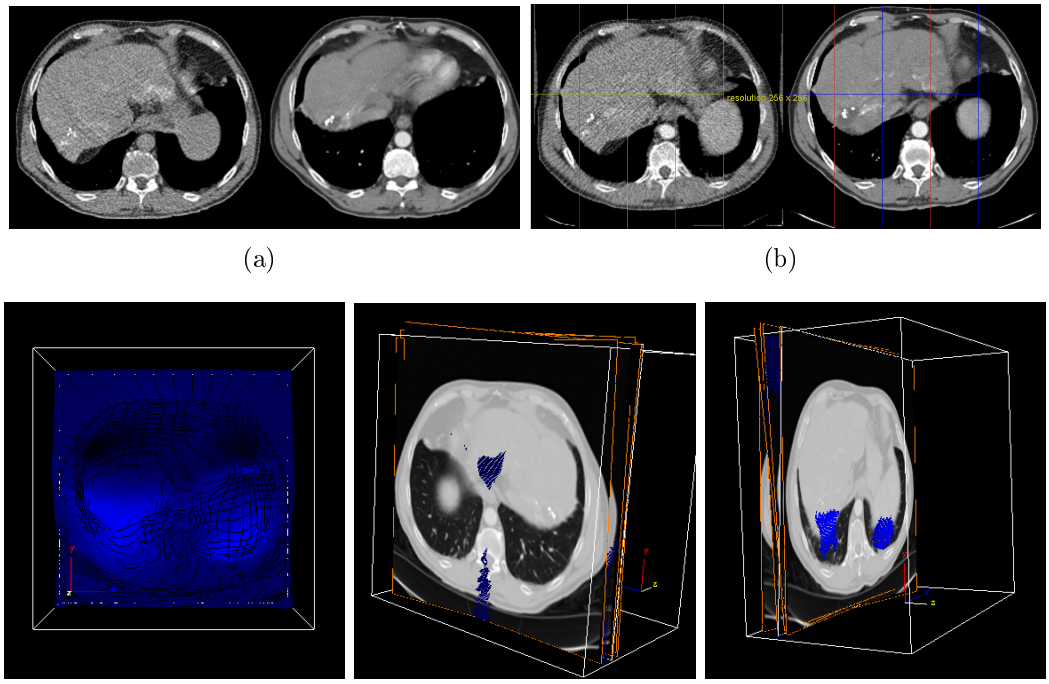

(a) (b)

(c) (d) (e)

Figure 3.13.: Clinical data next to simulations derived from the same patient including deformations and noise. (a) shows a real CT-fluoro and initial axial position in the pre-interventional volume. (b) shows a synthetic simulated CT-fluoro slice on the left and initial axial position in the pre-interventional volume. (c) is showing the deformation surface of the corresponding synthetic CT-fluoro slice. The cranio-caudal depth is coded from dark to light. (d) and (e) are showing the 6 planes resulting from the piecewise registration from two perspectives. Most of the liver voxels are included in the volume. The liver voxels that are not included show a distance less than 3mm to the closest plane.

modes. The first one is defined by the envelope planes of the minimum volume, while the second one is the volume defined by axial slices around the global registered slice. The evaluation of patient data by two interventional radiologists has shown a clear preference for the visualization of the minimum volume defined by the six-planes, followed by the four-planes, over the envelope planes, and the traditional axial planes. The interventional radiologists highly appreciated the possibility to assess the target lesion and its neighborhood in relation to the CT-fluoro image.

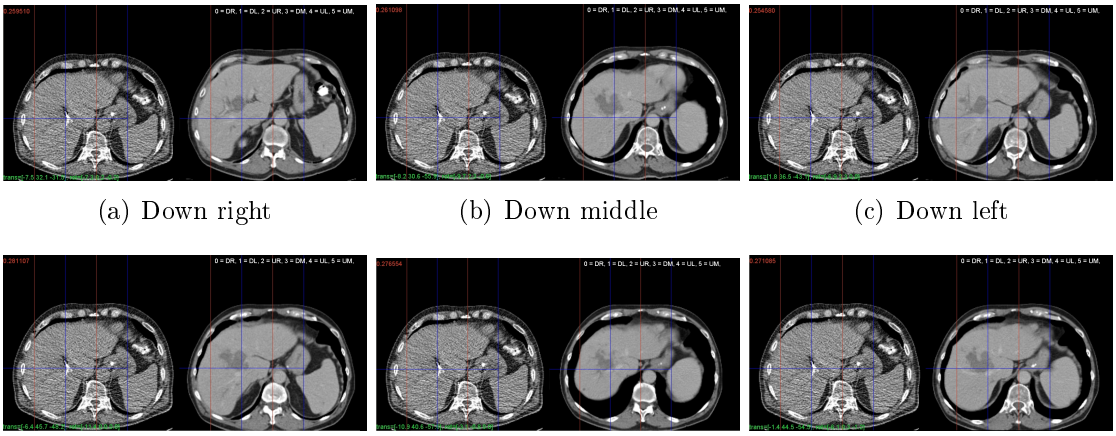

(a) Down right (b) Down middle (c) Down left

(d) Upper right (e) Upper middle (f) Upper left

Figure 3.14.: 2D views of six-pieces registration results on real CT-fluoro images. Right and left represent the right and left patient side. The registration results of the four-pieces registration are included into the six-pieces registration: (a), (c), (d), (f) represent the four-pieces registration results.

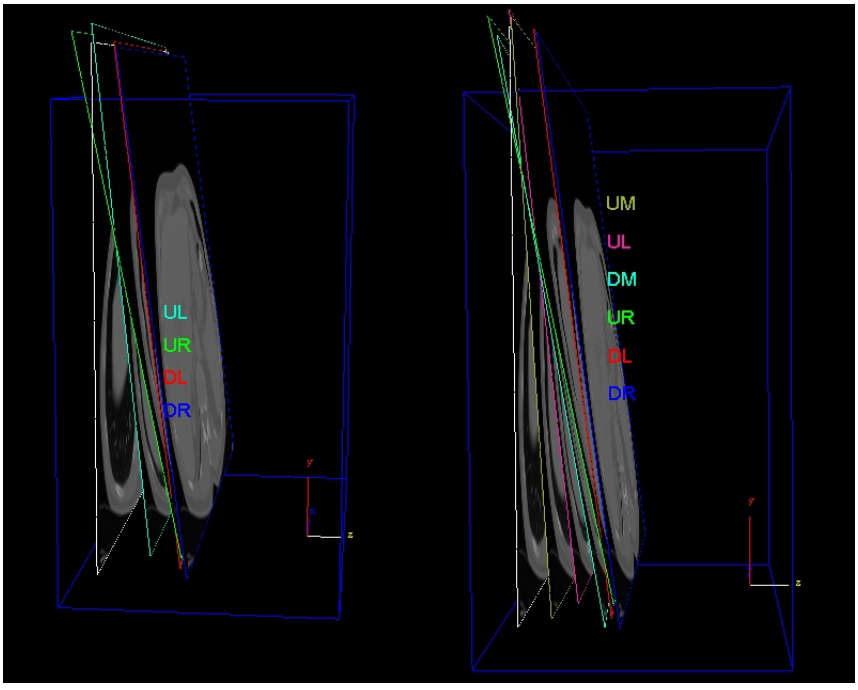

(a) Four and six planes

Figure 3.15.: 3D views of piecewise registration results. The initial pose position in the volume as axial slice is also shown (most left).

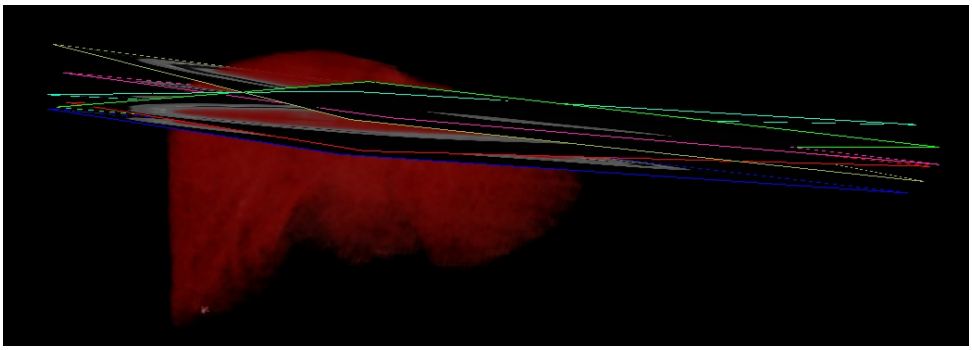

(a) 3D sagittal-coronal view

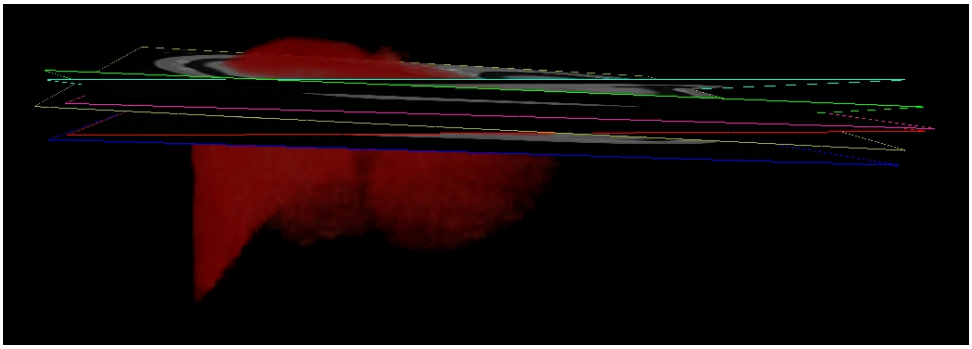

(b) 3D coronal view

Figure 3.16.: 3D sagittal-coronal and 3D coronal views. (a) is showing a sagittal-coronal view of the resulting planes and segmented liver. (b) shows a coronal view of the resulting planes and segmented liver.

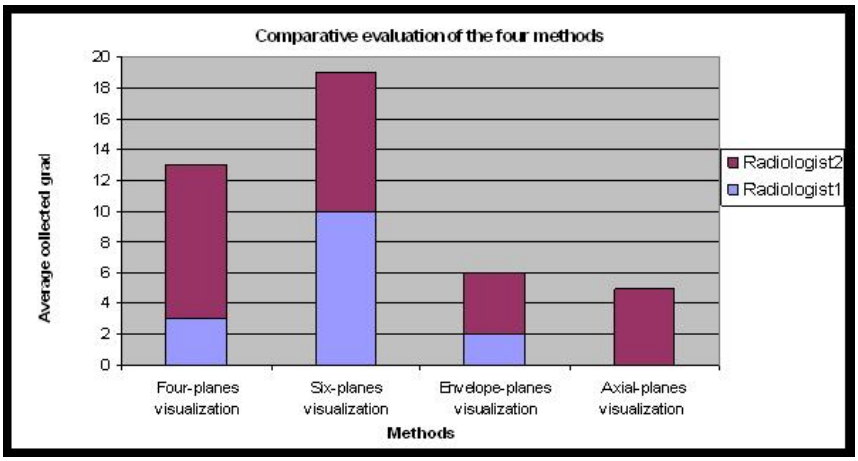

Figure 3.17.: Qualitative evaluation of the four different visualization modes.

CHAPTER

FOUR

ADAPTIVE VISUALIZATION BASED ON ISOSURFACES OF SLICE-TO-VOLUME SIMILARITY FUNCTION

4.1. Introduction

In contrast to the previous approach in chapter 3, this chapter presents a method which aims to first obtain a solution to the global registration and then visualize a specific volume that encompasses its neighborhood. Instead of targeting a unique solution for the registration process, we are proposing a set of solutions defined in the convergence basin of the registration result. In this neighborhood, we sample the isosurfaces of the employed cost function by using a line search strategy in order to retrieve the out-of-plane motion parameters. This is based on the assumption that the optimization path of the similarity measure during minimization encounters uncertainty along flat hypersurfaces.

In order to overcome the breathing motion artifacts, the noise, and also the needle artifacts in the CT-fluoro slice, we are employing slice-to-volume rigid robust least-squares minimization. To this end, an Iteratively Reweighted Least-Squares (IRLS) technique is used. Equivalent approaches have been already employed for robust feature- based vascular image registration [113] and retinal mosaicking [15]. In [82], robust image intensity based registration is used for mono- and multimodal image registration. Another class of estimators, called annealing M-estimators, have been introduced in [64, 65, 63]. These estimators are robust to outliers and adapt to discontinuities. They are used for estimating point locations corrupted by noise, respectively for estimating rotation angles from image sequences. In this chapter, we compare both types of estimators for our registration and visualization task.

Figure 4.1 gives an overview of the registration and visualization process of this chapter.

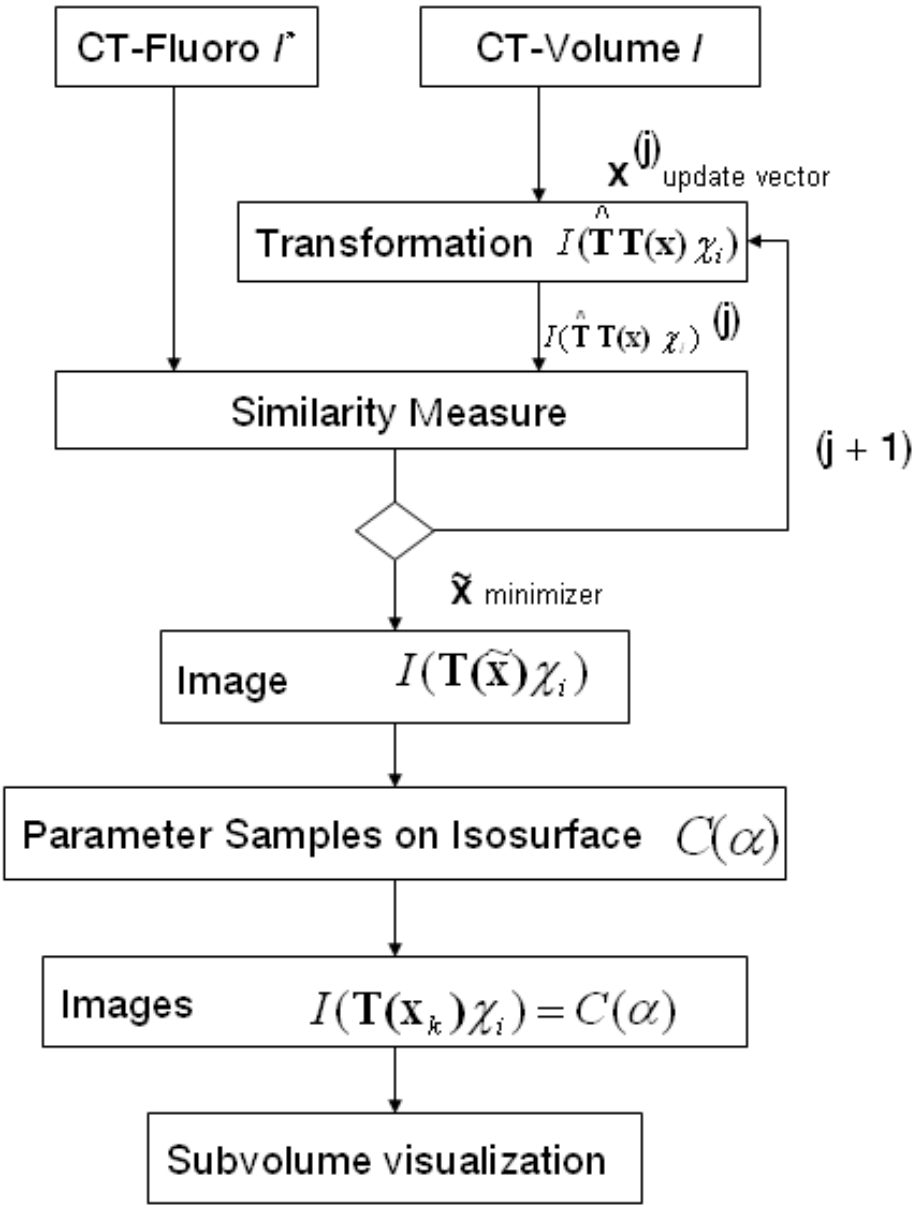

Figure 4.1.: Process of image registration and visualization.

4.2. Registration Details

4.2.1. Parameterization of the 3D Transformations

In order to register the 2D CT-fluoro slice with the 3D CT-volume, the latter should be projected onto a gray-scale image after having been subject to a 3D rigid transformation. Such transformation can be described by a (4×4) matrix $\mathbf{T}$ that belongs to the Special Euclidean group $\mathbb{SE}(3)$ having the following form

$$\mathbf{T} = \begin{bmatrix} \mathbf{R} & \mathbf{t} \\ \mathbf{0} & 1 \end{bmatrix}$$

where $\mathbf{R} \in \mathbb{SO}(3)$ is a 3D rotation matrix and $\mathbf{t} \in \mathbb{R}^3$ is the translation vector. Such matrix has 6 d.o.f and can be parameterized using the Lie-Algebra $\mathfrak{se}(3)$ that corresponds to the Lie group $\mathbb{SE}(3)$ through the exponential map. Let $\mathbf{A}_i$, with $i \in \{1, ..., 6\}$, be a basis of the Lie algebra $\mathfrak{se}(3)$. Any matrix $\mathbf{A} \in \mathfrak{se}(3)$ can be written as a linear combination of the matrices $\mathbf{A}_i$:

$$\mathbf{A}(\mathbf{x}) = \sum_{i=1}^{6} x_i \mathbf{A}_i$$

where $\mathbf{x} = [x_1, \ ..., \ x_6]^\top$ and x_i is the i-th element of the base field. Let the vectors $\mathbf{b}_x = [1, 0, 0]^\top$, $\mathbf{b}_y = [0, 1, 0]^\top$ and $\mathbf{b}_z = [0, 0, 1]^\top$ be the natural orthonormal basis of $\mathbb{R}^3$. Knowing that the dimension of the matrices $\mathbf{A}_i$ is (4×4), the generators for the translation are

$$\mathbf{A}_1 = \begin{bmatrix} \mathbf{0} & \mathbf{b}_x \\ \mathbf{0} & 0 \end{bmatrix}, \mathbf{A}_2 = \begin{bmatrix} \mathbf{0} & \mathbf{b}_y \\ \mathbf{0} & 0 \end{bmatrix}, \mathbf{A}_3 = \begin{bmatrix} \mathbf{0} & \mathbf{b}_z \\ \mathbf{0} & 0 \end{bmatrix}$$

and the generators for the rotation are

$$\mathbf{A}_4 = \begin{bmatrix} [\mathbf{b}_x]_\times & \mathbf{0} \\ \mathbf{0} & 0 \end{bmatrix}, \mathbf{A}_5 = \begin{bmatrix} [\mathbf{b}_y]_\times & \mathbf{0} \\ \mathbf{0} & 0 \end{bmatrix}, \mathbf{A}_6 = \begin{bmatrix} [\mathbf{b}_z]_\times & \mathbf{0} \\ \mathbf{0} & 0 \end{bmatrix}$$

where $[\mathbf{b}_i]_\times$ is the skew matrix associated to the vector $\mathbf{b}_i$. The exponential map links the Lie algebra to the Lie Group: $\exp : \mathfrak{se}(3) \rightarrow \mathbb{SE}(3)$. It exists an open cube v about $\mathbf{0}$ in $\mathfrak{se}(3)$ and an open neighborhood U of the identity matrix $\mathbf{I}$ in $\mathbb{SE}(3)$ such that $\exp : v \rightarrow U$ is smooth and one-to-one onto, with a smooth inverse.

Hence given a coefficient vector $\mathbf{x} = [x_1, x_2, ..., x_6]$, the corresponding transformation matrix $\mathbf{T}$ is obtained as

$$\mathbf{T}(\mathbf{x}) = \exp(\sum_{i=1}^{6} x_i \mathbf{A}_i) \tag{4.1}$$

See for example [135] for more details concerning this parameterization.

4.2.2. Iterative registration method

A pixel in the 2D CT-fluoro slice (fixed image) is the result of the projection of a voxel $\mathcal{X}$. Its intensity in this image is $\mathcal{I}^*(\mathcal{X})$. Further, let $\mathbf{T}$ be the transformation matrix defining a certain pose estimate of the 3D CT-Volume. When projected at this pose, the volume results in an image $\mathcal{I}(\mathbf{T}\mathcal{X})$. Ideally, registering the 2D CT-fluoro slice with the 3D CT-Volume consists in finding the transformation matrix $\overline{\mathbf{T}}$ such that:

$$\forall \mathcal{X}_i, \quad \mathcal{I}\left(\overline{\mathbf{T}}\mathcal{X}_i\right) = \mathcal{I}^*(\mathcal{X}_i) \tag{4.2}$$

Due to the high non-linearity of the problem, the registration problem is generally solved iteratively by estimating at each iteration an incremental pose update $\mathbf{T}(\mathbf{x})$ that should be composed with the current estimate $\widehat{\mathbf{T}}$ such that a cost function is minimized. The cost function is generally based on the sum-of-squared differences of pixel intensities (SSD). In practice, it does not give satisfactory results for the reasons that we already mentioned in the previous chapter: the severe and natural noise of CT-fluoro slices, due to the low dose applied; the high contrast difference between the pre-interventional volume and the interventional CT-fluoro slices; the presence of needle in the interventional CT-fluoro slices. That is the reason why we are using two robust methods. As a first method, we employ M-estimators as cost function in combination with an 'Iteratively Reweighted Least Squares' (IRLS) process. As a comparative method, we use the annealing M-estimator as cost function in combination with a graduated non-convexity optimization [64, 65] in order to compute the update parameters for the incremental pose $\mathbf{T}(\mathbf{x})$. In the following sections, we will describe the cost functions based on the M-estimator and annealing M-estimator.

4.2.3. M-estimator

The cost function considered for this purpose penalizes the largest residues:

$$f(\mathbf{x}) = \sum_{\mathcal{X}_i} \rho\Big[\mathcal{I}^*(\mathcal{X}_i) - \mathcal{I}\left(\widehat{\mathbf{T}}\mathbf{T}(\mathbf{x})\mathcal{X}_i\right)\Big] \tag{4.3}$$

where the function ρ is called the robust loss function. There exist many possibilities for the ρ function e.g. Huber, Cauchy or Beaton-Tukey functions [112]. Basically, they all play the same role: they permit to give different weights to the image differences by putting at a disadvantage the larger residues and at a favor smaller ones (in different manners depending on the function used). The minimization process consists in estimating the weights (that reflect the confidence of each intensity difference), evaluating the vector $\mathbf{x}$ by solving the weighted system, then, reiterate until convergence. With all minimization techniques based on a descent direction e.g. Gradient descent, Newton, Gauss-Newton or Levenberg-Marquardt [36] (see also Appendix A), this approach automatically rejects the outliers, the noise, the needle presence and the high contrast differences (that are not solved by the image normalization). Therefore, the registration does not suffer from spurious measurements

and the real global minimum can be better localized. As M-estimator, we choose the popular Beaton-Tukey biweight function, which is a strict outliers rejector since it descends very fast toward zero with increasing error differences:

$$\rho\left(d\right) = \begin{cases} \frac{a^2}{6}\left[1 - \left(1 - \left(\frac{d}{a}\right)^2\right)^3\right], & |d| \leq a \\ \frac{a^2}{6}, & |d| > a \end{cases}$$

where the parameter $a = 4.6851\ \widehat{\sigma}$ and where $\widehat{\sigma}$ is a robust estimation of the standard deviation of the inliers. It is usually defined by the Median Absolute Deviation (MAD) $\widehat{\sigma} = 1.4826 r_i$.

Additionally, we constrain the rotation parameters and translation along z within an interval, $[b_l, b_u]$ that we deduced empirically by letting experienced interventional radiologists define slices in the pre-interventional volume being closest to the corresponding CT-fluoro slice. We use the same barrier function 3.1 from the previous chapter penalizing the rotation parameters when approaching the limits

$$b(\mathbf{x}) = \sum_{i=3}^{6} \exp(-\beta(x_i - b_l)(b_u - x_i)) \tag{4.4}$$

where β is a scaling factor controlling the U-shape of the exponential. It is chosen such that the barrier function is near zero inside the interval $[b_l, b_u]$ and very high when approaching the limits. The function to minimize becomes now

$$f(\mathbf{x}) = \sum_{\mathcal{X}_i} \rho\Big[\mathcal{I}^*(\mathcal{X}_i) - \mathcal{I}\left(\widehat{\mathbf{T}}\mathbf{T}(\mathbf{x})\mathcal{X}_i\right) + \lambda b(\mathbf{x})\Big] \tag{4.5}$$

4.2.4. Annealing M-estimator

The annealing M-estimator [63, 64, 65] for our registration problem is defined as following:

$$f_\gamma = \frac{\sum_{\mathcal{X}_i}(h_\gamma(d_i)|d_i|)}{\sum_{\mathcal{X}_i} h_\gamma(d_i)} \tag{4.6}$$

$$d_i = \mathcal{I}^*(\mathcal{X}_i) - \mathcal{I}\left(\widehat{\mathbf{T}}\mathbf{T}\mathcal{X}_i\right) \tag{4.7}$$

where d_i are the intensity differences and h_γ representing an adaptive interaction function. For the properties of those functions and the relationship between M-estimators and the adaptive interaction functions (AIF) see e.g. [65, 63]. We choose following h_γ

$$h_\gamma(\eta) = \frac{1}{1 + \eta^2/\gamma} \quad where \quad \eta = d_i \tag{4.8}$$

4.2.5. Optimization

A Gauss-Newton minimization is used in a multi-resolution approach in order to speed up the process and to help avoiding local minima trap. To minimize the cost function f, we use an iterative-reweighted least squares [112].

To minimize the cost function h, we use a GNC technique [10, 65], starting with a sufficient high γ such that the potential function associated with h is strictly convex. This is called the band of the function [63] and is located between the two extrema of h. It is given by:

$$B_\gamma = [-\sqrt{\gamma}, \sqrt{\gamma}] \tag{4.9}$$

The initial γ needs to satisfy

$$|\eta| = d_i < |\sqrt{\gamma}| \tag{4.10}$$

At each iteration step, γ is then lowered according to a schedule.

Let $\mathbf{d}$ be the vector containing all the intensity differences d_i and $r_i = |d_i - median(\mathbf{d})|$ denote the case median centered intensity difference residuals with associated variance σ_i. The median is calculated according to the median of medians algorithm [11], insuring linear time calculation. Introducing a weight function w by $\rho'(d) = \psi(d) = w(d)\, d$, we arrive at the following weighted equation system to solve

$$\sum_{\mathcal{X}_i} w(r_i/\sigma_i)\, \mathbf{J}_i^\top \mathbf{J}_i \mathbf{x} = \sum_{\mathcal{X}_i} w(r_i/\sigma_i)\, \mathbf{J}_i^\top (d_i + \lambda b(\mathbf{x})) \tag{4.11}$$

where the Jacobian reads

$$\mathbf{J}_i = \frac{\partial r_i}{\partial \mathbf{x}} - \lambda \frac{\partial b(\mathbf{x})}{\partial \mathbf{x}} \tag{4.12}$$

The first term of equation 4.12 stands for the Jacobian of the residual. The second term is substracted from it for the translation along z and rotational parts:

$$\beta(2x_i - b_l - b_u)\exp(-\beta(x_i - b_l)(b_u - x_i)), i = 2, 3, 4, 5 \tag{4.13}$$

Starting from a first order Taylor approximation of the residual, the image gradient is calculated by following equation

$$\left.\frac{\partial \mathcal{I}\left(\widehat{\mathbf{T}}\mathbf{T}(\mathbf{x})\mathcal{X}\right)}{\partial \mathbf{x}}\right|_{\mathbf{x}=\mathbf{0}} = \left.\frac{\partial \mathcal{I}(\widehat{\mathbf{T}}\mathcal{X})}{\partial \mathcal{X}} \cdot \frac{\partial \mathbf{T}\mathcal{X}}{\partial \mathbf{T}} \cdot \frac{\partial \mathbf{T}(\mathbf{x})}{\partial \mathbf{x}}\right|_{\mathbf{x}=0} \tag{4.14}$$

The first term is a (1×3) matrix and represents the gradient of the image corresponding to the projection of the volume at the pose $\widehat{\mathbf{T}}$. The image gradient is computed before the registration process for the whole volume. The second term is a (3×12) matrix, which depends only on the homogeneous coordinates of the considered voxel $\mathcal{X}$

$$\frac{\partial \mathbf{T}\mathcal{X}}{\partial \mathbf{T}} = \begin{bmatrix} x & y & z & 1 & 0 & 0 & 0 & 0 & 0 & 0 & 0 & 0 \\ 0 & 0 & 0 & 0 & x & y & z & 1 & 0 & 0 & 0 & 0 \\ 0 & 0 & 0 & 0 & 0 & 0 & 0 & 0 & x & y & z & 1 \end{bmatrix} = \begin{bmatrix} \mathcal{X}^\top & \mathbf{0} & \mathbf{0} \\ \mathbf{0} & \mathcal{X}^\top & \mathbf{0} \\ \mathbf{0} & \mathbf{0} & \mathcal{X}^\top \end{bmatrix} \tag{4.15}$$

since the gradient generalization to the matrices $\frac{\partial}{\partial \mathbf{T}}$ corresponds to the derivative with respect to each entry of the matrix

$$\mathbf{T}\mathcal{X} = \begin{bmatrix} t1 & t2 & t3 & t4 \\ t5 & t6 & t7 & t8 \\ t9 & t10 & t11 & t12 \\ t9 & t10 & t11 & t12 \end{bmatrix} \begin{bmatrix} x \\ y \\ z \\ 1 \end{bmatrix} = \begin{bmatrix} xt1 + yt2 + zt3 + t4 \\ xt5 + yt6 + zt7 + t8 \\ xt9 + yt10 + zt11 + t12 \\ 1 \end{bmatrix} \tag{4.16}$$

taken line after line. The third term represents the Jacobian of the exponential map with respect to the motion parameters

$$\left.\frac{\partial \mathbf{T}(\mathbf{x})}{\partial \mathbf{x}}\right|_{\mathbf{x}=0} = \left[\begin{array}{cccccc} \mathbf{a}_1 & \mathbf{a}_2 & \mathbf{a}_3 & \mathbf{a}_4 & \mathbf{a}_5 & \mathbf{a}_6 \end{array}\right] \tag{4.17}$$

where $\forall i \in [1,6]$, $\mathbf{a}_i$ is a (12×1) vector containing the entries of the matrix $\mathbf{A}_i$ taken line after line.

4.2.6. Registration results

Here, despite that the projection of the 3D CT-Volume at the initial pose (Fig. 4.2(b)) is far from the reference 2D CT-Fluoro slice (Fig. 4.2(a)), the proposed approach succeeds to converge toward the minimum (Fig. 4.2(c)). The weights image makes it possible to detect the spurious measurements, the noise, the needle presence and the regions suffering from a high contrast differences (see the dark regions in figures 4.2(e), 4.2(f)). Figure 4.2 shows a result of the proposed approach on real data. In this example the M-estimator and AM-estimator give similar results.

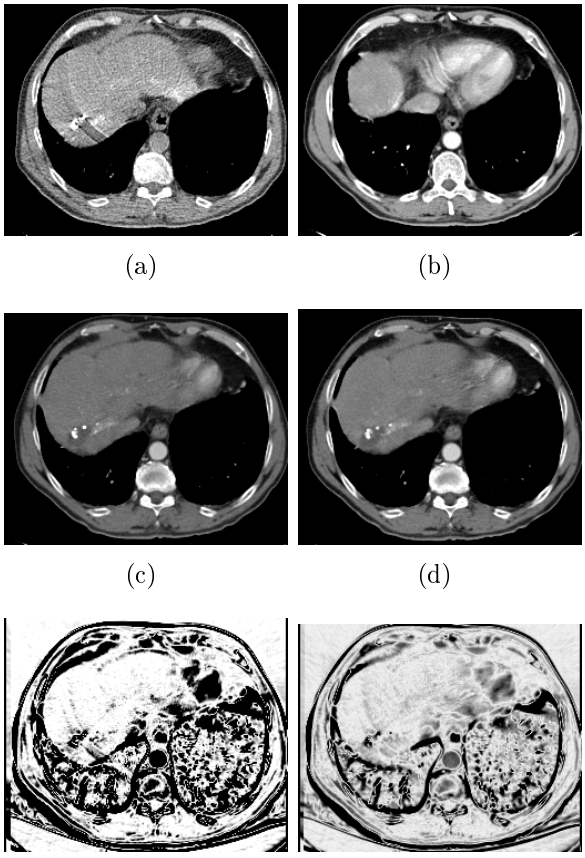

(a) (b)

(c) (d)

(e) (f)

Figure 4.2.: 2D views of registration results on clinical data using M-estimator and AM-estimator. (a) shows the 2D CT-fluoro slice. (b) shows the initial pose in the CT-volume. (c) and (d) show the estimated minimum for the M-estimator respectively AM-estimator (e) shows the weights image at the minimum (dark for small weights and bright for high weights) for the M-estimator. (f) shows the weights image at the minimum (dark for small weights and bright for high weights) for the AM-estimator.

4.3. Adaptive Visualization

For better spatial orientation, and to increase the confidence in the registration result, not only the minimizer of the registration function f is visualized as a 2D view, but also other views "close" to the minimizer. For this, we choose a set of parameters for which the cost function attains almost minimal value. The corresponding views (along with the minimizing view) are then visualized in a smooth animation. We will explain the strategy more precisely, starting with the notion of "close views" in section 4.3.1.

The visualization of the 3D volume on this trajectory brings more information than the single slice. It gives the intuition of slowly exploring the volume in the neighborhood (in real space) of the minimizer. In addition, since the function associating a set of parameters to a 2D view is continuous, projecting the volume with the parameters on this trajectory gives a smooth evolution of the image intensities in the closed loop passing by the minimum (obtained at the registration) and the different points on the isosurface.

4.3.1. Isosurface Sampling

For a given $\alpha \in \mathbb{R}^+$, an isosurface of the cost function f defined in the equation (4.3) is a set $\mathcal{C}(\alpha) \subset \mathbb{R}^6$ given by

$$\mathcal{C}(\alpha) = \{\mathbf{x} \in \mathbb{R}^6 : f(\mathbf{x}) = \alpha\} \tag{4.18}$$

See figure 4.3(a) for an illustration of isosurfaces in $\mathbb{R}^2$ (i.e., isolines). Now, let $\tilde{\mathbf{x}} \in \mathbb{R}^6$ be the estimated minimizer. To find a certain number of parameters $\mathbf{x}_i$ around the minimizer, we use a line search in different directions for points on the isosurface $\mathcal{C}(f(\tilde{\mathbf{x}}) + \varepsilon)$, where ε defines the size of the neighborhood in parameter space. In section 4.4, we explain how, in practice, we choose the directions of the line search and the ε defining the size of the neighborhood. Each of these points corresponds to a certain pose and, therefore, to a certain projection of the volume. We call these views *cost-equivalent projections* (CEPs). See figure 4.3(b) for an illustration of the line search approach and the sampling of an isoline close to the minimizer of a function in $\mathbb{R}^2$. Once the minimizer of the function f is identified and a number of samples on a given isosurface are determined, it is possible to define a trajectory interpolating these points. See Fig. 4.3(b) for an illustration of a such trajectory.

4.3.2. Trajectory Waypoints

In order to visualize the volume smoothly, we first need to find an optimal trajectory from the minimizer through all of the isosurface sample points $\mathbf{x}_i$. Ideally, this trajectory follows the shortest path from the minimizer toward the isosurface, stays on the latter exactly, and aims for the minimizer again.

As the isosurface itself is not analytically known, we use the sample points computed previously as waypoints, and rearrange them in a way that we visit each point

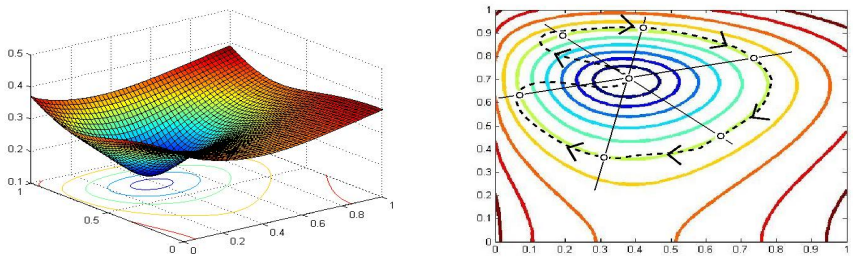

(a) (b)

Figure 4.3.: Trajectories on isosurfaces. (a) a function in $\mathbb{R}^2$ and its isolines. (b) an example of a closed trajectory passing by the minimum of the function and six sample points situated on a certain isoline (obtained by a line search in six directions). This illustrates the concept proposed in this paper in $\mathbb{R}^2$ instead of $\mathbb{R}^6$.

once while following a trajectory of minimal length. We expect this path to be of similar merit in our visualization as the ideal trajectory, while being faster in computation. This task is an old problem of theoretical computer science – the Traveling Salesman Problem (TSP) – and can not be solved deterministically in polynomial time. Therefore, we use the Minimum Spanning Tree (MST) heuristic that guarantees an upper boundary of 200 % of the minimal path length. We currently use the Euclidean norm as distance metric between parameters in $\mathbb{R}^6$.

The MST is built using *Kruskal's Algorithm* [60]. For the MST heuristic, each of the MST's edges are doubled. With *Fleury's Algorithm* [19], we search for an Euler circle in the resulting graph. If nodes are encountered that have been visited before, an additional edge bypassing that node, is created. After this operation, the way from the minimizer through all of the sample points and back to the minimizer is known.

4.3.3. Trajectory Interpolation

Here, we create a smooth path passing by the ordered points $\mathbf{x}_i$ defined above. We interpolate these points in parameter space as elements of the Lie algebra $\mathfrak{se}(3)$ and convert these vectors via the exponential map into the Lie group $\mathbb{SE}(3)$. The transformation matrices denote now the position and orientation of the virtual camera. Since the rotational parameters are small between each CEP, global distortion errors occurring from the flat topology of $\mathfrak{se}(3)$ which is mapped into the non-flat topology of $\mathbb{SO}(3)$ do not occur (cf. [54]). We use piecewise cubic Hermite interpolation [27] to interpolate between the sample points $\mathbf{x}_i$. The desired gradients at these anchor points are approximated by computing the difference between the next and the previous point in relation to the respective anchor point. Having obtained suitable values for $g(0) = \mathbf{x}_i$, $g(1) = \mathbf{x}_{i+1}$, $g'(0) = \mathbf{x}_{i+1} - \mathbf{x}_{i-1}$, and $g'(1) = \mathbf{x}_{i+2} - \mathbf{x}_i$

for two successive anchor points $\mathbf{x}_i,\ \mathbf{x}_{i+1} \in \mathbb{R}^6$, we can compute a cubic polynomial $g : [0,1] \rightarrow \mathbb{R}^6$ that is applied to interpolate between these. Repeating this procedure for all pairs of successive (with respect to the trajectory) points yields a sufficiently smooth curve through the parameter space.

4.4. Experiments and Results

The volume datasets as well as the CT-fluoro slices are downsampled in x and y from 512×512 to 256×256. The registration is performed with a coarse-to-fine strategy, starting at 64×64 and increasing to 128×128 and 256×256. In each run, the estimated values are taken as initialization for the next resolution. The optimization procedure is started from the pose obtained by the DICOM Image Position Patient tag since the patient usually stays on the same table throughout the entire procedure. Also the Reconstruction Diameter was taken into account since the CT-fluoro view is sometimes augmented by reducing the reconstruction diameter. The following experiments were run on a PC with 1.80 GHz Intel Pentium processor and 1 GB of memory. The average time for the registration of the clinical images has been $5.5s$ for the M-estimator and $3.9s$ for the AM-estimator. The computation of the set of solutions on the isosurface has taken in average $15s$. A solution set of 18 sampling points are taken on the isosurface. The points are retrieved from search directions obtained by combinations of out-of-plane parameters, i.e. translation along the z axis, rotations about the x and y axis. Here, six CEPs result from the three out-of-plane parameters in + and - direction, and twelve CEPs result from the combination of each of two parameters in + and - direction.

4.4.1. CEPs generation with M-estimator

More precisely, at every search step in one direction, we are computing the weights based on the actual intensity residuals between the projected slice in the volume and the CT-fluoro slice with the Beaton-Tukey biweight function and include these weights to reach the isosurface. The same procedure is used for the parameter combination to reach the isosurface. The reason for using further a weighted search is that the estimated minimum is not any more a local minimum when the SSD cost function is used.

4.4.2. CEPs generation with AM-estimator

Similar to the M-estimator the weights are calculated according to the chosen AIF and incorporated into the similarity measure to reach the isosurface.

4.4.3. Linking *epsilon* with the volume

Based on results described in the literature, e.g. [21], [99], [9], the deformation in the liver can reach up to $20mm$ from the predicted rigid position, while the

average across tissue yields about $6mm$. Therefore, we would like the CEPs to represent an average movement between $6mm - 7mm$. We start with an initial guess of ε and adapt it until the average motion of all 3D points $\mathcal{X}_i$ considered in the volume between the minimum view and the views at the CEPs fit in the interval $[6mm, 7mm]$. See figure 4.4 for an illustration of the iterative process.

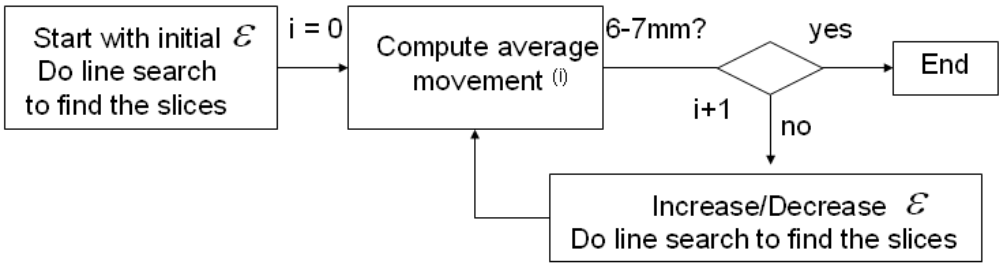

Figure 4.4.: CEP generation process

4.4.4. Experiments on synthetic Slices without Deformation

To test the registration algorithm, we create a set of Ground-Truth (GT) slices simulating a CT-fluoro slice. We use a noisy reconstructed volume [51] from one patient where we extract four slices at different poses including rotations and translations. These noisy slices are registered to the same high resolution pre-interventional volume.

RMS	Translation $[mm]$	Rotation $[°]$
Init	35.7	7.22
M-estimator	0.88	0.28
AM-estimator	0.65	0.03

Table 4.1.: RMS error with respect to the GT slice at the initial position (Init) and registered slices with the M-estimator and AM-estimator.

4.4.5. Experiments on synthetic Slices including Deformation

For deriving synthetic 2D slices that also include deformations, we use two CT-volumes of one patient, the pre- and the post-interventional datasets. The pre-interventional CT-volume, the template volume, is elastically [76] registered to the post-interventional CT-volume, the reference volume. Since after the intervention, the patient is not able to achieve the full inspiration breath-hold as before the intervention, the registration of the pre-interventional to the post-interventional scan is mimicking a possible expiration movement. This post-interventional scan

Pat.	CT-volume		CT-fluoro			
	Image Size	Image Res. [mm]	Image Size	Image Res. [mm]	Slice thick. [mm]	No. img.
1	256x256x212	1.48438x1.48438x1.00	256x256	1.0936x1.0936	6	105
2	256x256x223	1.32813x1.32813x1.00	256x256	1.0936x1.0936	3	110
3	256x256x208	1.32000x1.32000x1.00	256x256	1.4063x1.4063	4	111
4	256x256x212	1.44141x1.44141x1.00	256x256	1.4453x1.4453	3	108
5	256x256x213	1.37891x1.37891x1.00	256x256	1.1719x1.1719	6	100
6	256x256x208	1.06250x1.06250x1.00	256x256	1.0938x1.0938	6	211
7	256x256x219	1.33203x1.33203x1.00	256x256	1.3672x1.3672	3	117
8	256x256x194	1.32031x1.32031x1.00	256x256	1.0938x1.0938	3	144

Table 4.2.: Description of datasets

is not used for the next steps, only the deformed volume. The displacement field for the achieved deformation maps the voxels of the deformed volume into the pre-interventional scan. In this way, by extracting axial slices of this deformed volume, adding noise (cf. [129]), and adding for some of them a previously segmented needle of real CT-fluoro slice, each of these slices represent hypothetical CT-fluoro slices. Six axial slices are extracted every $1cm$, and we run the robust minimization for each of them. Figure 4.6 shows such a registration result. For each synthetic CT-fluoro slice, each voxel is mapped into the pre-interventional volume resulting in a deformation surface.

Starting with an initial guess of $\varepsilon = 0.25$ the corresponding average movements and ε are shown in the table below:

Slice	1	2	3	4	5	6
$RMS[mm]$	6.38	6.37	6.52	6.60	6.06	6.56
ε	0.3	0.25	0.3	0.3	0.25	0.3

Visually, we clearly see that the deformation of all slices of the liver voxels is included by the estimated CEPs.

4.4.6. Experiments on clinical Data

We evaluate datasets of eight different patients. The datasets have been routinely acquired using a Sensation 16 and Sensation 4 scanner (Siemens AG, Forchheim). Table 4.2 summarizes the image details.

4.4.7. Evaluation of the Registration Results

Visual assessment of all 880 registrations has been carried out by automatically loading the slices and the corresponding result. Criterias that have been taken into

	M-Estimator		AM-Estimator	
Patient	Avg time [s]	Failure rate [%]	Avg time [s]	Failure rate [%]
1	8.65	0	14.31	0
2	6.4	9.89	14.68	11
3	4.97	0	2.74	0
4	7.48	27	9.41	1.85
5	9.35	0	10.04	5
6	7.00	8.82	3.63	0
7	4.78	18.81	2.69	0
8	7.88	1.81	8.86	.9

Table 4.3.: Registration results for M-estimator and AM-estimator

account are the shape of the liver, ligamentum falciforme in the liver, gallbladder, the lesions, spleen, the right kidney, and other patient specific landmarks like calcifications[1]. Unsatisfactory results have been noted and further assessed. Note that due to the involved deformation (breathing, needle pressure), we are not aiming at a perfect match. Our goal is to show the relevant areas, respectively all information that occurs for the liver in the CT-fluoro slice. When structures which are present in the CT-fluoro slice had not been found in the estimated slice, a search of 10mm in the normal direction of the registered plane has been performed. In our further automatic visualization (section 4.3.3), we consider all out-of-plane parameters and combinations of them and not only the normal direction. Table 4.3 summarizes the registration results. We have also shown samples of these results to our clinical partners and their evaluation agreed with ours. In some cases a failure rate of 27% has occured so the use of the Levenberg-Marquardt algorithm or Trust region optimization (see appendix A) might provide better results and could be further assessed. Both algorithms are more robust to a highly non-convex cost surface.

4.4.8. Generation of CEPs

For each of the 8 datasets, we use 3 CT-fluoro slices which results in 24 examples. The CEPs are generated for each slice starting with an $\varepsilon = 0.2$ for the M-estimator and $\varepsilon = 0.25$ for the AM-estimator. A linear model of the increase/decrease of ε with respect to the RMS error is assumed. This is not true for all examples resulting in an increase of iterations which has been 4. Since the calculations along the out-of-plane parameter axes are independent, the whole procedure can be parallelized. Figure 4.8 shows a 3D view of the generated CEPs for a slice of patient 3 where the registration of the AM-estimator has been rated as successful. The result of the M-estimator has not been rated successful because the spleen which is present in the CT-fluoro slice, is not present in the estimated minimum. Figures 4.9 and 4.10 show the 2D views of all 18 CEPs. In this example, the registration employing the

[1]See liver ablation workflow in section 1.1.1

M-estimator has been trapped in a local minimum. In figure 4.8(b), we see that there are three planes outside the bundle. These planes represent the images shown in the 2D view represented by 4.10(i), 4.10(m), 4.10(s) which all contain the spleen that was not captured.

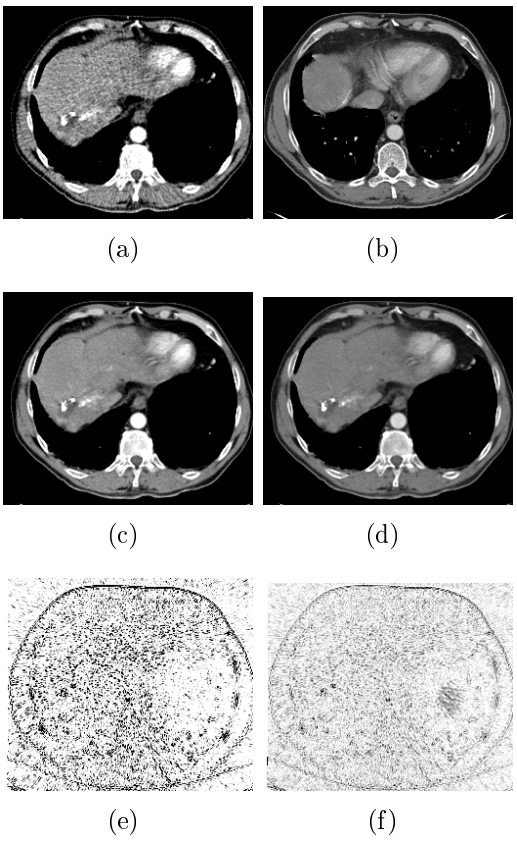

Figure 4.5.: 2D views of registration results for synthetic slices without deformation. (a) shows a 2D CT synthetic slice including noise. (b) shows the starting position for optimization with an RMS of 20.12mm for translation and 5.4° for rotation. (c) shows the estimated minimum (M-estimator) with an RMS of 0.86mm for translation and 0.004° for rotation. (d) shows the estimated minimum (AM-estimator) with an RMS of 0.08mm for translation and 0.0009° for rotation.(e) and (f) show the weights image in the estimated minimum for the M- and AM-estimator respectively.

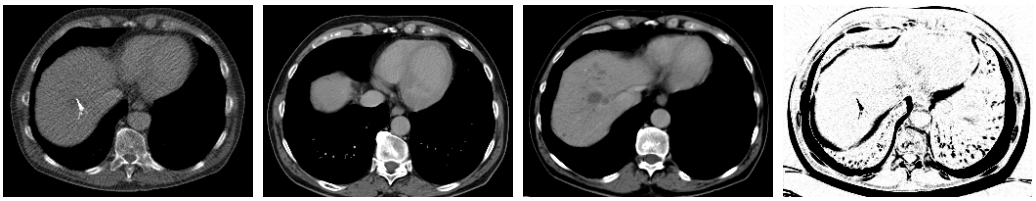

(a) (b) (c) (d)

Figure 4.6.: 2D views (M-estimator). (a) shows a 2D CT synthetic slice including deformation, noise and needle. (b) shows the same axial position in the pre-interventional volume as the position where the synthetic slice was extracted in the deformed volume. This position is used as starting position for optimization. (c) shows the estimated minimum. (d) shows the weights image in the estimated minimum.

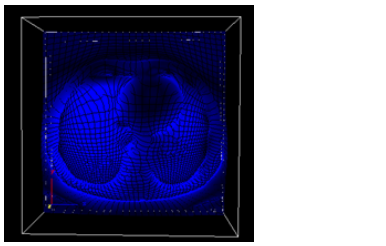

(a)

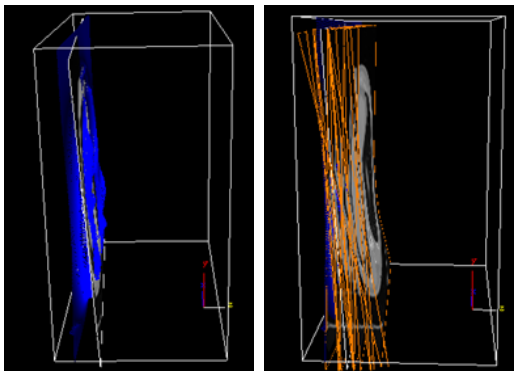

(b) (c)

Figure 4.7.: 3D views of the example showed in fig.4.6. (a) shows an axial view of the deformed surface where the cranio-caudal depth is coded from dark to light. (b) shows a saggital view on the recovered deformed surface and the estimated minimum slice intersecting the surface. (c) shows the same configuration as (b) from different viewpoints plus the CEPs at an average movement of $6.56mm$ and $\varepsilon = 0.3$. All the liver voxels are included into the volume defined by the CEPs.

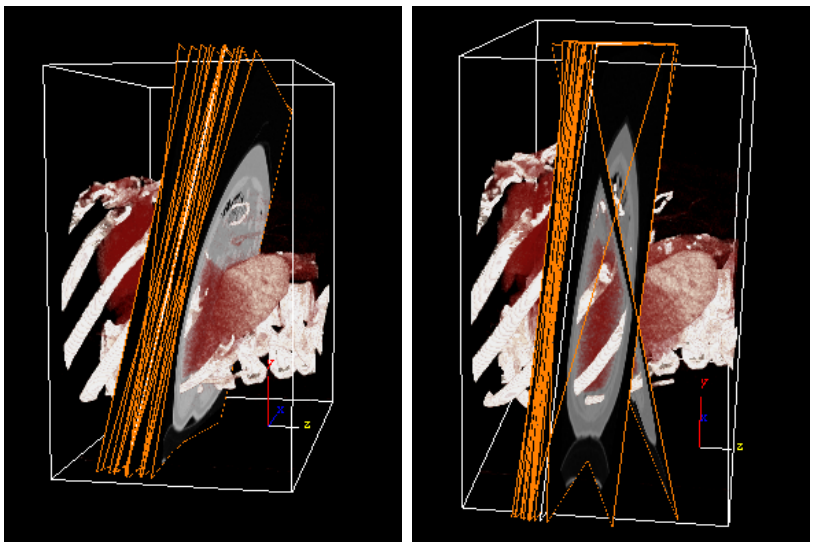

(a) (b)

Figure 4.8.: 3D views of the generated CEPs. (a) AM-estimator (b) M-estimator. Notice that in the case of the M-estimator which was rated as not successful there are three planes outside the bundle. These correspond to projections where the spleen is captured, as it is present in the CT-fluoro slice. The CT-fluoro slice for this case is shown in figures 4.9(a) or 4.10(a). The slices are shown in a 2D view in figure 4.10 and correspond to the figures 4.10(j), 4.10(n) and 4.10(t). Note that they are located in the subvolume which is identified as the solution subvolume.

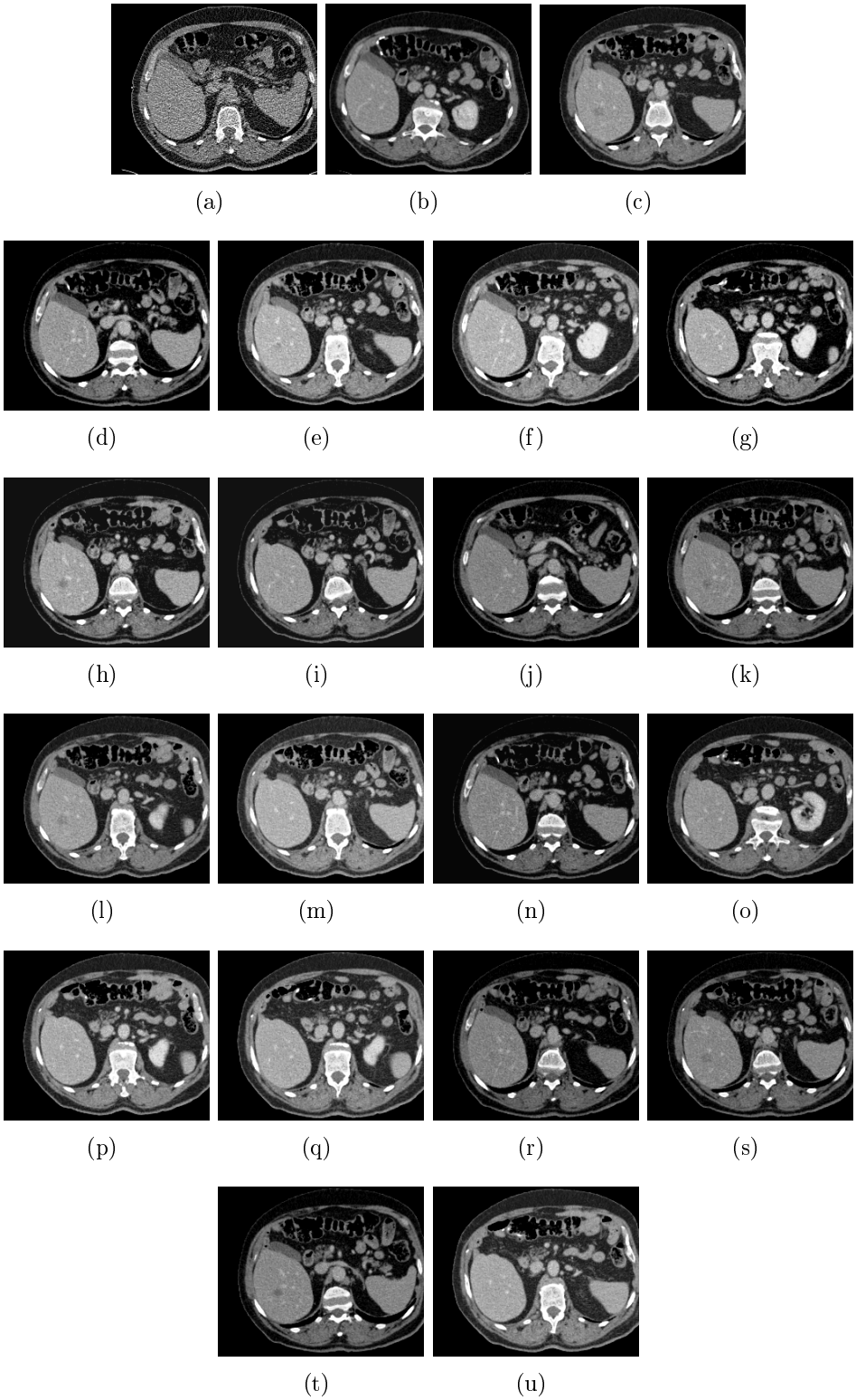

Figure 4.9.: AM-estimator: (a) represents the CT-fluoro slice. (b) represents the initial pose in the volume. (c) represents the estimated minimum. From (d) to (u): the 2D views represent CEPs.

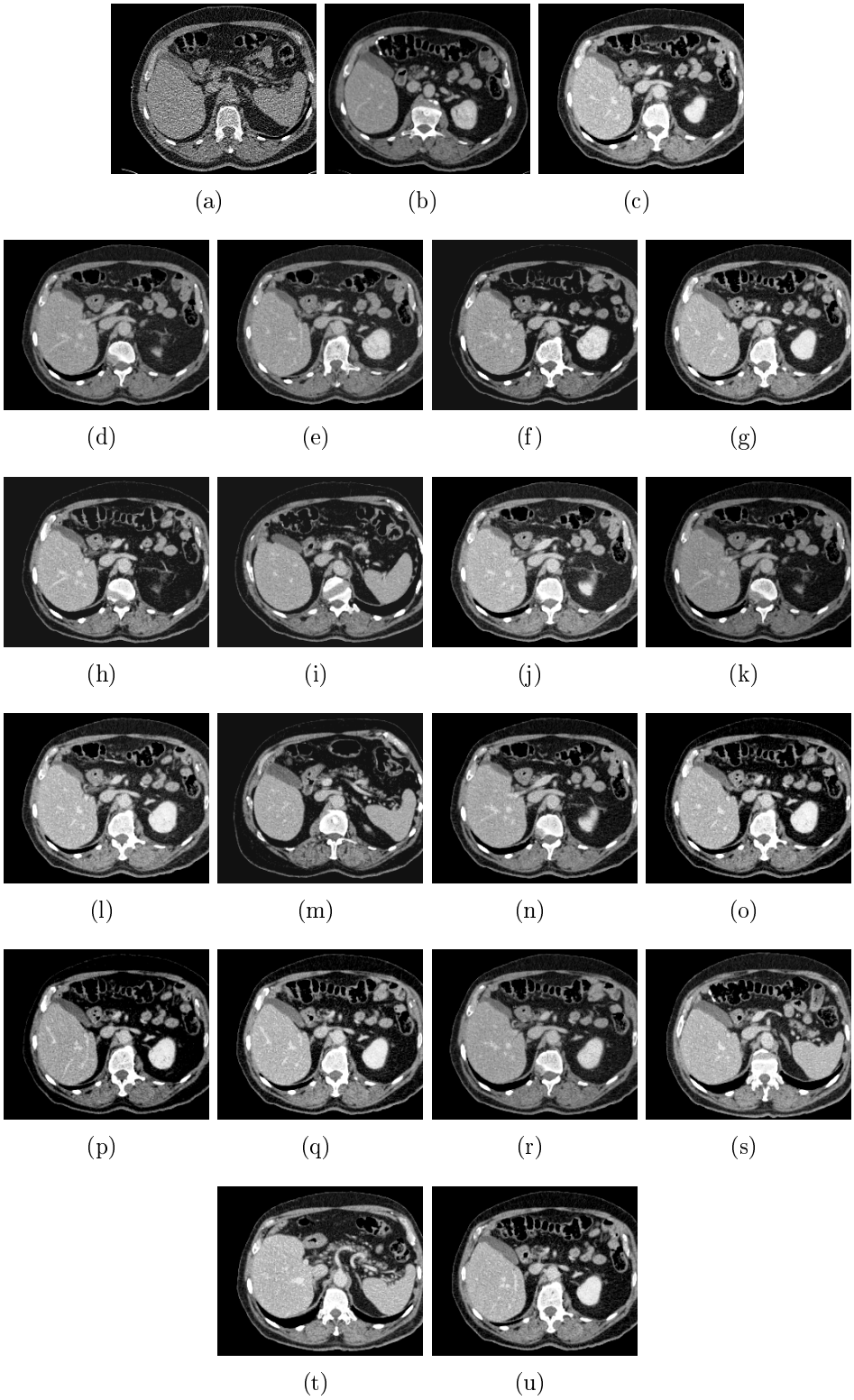

Figure 4.10.: M-estimator: (a) represents the CT-fluoro slice. (b) represents the initial pose in the volume. (c) represents the estimated minimum (note that the spleen is not captured). From (d) to (u): the 2D views represent CEPs.

4.5. Evaluation of adaptive Visualization

Three experienced interventional radiologists have evaluated independently the CEP visualization versus the visualization of a single slice for the case of M-estimators. Six datasets have been assessed with corresponding three CT-fluoro slices, resulting in eighteen examples. Two of the radiologists have considered, in all eighteen cases (100%), the CEP visualization more valuable than one slice. One of them has voted for the CEP visualization in eleven examples (61%).

4.6. Discussion

In this chapter, we have presented two robust slice-to-volume registration methods to overcome the noise and the difference between the conditions of the pre-interventional and the interventional acquisitions. The methods have been evaluated with simulations on synthetic noisy slices with and without deformations. We have also extensively evaluated the registration results on clinical data since our proposed adaptive visualization relies on a good registration result. The visualization has included views of the CT-volume determined along flat directions of the out-of-plane motion parameters next to the minimum pose, where the optimization encounters uncertainty. The views have been generated at poses that represent an average movement reported in the literature. In this way, the deformation caused by the breathing could have been included in the volume defined by the views. Segmentation of the liver would contribute to a better accuracy of the subvolume estimation. Now, the average movement of voxels is computed for a rectangular mask (which is automatically detected) in which the whole body is considered. The proposed method has given very good results in a reasonable time with a standard computer. Furthermore, it can be run in parallel threads since the line search is done on independent directions from each other speeding up the process of visualization.

The result of the registration and the adaptive visualization have been assessed by three experienced interventional radiologists on clinical CT-fluoro data[2]. The evaluation outcome supports that such visualization in the intervention room allows the examiner to orientate himself better and estimate more accurately the path to the lesion. This is because all relevant features (vessels and lesion(s)) of the liver were present in the CEP visualization. The neighborhood assessment helps to know in which direction to further perform and how to angulate the needle. A single slice in the CT-volume will confirm or not the right position, but it misses further guidance and neighborhood assessment. On the other hand, this visualization ties up to the familiar view in the radiology. By permitting interaction, a user interface further improves the usability of the proposed approach. Finally, in addition to the proposed visualization, a display for the scale of distance to the target and a 3D coronal view for incorporating the cranio-caudal direction eases the perception of depth and orientation of the needle.

[2]The evaluation has been performed only for the case of M-estimators

CHAPTER

FIVE

ADAPTIVE VISUALIZATION BASED ON EIGENANALYSIS OF SLICE-TO-VOLUME SIMILARITY FUNCTION

5.1. Introduction

SIMILAR to the previous chapter 4, we start from an already detected minimum pose in the CT-volume and analyze the six-dimensional cost surface in order to detect its structure. Since some of the registration parameters impose stronger constraints than the others, we therefore expect to see a higher-dimensional valley roughly pointing into the directions of the weak parameters. We seek a trajectory along the cost function valley floor and thus capture the parameters for which the similarity measure is not changing much, i.e. the parameters which impose most uncertainty when searching a solution in the CT-volume. In order to find this valley, we apply algorithms from computational chemistry that we adapt for our needs, as well as a newly developed adaptive eigenvector step (EV-step) method.

When analyzing a cost function surface for a CT-volume and a perfectly matching fluoro slice, we expect to find a well-defined global minimum, that is a clear funnel-like shape of the surface. However, the deformations caused by breathing will add a considerable amount of fuzziness. Figures 5.1(a) and 5.1(b) show the cost function for the out-of-plane parameters z translation (cranio-caudal direction) and x rotation (with respect to an axial CT slice). Figure 5.1(a) shows the cost potential for a synthetic slice at a rigid pose from the volume – a small but sharp trough at the minimum. Figure 5.1(b) shows the cost function for a synthetic slice with deformations: the trough is wider and rather flat at the center. We suppose that by detecting the fuzziness or flatness and visualizing that area, we will also recover the deformation volume. This expectation coincides with the 'weak perspective' around the minimum observed by Birkfellner et al. [6] when analyzing different cost functions for slice-to-volume registration for the same application. The 'weak perspective' is similar to the DRR-based registration, where the uncertainty arrives at the translation along the direction of the normal beam. In contrast to our proposed

solution, the authors suggest a second slice as solution to this problem since the new generation of multislice CT-scanner already provide this functionality.

For detecting this 'weak perspective', we need to analyze the cost surface in the neighborhood of the optimum that was already found using numerical optimization. The local shape of the cost potential can be described by second order derivatives.

Analysis of the second order derivative is extensively used for pattern analysis where the structure of a point can be described by taking into account its neighborhood. It is known as structure tensor [41, 33]. In [39], Hessian analysis of the cost function at the minimum is performed to better understand the training of neural networks. In the same community, the thesis of Gallagher [35] analyzes the error surface (cost surface) by Principal Component Analysis (PCA) and proposes a trajectory visualization of the learning path, as well as sampling techniques.

In the context of monocular human tracking, [111] presents two methods to build roadmaps linking local minima on a cost surface. The first uses a trust region damped Newton method along the eigendirections of the cost function. The other one uses a constrained optimization, in particular a quadratic sequential optimization, along an evolving hypersurface to track saddle points and minima within it. In computational chemistry, the path between minima passing through saddle points on an energy potential encodes the minimal energy such that a reaction can occur. Many publications exist that aim for its determination, such as [48], [95]. A review of methods used in this field can be found in [4].

In our context, the trajectory path connects local minima in the neighborhood of the initially found optimum and passes through saddle points. Fluctuations caused by the deformation will thus be passed and other potential solutions to our registration problem will be found. A trajectory planning method will identify those motion parameters for which the similarity measure is not changing much, i.e. the motion parameters which impose most uncertainty. As a single six-dimensional point in parameter space uniquely identifies a coordinate frame in three-dimensional space and thus a slice in the original CT-volume, we can convert such a path into a smooth animation sequence of slices.

In contrast to this plan, figure 5.1(b) suggests to explore all directions around the minimum to capture the deformation as our expectation of a valley may not necessarily apply. However, as we plan to convert the path into an animation sequence, a set of multiple trajectories will be hard to display. A visualization along one dominant path of uncertainty will be much simpler generated and much easier understood by the interventional radiologists. A single one-dimensional subspace will thus suffice in our application.

In section 5.2, we present our employed similarity measures and their derivatives. In the sequel, in section 5.4, two methods for moving along the valley floor of the cost surface are introduced. The first method performs iterative motions along the eigenvector corresponding to the smallest eigenvalue and subsequently corrects the position using a linesearch orthogonal to the original direction. The second method has been adopted from [95] and adapted for our application. Similarly to the first method, the latter relies on the correction of a predicted step. After introducing

our methods in sections 5.4.1 and 5.4.2, we present a performance evaluation on mathematical models and on real registration data.

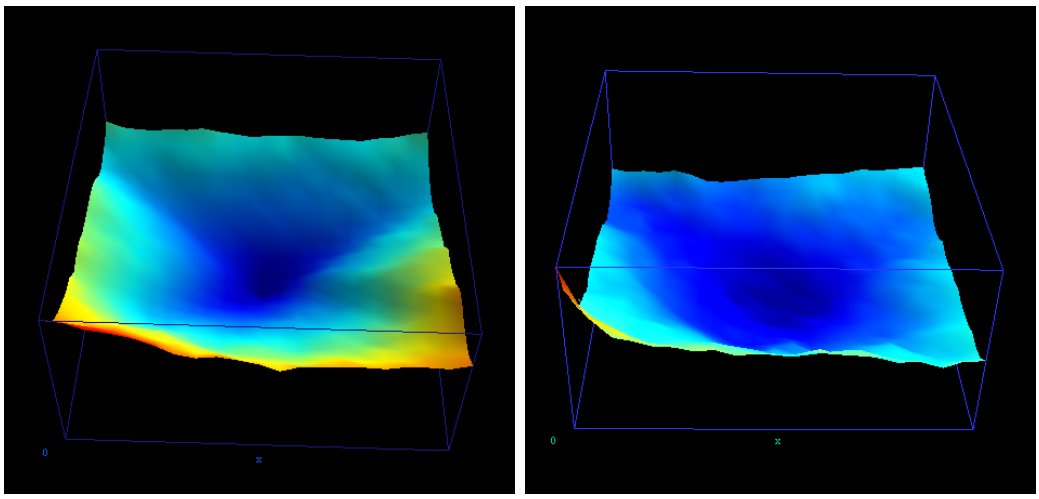

(a) Sharp trough (b) Fuzzy trough

Figure 5.1.: Cost function plot using the Beaton-Tukey M-estimator for the out-of-plane parameters – translation along the z axis and rotation around the x axis. (a) shows a small but sharp funnel as the synthetic slice was not deformed whereas (b) shows a fuzzy area since the synthetic slice contains deformation. The information of the CT-fluoro slice is thus dispersed into a subvolume of the CT data set.

5.2. Cost Functions

Consider the case when f is based on the sum of squared differences (SSD) between a fixed image $\mathcal{I}^*$ and a slice $\mathcal{I}$ resampled from a CT-volume at a pose described by a six-dimensional parameter vector $\mathbf{x}$. The sum is computed over all image voxels $\mathcal{X}$ as

$$f(\mathbf{x}) = \sum_{\mathcal{X}} \rho(d_{\mathcal{X}}(\mathbf{x})) \tag{5.1}$$

with

$$\rho : \mathbb{R} \to \mathbb{R},$$

for instance

$$\rho(d) = \frac{1}{2}\|d\|^2,$$

and

$$d_{\mathcal{X}}(\mathbf{x}) = \mathcal{I}^*(\mathcal{X}) - \mathcal{I}(\mathbf{T}(\mathbf{x})\mathcal{X}).$$

5.2.1. First Derivative

The first derivative of the cost function (5.1) reads:

$$\begin{aligned}
\frac{\partial f(\mathbf{x})}{\partial \mathbf{x}} &= \sum_{\mathcal{X}} \frac{\partial \rho(d_{\mathcal{X}}(\mathbf{x}))}{\partial \mathbf{x}} && (5.2)\\
&= \sum_{\mathcal{X}} \rho'(d_{\mathcal{X}}(\mathbf{x})) \cdot \frac{\partial d_{\mathcal{X}}(\mathbf{x})}{\partial \mathbf{x}} && (5.3)\\
&= \sum_{\mathcal{X}} \rho'(d_{\mathcal{X}}(\mathbf{x})) \cdot \frac{\partial (\mathcal{I}^*(\mathcal{X}) - \mathcal{I}(\mathbf{T}(\mathbf{x})\mathcal{X}))}{\partial \mathbf{x}} && (5.4)\\
&= \sum_{\mathcal{X}} \rho'(d_{\mathcal{X}}(\mathbf{x})) \cdot (-1) \cdot \frac{\partial \mathcal{I}(\mathbf{T}(\mathbf{x})\mathcal{X})}{\partial \mathbf{x}} && (5.5)\\
&= -\sum_{\mathcal{X}} \rho'(d_{\mathcal{X}}(\mathbf{x})) \cdot \frac{\partial \mathcal{I}(\mathbf{T}(\mathbf{x})\mathcal{X})}{\partial \mathbf{x}}. && (5.6)
\end{aligned}$$

The second factor of each summand – subsequently referred to as $\mathbf{J}_{\mathcal{X}}(\mathbf{x})$ – is

$$\frac{\partial \mathcal{I}(\mathbf{T}(\mathbf{x})\mathcal{X})}{\partial \mathbf{x}} = \frac{\partial \mathcal{I}(\mathbf{T}(\mathbf{x})\mathcal{X})}{\partial \mathbf{T}(\mathbf{x})\mathcal{X}} \cdot \frac{\partial \mathbf{T}(\mathbf{x})\mathcal{X}}{\partial \mathbf{T}(\mathbf{x})} \cdot \frac{\partial \mathbf{T}(\mathbf{x})}{\partial \mathbf{x}} =: \mathbf{J}_{\mathcal{X}}(\mathbf{x}). \tag{5.7}$$

$\mathbf{J}_{\mathcal{X}}(\mathbf{x})$ is the Jacobian of the image $\mathcal{I}$ at the transformation $\mathbf{T}(\mathbf{x})$. The first term of $\mathbf{J}_{\mathcal{X}}(\mathbf{x})$ represents the image gradient at the pose defined by the transformation. The second term represents the derivative with respect to the homogenous coordinates and the third term represents the derivative with respect to the parametrization of the motion.

5.2.2. Second Derivative

Likewise, the second derivative of the cost function (5.1) reads:

$$\begin{aligned}
\frac{\partial^2 f(\mathbf{x})}{\partial^2 \mathbf{x}} &= -\sum_{\mathcal{X}} \frac{\partial (\rho'(d_{\mathcal{X}}(\mathbf{x})) \cdot \mathbf{J}_{\mathcal{X}}(\mathbf{x}))}{\partial \mathbf{x}} && (5.8)\\
&= -\sum_{\mathcal{X}} \frac{\partial \rho'(d_{\mathcal{X}}(\mathbf{x}))}{\partial \mathbf{x}} \cdot \mathbf{J}_{\mathcal{X}}(\mathbf{x}) + \rho'(d_{\mathcal{X}}(\mathbf{x})) \cdot \frac{\partial \mathbf{J}_{\mathcal{X}}(\mathbf{x})}{\partial \mathbf{x}} && (5.9)\\
&= \sum_{\mathcal{X}} \rho''(d_{\mathcal{X}}(\mathbf{x}))\ \mathbf{J}_{\mathcal{X}}(\mathbf{x})^{\top} \mathbf{J}_{\mathcal{X}}(\mathbf{x}) - \rho'(d_{\mathcal{X}}(\mathbf{x})) \cdot \frac{\partial \mathbf{J}_{\mathcal{X}}(\mathbf{x})}{\partial \mathbf{x}}. && (5.10)
\end{aligned}$$

The second factor of the subtrahend – subsequently referred to as $\mathbf{H}_{\mathcal{X}}(x)$ – reads:

$$\begin{aligned}
\frac{\partial \mathbf{J}_{\mathcal{X}}(\mathbf{x})}{\partial \mathbf{x}} &= \frac{\partial^2 \mathcal{I}(\mathbf{T}(\mathbf{x})\mathcal{X})}{\partial^2 \mathbf{x}} && (5.11)\\
&= \left(\frac{\partial^2 \mathcal{I}(\mathbf{T}(\mathbf{x})\mathcal{X})}{\partial^2 \mathbf{T}(\mathbf{x})\mathcal{X}} \cdot \frac{\partial \mathbf{T}(\mathbf{x})\mathcal{X}}{\partial \mathbf{T}(\mathbf{x})} \cdot \frac{\partial \mathbf{T}(\mathbf{x})}{\partial \mathbf{x}} \right)^{\top} \cdot \frac{\partial \mathbf{T}(\mathbf{x})\mathcal{X}}{\partial \mathbf{T}(\mathbf{x})} \cdot \frac{\partial \mathbf{T}(\mathbf{x})}{\partial \mathbf{x}} && (5.12)\\
&=: \mathbf{H}_{\mathcal{X}}(\mathbf{x}). && (5.13)
\end{aligned}$$

5.3. Simplifications

For a constant $\rho'' = c$, formula (5.10) can be rewritten as

$$\frac{\partial^2 f(\mathbf{x})}{\partial^2 \mathbf{x}} = c\ \mathbf{J}(\mathbf{x})^\top \mathbf{J}(\mathbf{x}) - \sum_{\mathcal{X}} \rho'(d_{\mathcal{X}}(\mathbf{x})) \cdot \mathbf{H}_{\mathcal{X}}(\mathbf{x}) \tag{5.14}$$

with $\mathbf{J}(\mathbf{x})$ denoting the stacked up $\mathbf{J}_{\mathcal{X}}(\mathbf{x})$'s.

5.3.1. SSD – Sum of squared Differences

$$\rho(d) = \frac{1}{2} d^2 \tag{5.15}$$

$$\rho'(d) = d \tag{5.16}$$

$$\rho''(d) = 1 \tag{5.17}$$

When using this formula for ρ, the simpler equation (5.14) holds and writes as

$$\frac{\partial^2 f(\mathbf{x})}{\partial^2 \mathbf{x}} = \mathbf{J}(\mathbf{x})^\top \mathbf{J}(\mathbf{x}) - \sum_{\mathcal{X}} d_{\mathcal{X}}(\mathbf{x}) \cdot \mathbf{H}_{\mathcal{X}}(\mathbf{x}). \tag{5.18}$$

5.3.2. Beaton-Tukey

$$\rho(d) = \begin{cases} \frac{a^2}{6}\left(1 - \left(1 - \left(\frac{d}{a}\right)^2\right)^3\right), & |d| \le a \\ \frac{a^2}{6}, & |d| > a \end{cases} \tag{5.19}$$

$$\rho'(d) = \begin{cases} d\left(1 - \left(\frac{d}{a}\right)^2\right)^2, & |d| \le a \\ 0, & |d| > a \end{cases} \tag{5.20}$$

$$\rho''(d) = \begin{cases} 1 - 6\left(\frac{d}{a}\right)^2 + 5\left(\frac{d}{a}\right)^4, & |d| \le a \\ 0, & |d| > a \end{cases} \tag{5.21}$$

5.4. Methods

In order to evaluate the quality of a cost function

$$f(\mathbf{x}) : \mathbb{R}^n \to \mathbb{R},$$

the second derivative with respect to the parameter vector $\mathbf{x}$

$$\frac{\partial^2 f(\mathbf{x})}{\partial^2 \mathbf{x}} : \mathbb{R}^n \to \mathbb{R}^{n \times n},$$

is computed at a previously found minimum $\mathbf{x}_0$ and evaluated using eigenvalue decomposition. The eigenvector $\mathbf{v}_{min}$ corresponding to the smallest eigenvalue λ_{min} points into the direction of f's smallest variance.

The Taylor expansion of $f(\mathbf{x})$ around the optimum $\mathbf{x}_0$ is

$$f(\mathbf{x}) = f(\mathbf{x}_0 + \Delta\mathbf{x}) \approx f(\mathbf{x}_0) + \left(\frac{\partial f}{\partial \mathbf{x}}(\mathbf{x}_0)\right)^\top (\Delta\mathbf{x}) + \frac{1}{2}(\Delta\mathbf{x})^\top \left(\frac{\partial^2 f}{\partial^2 \mathbf{x}}(\mathbf{x}_0)\right)(\Delta\mathbf{x}) + ...$$

For an analysis of the smallest change only the third term matters as the first can be discarded as constant and the second term depends on the first derivative that is supposed to equal $\mathbf{0}$ in the optimum $\mathbf{x}_0$. The Taylor expansion can be rewritten for $\mathbf{x} = \mathbf{x}_0 + \mathbf{v}_{min}$ as

$$f(\mathbf{x}_0+\mathbf{v}_{min}) \approx f(\mathbf{x}_0)+\frac{1}{2}(\mathbf{v}_{min})^\top \left(\frac{\partial^2 f}{\partial^2 \mathbf{x}}(\mathbf{x}_0)\right)(\mathbf{v}_{min}) \approx f(\mathbf{x}_0)+\frac{1}{2}(\mathbf{v}_{min})^\top \lambda_{min}(\mathbf{v}_{min}).$$

Consequently, a small eigenvalue directly corresponds to a small change of the function value. This relationship is also valid outside the minimum when the gradient is constant e.g. on a flat surface. In any other case where the cost function will increase, we would like to stay on the valley floor of the cost surface. Therefore, even if the gradient is not zero any more, its variation should be kept as small as possible. A first order approximation of the gradient is $\mathbf{g}_f(\mathbf{x}_0 + \Delta\mathbf{x}) = \mathbf{g}_f(\mathbf{x}) \approx \mathbf{g}_f(\mathbf{x}_0) + \mathbf{H}_f(\mathbf{x}_0)\Delta\mathbf{x}$. Here again, the smallest variation of the gradient occurs in the direction of the eigenvector corresponding to the smallest eigenvalue.

In the next sections the methods ensuring that the trajectory path continues along the valley floor are described.

5.4.1. Trajectory Path using EV-Step

Starting from a minimum found previously, we compute an eigenvalue decomposition of the Hessian of the cost function at this location. We move a small step away from that minimum in the negative and positive direction of the eigenvector corresponding to the smallest eigenvalue. At the new point $\mathbf{x}_{t+1}$, we apply a linesearch orthogonal to the trajectory path in order to correct the deviation. The final points will reside on the valley floor again. Note that if the valley floor can be approximated by a linear path, the eigenvector step will yield a point on the valley floor right away that does not need to be corrected. We repeat this process at the new end points using the same rule until further exploration is not useful any more.

Adaptive step size. During the iteration, an adaptive step size is computed. We start with a small step value and iteratively increase the step length as long as the eigenvector corresponding to the smallest eigenvalue at the current point $\mathbf{x}_k$ coincides with the gradient at the new estimated point $\mathbf{x}_{t+1}$ up to a small deviation. We are sure hence to move along the valley floor ([48], [95]). See figure 5.2 for an illustration of the linesearch concept.

5.4.2. Trajectory Path using TASC

We use a slightly adapted implementation of the TASC (Tangent Search Concept) algorithm proposed by Quapp [95] which generates a path along the valley floor

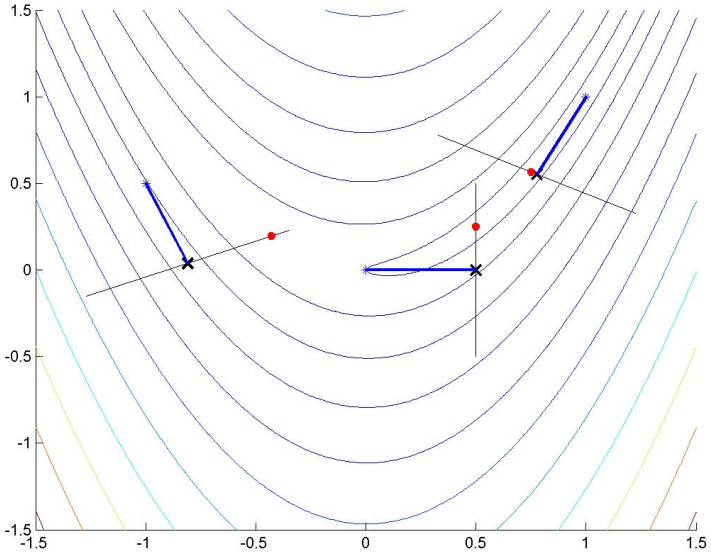

Figure 5.2.: The blue star marks the starting point, the black cross marks the point which results from the EV-step. The red point is the corrected location using the linesearch marked as a black line

gradient extremal. Gradient extremals [48] are curves where the gradient is an eigenvector of the Hessian of the cost surface. This results from the minimization of the gradient norm over a level set on the surface [95]. The TASC method handles curved reaction paths very well. The original proposal consists of two consecutive steps that generate a new point on the valley floor $\mathbf{x}_{k+1}$ from a point $\mathbf{x}_k$ and a search direction $\mathbf{r}_k$. Iterating over k, a complete path along the valley floor can be computed.

Initialization. Before starting the iteration, we need to generate useful initial seed points and search directions that fulfill the requirements imposed by TASC. As the procedure is gradient based, it is not possible to start at the minimum directly. We use the method described in 5.4.1 to move a small step away from that minimum in the negative and positive direction of the eigenvector corresponding to the smallest eigenvalue. Starting at the minimum $\mathbf{x}_0$, we generate two start points $\mathbf{x}_{\pm 1} = \mathbf{x}_0 \pm C\mathbf{v}_{min}$ and two corresponding initial search directions $\mathbf{r}_{\pm 1} = \pm\mathbf{v}_{min}$. These values are stored in a FIFO structure.

Iteration. For each entry in the queue, the two TASC steps are executed. Let the current seed point be denoted as $\mathbf{x}_k$ and the current search direction as $\mathbf{r}_k$. The first step is the *predictor* step that attempts a preliminary move along a Newton trajectory. A tangent direction $\mathbf{t}_k$ of unit length is computed as the null space of

$\mathbf{P}_{\mathbf{r}_k}\mathbf{H}_f(\mathbf{x}_k)$ using singular value decomposition, i.e. $\mathbf{P}_{\mathbf{r}_k}\mathbf{H}_f(\mathbf{x}_k)\mathbf{t}_k = 0$, with $\mathbf{P}_{\mathbf{r}_k} := \mathbf{I}_n - \mathbf{r}_k\mathbf{r}_k^\top$ denoting the orthogonal projection on the orthogonal complement of $\mathbf{r}_k$. In order to roughly move into the same direction as in the previous step, the tangent vector is constrained to point into the direction provided by the original search direction. Using the tangent and an adaptive step length s_k as described in section 5.4.1, the position is updated as $\mathbf{x}_k + s_k\mathbf{t}_k$. This position is augmented in a *corrector* step that optimizes the cost function $\mathbf{P}_{\mathbf{t}_k}\mathbf{g}_f(\mathbf{x}) = 0$ using Newton-Raphson steps, starting at the intermediate position computed in the predictor step. The result of this operation is stored as $\mathbf{x}_{k+1}$. If further exploration makes sense, $\mathbf{r}_{k+1} := \mathbf{t}_k$ and $\mathbf{x}_{k+1}$ are added to the queue to serve as seed for a later iteration. The queue structure enables us to create a very generic and flexible framework that allows to follow bifurcations by adding two tasks to the queue at such a point.

5.4.3. Path Visualization and Constraints

As stated above, a smooth interpolation between the poses on the trajectory is used to render an animation sequence of slices, starting at the minimum pose, passing through slices defined by path nodes, and returning back to the minimum. This approach imposes certain restrictions on the path. A first consequence is the desire to avoid sharp turns on the path trajectory. In order to guarantee a smooth camera flight, the path is abandoned in this case. Another stopping criterion, which we also used in the previous chapter in section 4.4.3, is an average relative motion of the voxels belonging to the slices generated at the respective trajectory points of more than $7mm$ with respect to the minimum rigid pose. We thus ensure that only relevant information corresponding to the CT-fluoro reference slice is retrieved and presented during the visualization of excerpts of the high resolution CT data.

5.5. Evaluations on analytical Surfaces

5.5.1. Results using EV-Step with Linesearch Correction

For analytical experiments we use the Rosenbrock function for the two dimensional case which has one minimum at $(1, 1)$:

$$f(x, y) = 100\left(y - x^2\right) + (x - 1)^2$$

We also use the Mueller-Brown triple-well potential surface from computational chemistry which has often been used as a benchmark for optimization algorithms. It has three minima $\mathbf{m}_1 = (0.6235, 0.0280)$, $\mathbf{m}_2 = (-0.0500, 0.4667)$, and $\mathbf{m}_3 = (-0.5582, 1.4418)$ and two saddle points $\mathbf{s}_1 = (0.21249, 0.29299)$, and $\mathbf{s}_2 = (-0.822, 0.62431)$.

$$V(x, y) = \sum_{i=1}^{4} A_i e^{a_i(x-x_i)^2 + b_i(x-x_i)(y-y_i) + c_i(y-y_i)^2}$$

where $A = (-200, -100, -170, 15)$, $a = (-1, -1, -6.5, 0.7)$, $b = (0, 0, 11, 0.6)$, $c = (-10, -10, -6.5, 0.7)$, $x = (1, 0, -0.5, -1)$, $y = (0, 0.5, 1.5, 1)$.

Comments on the algorithms. Besides the stopping condition described in section 5.4.3, we also check the bounds of the definition domain and stop if crossing them. Both proposed methods produce a similar path in case of the Rosenbrock surface, which has only one minimum and no saddle points. Whereas in the case of the Mueller-Brown surface, some stopping criterias apply in the case of TASC. This is due to the gradient extremal of this surface which does not lead to the upper minimum $\mathbf{m}3$ (cf. figure 4 in [4]). So, TASC stops prior to pivoting into the associated valley. This termination is caused according to the rule in section 5.4.3 after discovering the sharp bend immediately after the saddle point. Other methods can help in this special case, e.g. the steepest descent path from the saddle point, potentially in combination with a linesearch correction.

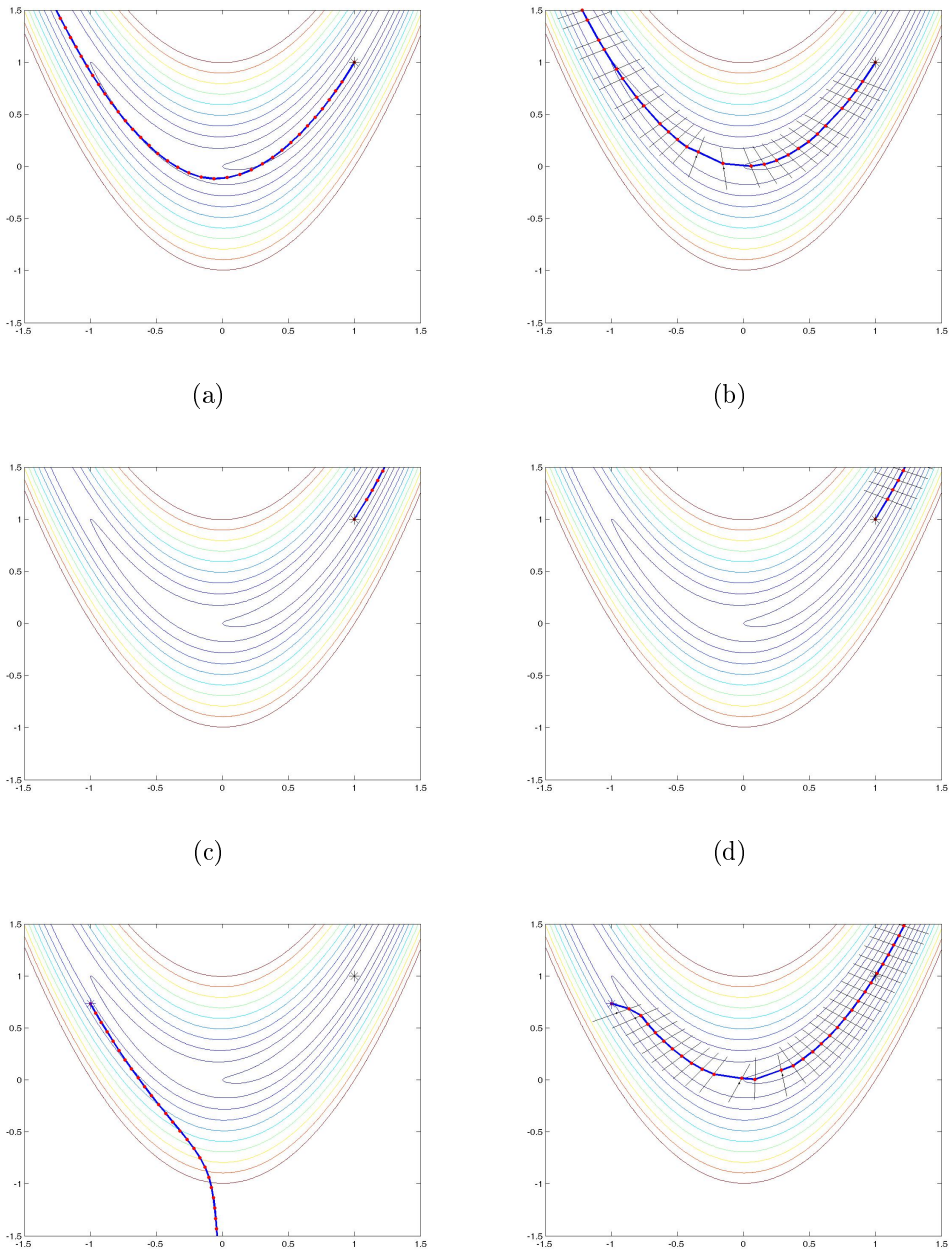

Figure 5.3.: Corrected versus uncorrected trajectories using the EV-step with adaptive step size on the Rosenbrock function. (a)-(d) show trajectories starting at the minimum $(1, 1)$. (a) and (c) shows the uncorrected trajectory while (b) and (d) includes the linesearch correction. Note that between (c) and (d) there is no difference since the valley floor is a linear path. (e) and (f) show trajectories starting at $(-1, .733)$ outside the valley floor. (e) shows the uncorrected trajectory while (f) includes the linesearch correction thus after some iterations it arrives on the valley floor and passes through the minima.

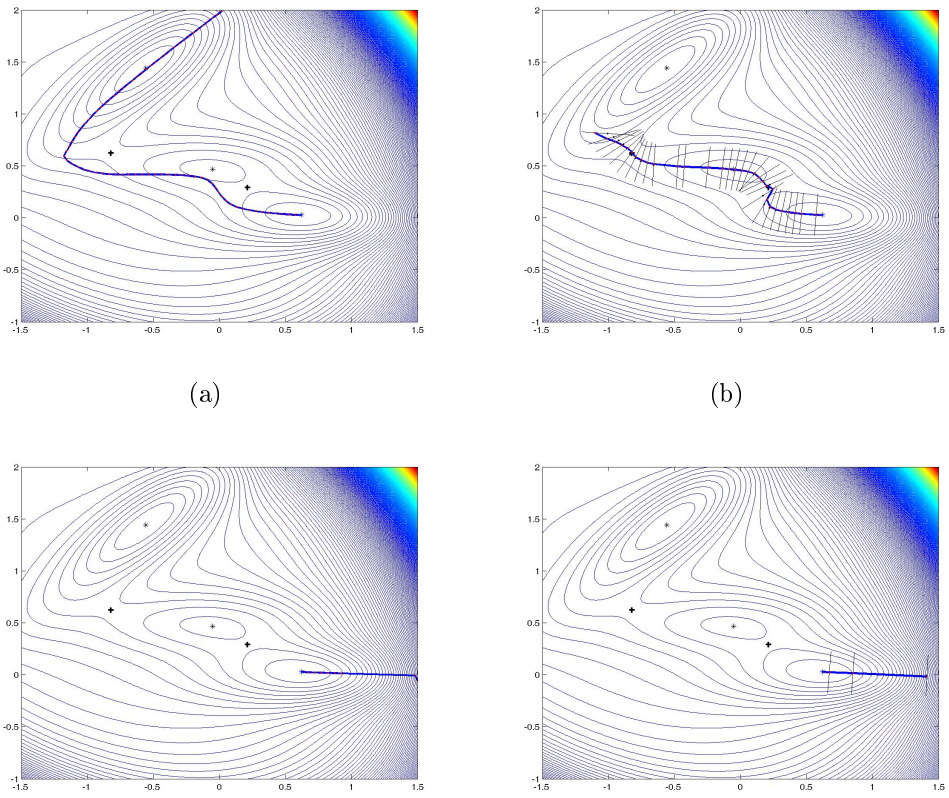

(a) (b)

(c) (d)

Figure 5.4.: Corrected versus uncorrected trajectories using the EV-step on the Mueller-Brown potential. The saddle points are marked with black crosses and the minima with black stars. (a) and (c) show the uncorrected trajectories while (b) and (d) includes the linesearch correction starting from the first minimum $\mathbf{m}_1$. Notice how the step size is large whenever the gradient is the eigenvector corresponding to the smallest eigenvalue like in (c) and (d). Also notice, that between (c) and (d) there is a very small difference since the valley path is linear. However when moving in the other direction of the eigenvector, saddle points and minima are not detected without the linesearch correction as shown for (a) and (b). In this case the valley floor has a more complex structure.

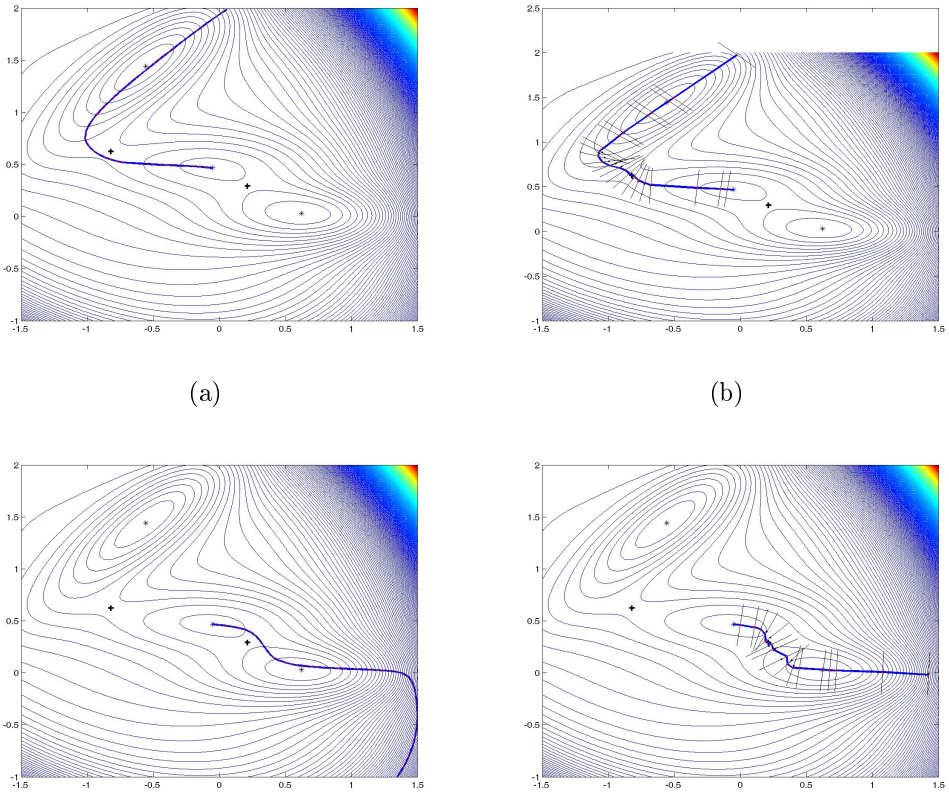

(a) (b)

(c) (d)

Figure 5.5.: Corrected versus uncorrected trajectories using the EV-step on the Mueller-Brown potential. The saddle points are marked with black crosses and the minima with black stars. (a) and (c) show the uncorrected trajectories while (b) and (d) includes the linesearch correction starting from the second minimum $\mathbf{m}_2$. In this case without the linesearch correction none of the stationary points are detected.

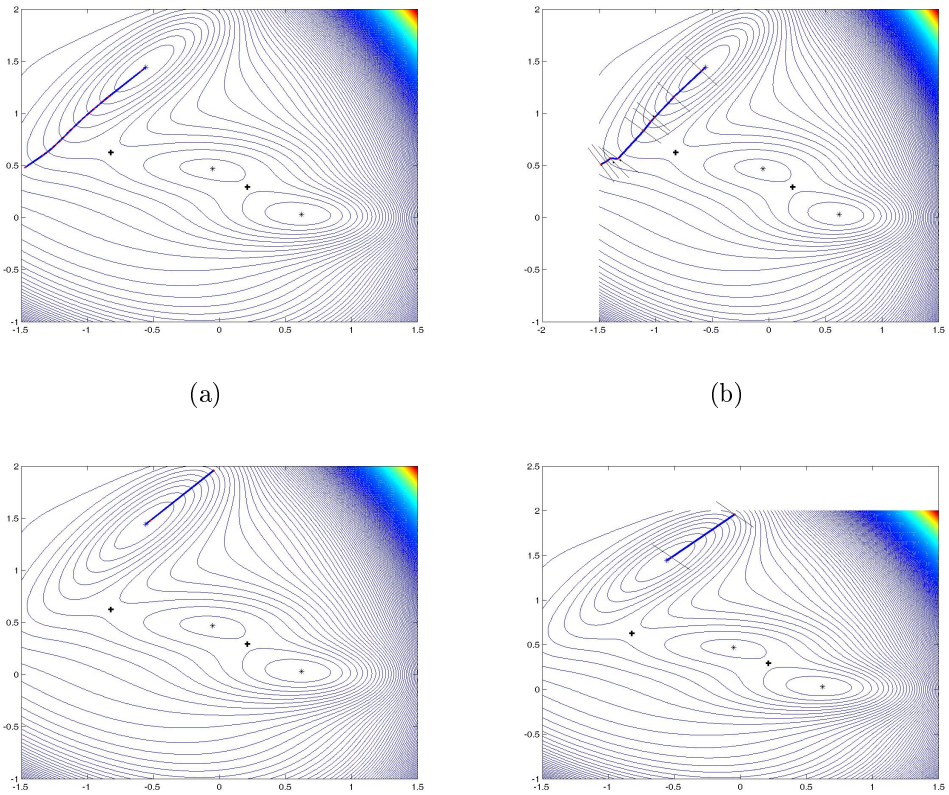

(a) (b)

(c) (d)

Figure 5.6.: Corrected versus uncorrected trajectories using the EV-step on the Mueller-Brown potential. The saddle points are marked with black crosses and the minima with black stars. (a) and (c) show the uncorrected trajectories while (b) and (d) includes the linesearch correction starting from the third minimum $\mathbf{m}_3$. This minimum is embedded into a long linear valley floor and there is almost no difference between the corrected and uncorrected paths. And no other stationary points are detected when starting from this minimum.

5.5.2. Results using TASC

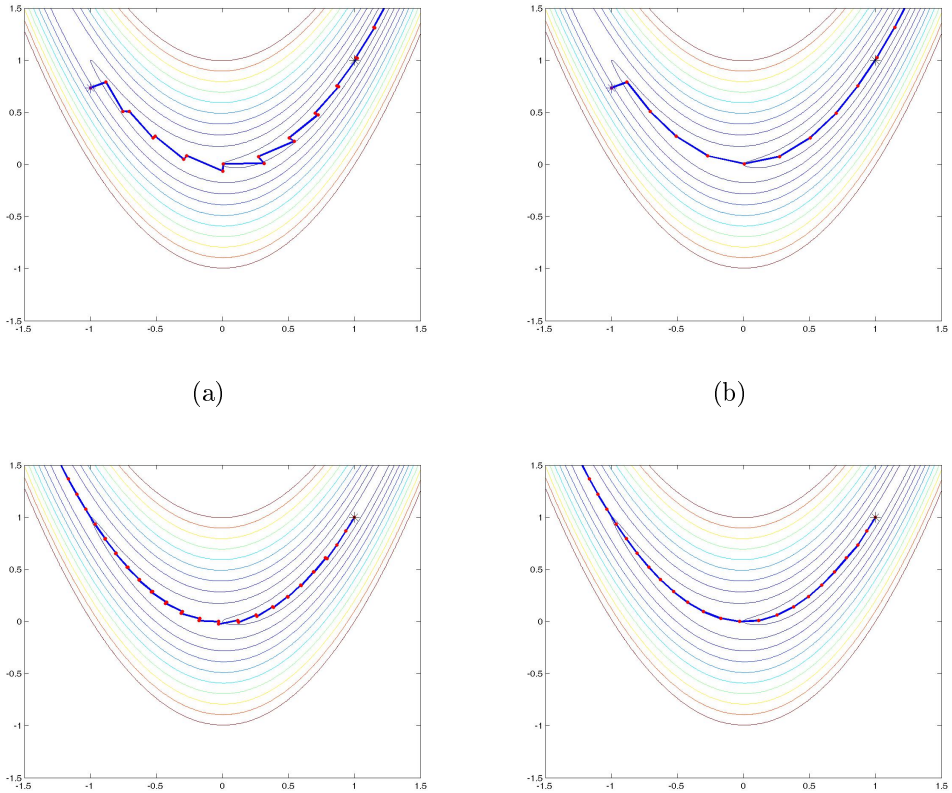

(a) (b)

(c) (d)

Figure 5.7.: TASC algorithm on the Rosenbrock function. (a) and (b) show trajectories starting at $(-1, .733)$ outside the valley floor. (a) and (c) show the predictor and corrector steps while (b) and (d) show only the resulting trajectory. From both starting points TASC ensures that the trajectory stays on the valley floor.

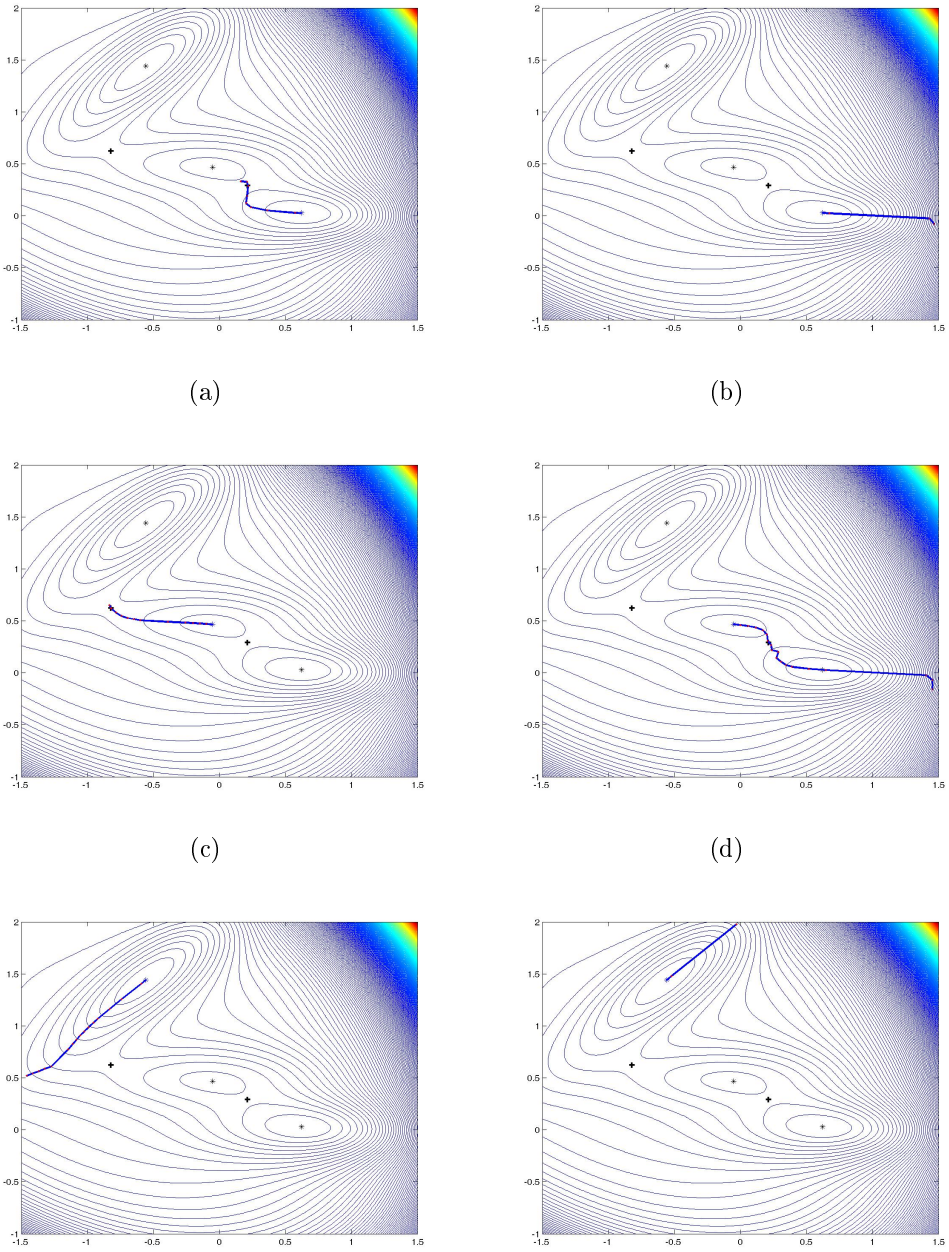

(a) (b)

(c) (d)

(e) (f)

Figure 5.8.: TASC algorithm on the Mueller-Brown potential. The figures show trajectories starting from all three minima along the valley floor. Notice that the algorithm stops in figure (c) after the saddle point since the trajectory performs a sharp bend and we do not allow this for the visualization. See section 5.5.1 for explanations.

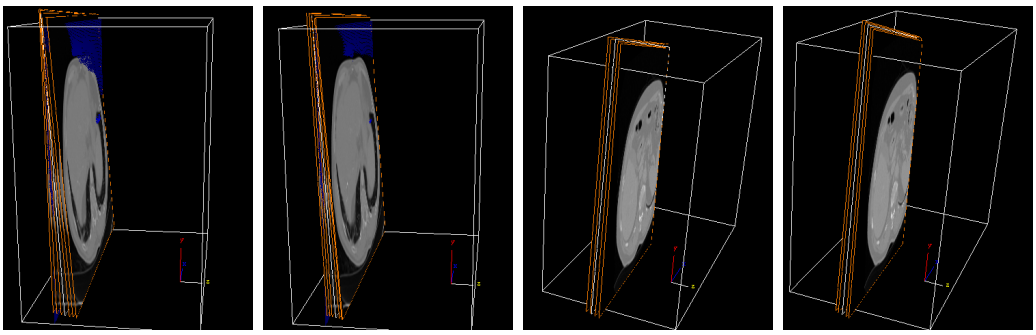

(a) EV-step (b) TASC (c) EV-step (d) TASC

Figure 5.9.: 3D views of estimated slices for synthetic data – results for the TASC algorithm. (a) and (b) show results for synthetic CT-fluoro slices including noise and deformations. (c) and (d) show results on clinical CT-fluoro data.

5.6. Evaluations on synthetic and real CT-fluoro Slices

For quantitative evaluations, we calculate the generated costs, i.e. the accumulated similarity measures as given by the cost function for all generated slices, for both methods. We expect that the optimal algorithm yields a minimal sum. Our aim is not to miss any information of the CT-fluoro slice but in the same time to ensure that the generated slices along the trajectory in the CT-volume have minimum differences from the CT-fluoro slice.

We use data from 7 different patients and 4 CT-fluoro slices for each of them. Additionally, we also use synthetic noisy slices with and without deformation. In total, we evaluate the average costs on 9 data series. For those experiments, we estimate a fixed number of 8 slices using both methods. The first two slices are by design identical. For both methods, the same step size has been employed, such that the conditions are the same. Quantitatively, the TASC method outperformed the EV-step method.

Figure 5.9 shows three-dimensional views of the proposed methods at the positions where the algorithm stopped due to the average motion of voxels criterion. Figures 5.9(a) and 5.9(b) show examples for synthetic CT-fluoro slices containing deformations. The ground-truth surface which is plotted in the volume as a blue surface, is included for the liver voxels into the volume with the stopping criterion. Figures 5.9(c) and 5.9(d) show examples for clinical CT-fluoro slices. Figure 5.10 shows the estimated slices in a 2D view for the example using TASC presented in figure 5.9(d).

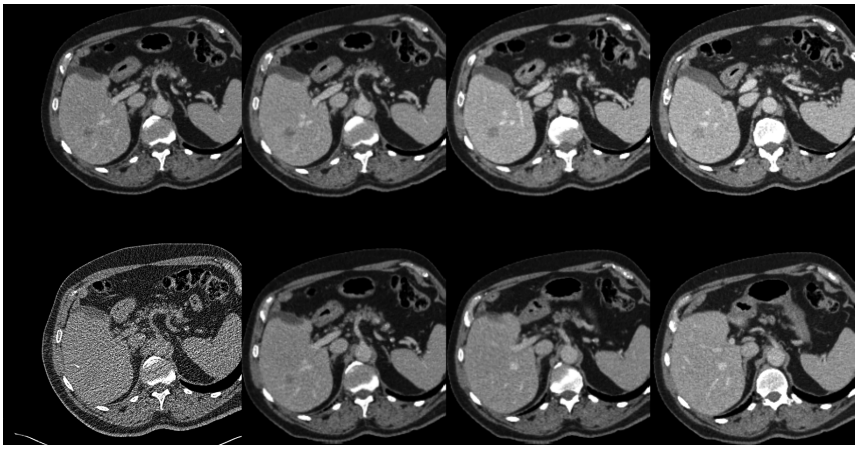

Figure 5.10.: 2D views of estimated slices for clinical data – results for the TASC algorithm. The first image column shows the CT-fluoro slice on the bottom and the estimated minimum at the top. The other images show slices on the valley floor created by the TASC algorithm.

5.7. Discussion

We have presented two methods based on works from computational chemistry and adapted them for visualization along the parameter-space valley floor of the similarity measure. The visualization along this path represents slices in the volume where the uncertainty is highest when estimating the pose in the volume fitting the CT-fluoro slice best. This method has also the advantage of connecting several nearby local minima. Compared to the visualization of the previous chapter 4, this visualization can be easier perceived by users. This is because, basically, a dominant direction along the eigenvector corresponding to the smallest eigenvalue has been identified by analysing the cost surface. As a future step, we will present this visualization to experienced radiologists in order to evaluate it qualitatively.

CHAPTER

SIX

CONCLUSION

Summary. The main objective of this thesis was to visually support the needle insertion task for CT-fluoro guided liver ablation. In order to achieve this goal, we developed novel visualization modes for CT data based on CT-fluoro slices acquired during the intervention. As the visualization modes consisted in displaying a smooth animation sequence, the uncertainty introduced by the deformation was conveyed by providing a set of solutions. The developed algorithms are purely image-based and could be very well integrated into the current workflow. Furthermore, a user interface was provided to interact with the animation and to manually navigate through the resulting subvolume.

The first developed visualization mode relating to the idea that different parts of the liver undergo different levels of motion and deformation, optimized the motion parameters for each part of the CT-fluoro slice to determine the corresponding slice in the CT-volume. Besides this *visualization based on piecewise registration*, we also developed simpler visualization modes for evaluation purposes. We tested the different visualization modes, volume against volume as described in section 3.7, in order to sense the value of such model. The outcome showed that although interventional radiologists are used to axial slices (that we also presented), the final result was in favor of the visualization based on piecewise registration.

In order to use all CT-fluoro information for the registration process, the next two modes modeled the visualization by analyzing the sensitivity of the cost surface for the employed similarity measure in the neighborhood of the globally estimated minimum. Herein, we targeted to visualize those slices in the volume for which the registration process encounters most uncertainty.

The *adaptive visualization based on isosurfaces of slice-to-volume similarity function* recovered out-of-plane motion parameters on isosurfaces. In this approach, we targeted to expand the cost surface sampling uniformly in all out-of-plane directions and combinations of these. A line search was used to provide the sampling points. For that purpose, we developed an adaptive technique for linking the isosurface of the cost function (function space) to the volume (motion parameter space). The adaptivity consisted in correlating the average motion of the voxels within the sub-

volume with liver motions reported in the literature. For this visualization mode, we evaluated the visualization of a single slice versus the recovered subvolume, where the latter proved to be the preferred choice of the interventional radiologists.

The *adaptive visualization based on eigenanalysis of slice-to-volume similarity function* recovered a trajectory along the valley floor of the cost surface. On this trajectory, the cost surface had small variance and, thus, high uncertainty in estimating a solution in the CT-volume. Furthermore, this trajectory had also the property of connecting nearby local minima by passing through saddle points. We evaluated two such methods on analytical surfaces, on synthetic slices including deformation, and on real CT-fluoro slices. This concept proved to yield a visualization which can be easier perceived by users.

6.1. Discussion and Future Work

Unified visualization evaluation. The last two of the three approaches presented in this work feature the highest robustness. The second approach, presented in chapter 4, featured the highest accuracy in visualizing the fuzziness around the minimum, as it expands a visualization in all out-of-plane directions around the estimated minimum, while weighting all directions in the same way. On the other hand, the last visualization mode presented in chapter 5, seems to be the best perceivable of all since the visualization follows a trajectory[1] identified by all motion parameters but favoring those imposing weaker constraints. However, its superior perceivability is still to be confirmed in a comparative evaluation of the modes by interventional radiologists.

Further clinical applications. In this work, we focused on the liver ablation procedure. However, the developed visualization methods can be transferred to other interventional applications where a solution set can aid the operation. Ablations performed on other organs like lung or kidney can be considered. Biopsies feature the same workflow as ablations until the target lesion has been reached. The developed registration and visualization tools are also suitable for different modalities other than CT/CT-fluoro, used for the pre-interventional scan and the intervention. In this case, the employed similarity measure has to adapted for the application.

6.1.1. Extensions for new Scanner Protocols

A recently introduced software for CT scanners provides the feature of saving three CT-fluoro slices at the same time. This protocol adds more information in the z direction and makes this application less ill-posed. The registration methods developed can be naturally extended from a slice-to-volume registration to a subvolume-to-volume registration. The additional information will certainly improve the regis-

[1] The trajectory path is along the positive and negative directions of the eigenvector corresponding to the smallest eigenvalue

tration step and also the estimation of the subvolume in the pre-interventional scan. The visualization along a trajectory which imposes most uncertainty is very suitable also for this protocol.

Enhanced visualization. Future work can investigate the position of the needle tip relative to the target lesion in the volume. The predicted position could then be displayed in the 3D CT-volume. Recent works [59] focus on an optimal trajectory planning which can be incorporated together with the segmented lesions into a 3D view, and displayed during the intervention. In this case an uncertainty visualization of the trajectory path in a similar way to [110] could be useful.

Evaluation of clinical data. Due to the lack of a gold standard algorithm for this application or gold standard clinical data, the only available option for evaluating the clinical data regarding registration and visualization results has been to rely on visual assessment. The criteria that can help for the assessment of registration results have been gained during several discussions with interventional radiologists (see 1.1.1). However, this method is only qualitative and subjective. Providing gold standard data for this application is a necessary step toward clinical use.

Deformable registration. Supplementary to a rigid registration, a deformable registration can be used to locally refine and update the result. The approach to be used should be fast and mainly intensity based[2]. A promising class of functions that could provide the requirements are the Radial Basis Functions (RBF's). The displacement field is parametrically defined at discrete control points $\mathbf{x}_i$:

$$\mathbf{v}(\mathbf{x}) = \sum_{i=1}^{N} \mathbf{c}_i \Phi(\mathbf{x} - \mathbf{x}_i).$$

The coefficients $\mathbf{c}_i$ act like forces at the control points. In [98] RBF's have been used in an intensity based approach where regions of mismatch are automatically identified and a topology preserving constraint is also derived. To move toward a more physically intensity based parametric approach, in [86] the authors suggest to use a Gaussian shaped force for which the corresponding analytical solution in an elastic medium is known. In this approach both the forces and the irregular placed control points are optimized during the alignment.

Figure 6.1 shows the deformation on a grid when applying a Gaussian RBF in one point. A Gaussian RBF reads

$$\Phi(\mathbf{x}) = \exp(-\frac{\|\mathbf{x}\|_2^2}{2\sigma^2}),\ with\ \mathbf{x} \in \mathbb{R}^3$$

In order to show the effect of the deformation along each axis' direction separately, the coefficients in the non-considered dimensions are set to zero.

[2]Since vessel features cannot be used for the registration in this application as we already mentioned in section 3.2.1

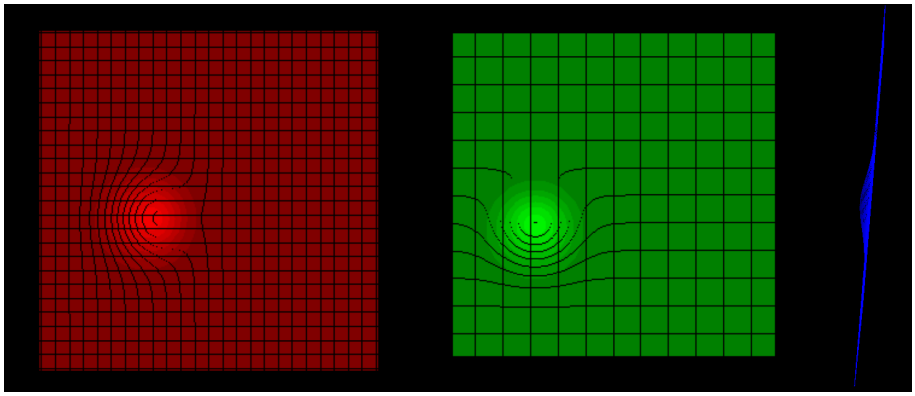

Figure 6.1.: Left: Gaussian RBF along x-direction, middle: Gaussian RBF along y-direction, right: Gaussian RBF along z-direction (out-of-plane)

We apply an intensity based slice-to-volume deformable registration defined by Gaussian RBF's on synthetic medical data, for which the GT is known from an elastic deformation. The optimization of the force coefficients $\mathbf{c}_i$ is performed with a gradient descent optimization. Initial experiments show that contours are very well recovered, however the lesion is not matching well. In this case, additional information along the z-axis will probably improve this result. It is also recommendable to use data from patients with HCC since this lesion is visible also in the CT-fluoro slices making a validation easier. This approach can be further extended to the one proposed by Pekar et. al [86] to reach a more physically based model.

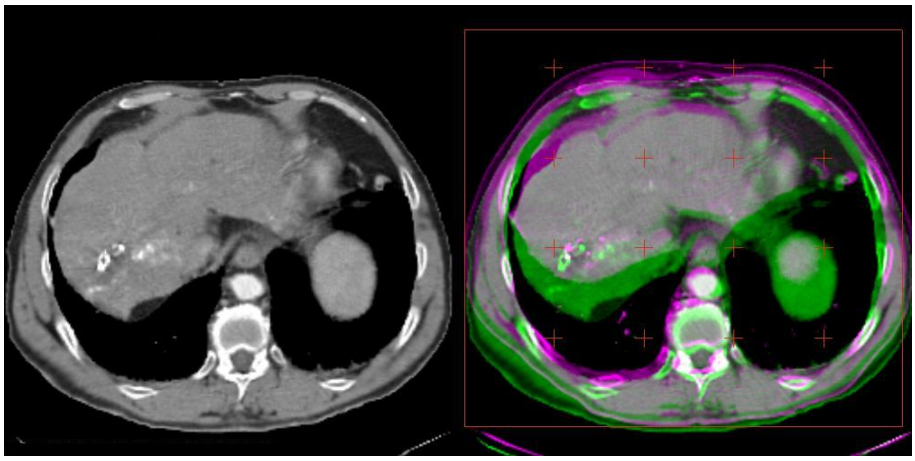

(a) Init

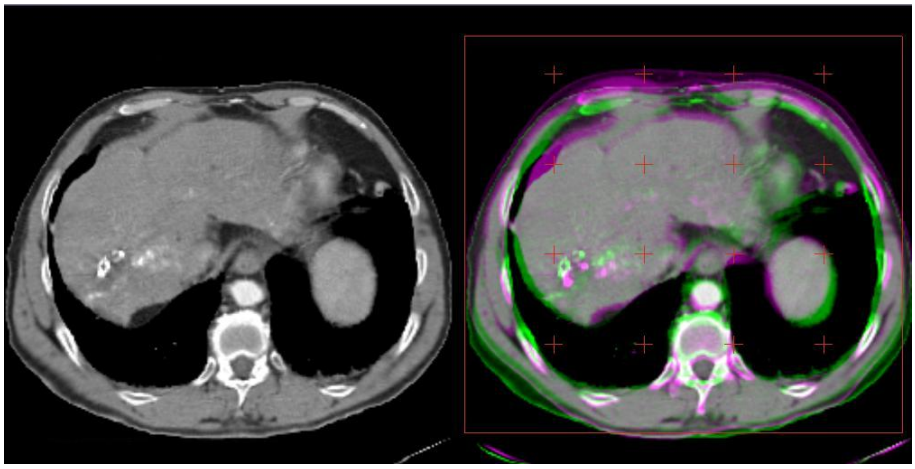

(b) After slice-to-volume deformable registration

Figure 6.2.: Slice-to-volume deformable example. (a) shows on the left a synthetic CT slice where the GT is known. On the right, the image in the CT-volume is shown at the axial position where the synthetic CT slice was extracted from the deformed volume. For this large deformation, also a large grid of the control points is applied to cope with it. Note that the predicted lesion position in the volume is not matching with the 2D CT slice.

APPENDIX

A

OPTIMIZATION

The material of this appendix is taken from [36], [81], [68], [38], [3]. Optimization algorithms based on descent directions are presented below. For simplicity only the non-robust case for the SSD is presented.
Consider the function $F(\mathbf{x}) : \mathbb{R}^m \mapsto \mathbb{R}$ being the sum of squares of nonlinear functions and $\mathbf{x}^*$ satisfying:

$$\mathbf{x}^* = argmin_{\mathbf{x}} \left\{ F(\mathbf{x}) = \frac{1}{2} \sum_{i=1}^{m} f_i(x)^2 = \frac{1}{2} \|f(x)\|_2^2 \right\} \tag{A.1}$$

Due to the non-linearity, the solution $\mathbf{x}^*$ is iteratively estimated: from a starting point $\mathbf{x}_0$, $\mathbf{x}_k$ is computed in a descent direction such that $F(\mathbf{x}_k) < F(\mathbf{x}_{k+1})$ is satisfied. This iterative process is based on a local linear or quadratic model of the objective function. Depending on the employed model, there are several optimization techniques each of them having different convergence properties (see section A.1). Let g_i be the gradient and $H_{i,j}$ be the Hessian Matrix of F with:

$$\mathbf{g} = g_i = \frac{\partial F}{\partial x_i} = \mathbf{J}_f(x)^T f(x) \quad with \quad \mathbf{J}_f(x) = \frac{\partial f_i}{\partial x_i} \tag{A.2}$$

$$\mathbf{H} = H_{i,j} = \frac{\partial^2 F}{\partial x_i \partial x_j} = \mathbf{J}_f(x)^T \mathbf{J}_f(x) + \sum_{i=1}^{m} f_i(x) f_i''(x) \tag{A.3}$$

The generic algorithm for the iterative "step-length-based" descent methods is:

k := 0, $\mathbf{x} := \mathbf{x}_0$
while $\|g_i\| < \epsilon 1$ and $\|\alpha \mathbf{h}\|$ and $k \leq k_{max}$ **do**
  Find a descent direction $\mathbf{h}$
  $\mathbf{x} := \mathbf{x} + \alpha \mathbf{h}, \alpha > 0$
  k := k + 1
end while

Considering a variation of F along the half line starting from $\mathbf{x}$ with direction $\mathbf{h}$, the Taylor expansion is given by:

$$F(\mathbf{x} + \alpha\mathbf{h}) \simeq F(\mathbf{x}) + \alpha\mathbf{h}^T\mathbf{g} \tag{A.4}$$

for α sufficiently small. Thus, in order that h is a descent direction, it has to satisfy $\mathbf{h}^T\mathbf{g} < 0$. If no such direction exist then $\mathbf{g} = \mathbf{0}$ (cf. [36], section 3.2.2). Otherwise α has to be determined in order to get a decrease in the objective function F. This is called *line search*

$$\alpha^* = argmin_{\alpha>0}\{F(\mathbf{x} + \alpha\mathbf{h})\} \tag{A.5}$$

A.1. Convergence

linear convergence	$\|x_{k+1} - x^*\| < \epsilon\|x_k - x^*\|$	
superlinear convergence	$\|x_{k+1} - x^*\| < \epsilon_k\|x_k - x^*\|$	with $\epsilon_k \to 0$
quadratic convergence	$\|x_{k+1} - x^*\| < \epsilon\|x_k - x^*\|^2$	

A.2. Steepest descent

The relative gain of F when moving in a descent direction as in eq.A.4 satisfies:

$$\lim_{\alpha\to 0} = \frac{F(\mathbf{x}) - F(\mathbf{x} + \alpha\mathbf{h})}{\alpha\|\mathbf{h}\|} = -\frac{\mathbf{h}^T\mathbf{g}}{\|\mathbf{h}\|} = -\|\mathbf{g}\|\cos\theta, \tag{A.6}$$

where θ represents the angle between the vectors $\mathbf{g}$ and $\mathbf{h}$. The biggest gain is achieved when $\theta = \pi$. The resulting direction is the one of negative gradient and it is called the *steepest-descent* direction:

$$\mathbf{h} = -\mathbf{g} \tag{A.7}$$

The step length α is then computed by a line search, e.g. with the Armijo backtracking line-search condition. This method is very slow, it converges linearly.

A.3. Newton method

A quadratic Taylor expansion of F about x is given by:

$$F(\mathbf{x} + \mathbf{h}) \simeq L(\mathbf{h}) = F(\mathbf{x}) + \mathbf{g}\mathbf{h} + \frac{1}{2}\mathbf{h}^T\mathbf{H}(\mathbf{x})\mathbf{h} \tag{A.8}$$

The unconstrained minimum of $L(\mathbf{h})$ solving for the step length is:

$$L'(\mathbf{h}) = \mathbf{g} + \mathbf{h}\mathbf{H}(\mathbf{x}) = \mathbf{0} \tag{A.9}$$

$$\Leftrightarrow \mathbf{h}\mathbf{H}(\mathbf{x}) = -\mathbf{g} \tag{A.10}$$

This method has final quadratic convergence but it is not robust. Far away from the minimum, there is no guarantee that the objective function is still strictly convex and thus the Hessian matrix is not any more positive definite.

A.4. Gauss-Newton method

The GaussNewton method is based on a linear approximation to the components of f_i about x. The assumption is that near the minimum the residuals f_i tend towards zero and thus the second part of the Hessian (see eq. A.3), too. In this case the Gauss-Newton optimization has also quadratic convergence, since $\mathbf{H} = \mathbf{L}''(h) = \mathbf{J}^T(\mathbf{x})\mathbf{J}(\mathbf{x})$

$$f(\mathbf{x}+\mathbf{h}) \simeq l(\mathbf{h}) = f(\mathbf{x}) + \mathbf{J}_f(x)\mathbf{h} \tag{A.11}$$

$$F(\mathbf{x}+\mathbf{h}) \simeq L(\mathbf{h}) = \frac{1}{2}l(\mathbf{h})^T l(\mathbf{h}) \tag{A.12}$$

$$= \frac{1}{2}f^T(\mathbf{x})f(\mathbf{x}) + h^T\mathbf{J}^T(\mathbf{x})f(\mathbf{x}) + \frac{1}{2}\mathbf{h}^T\mathbf{J}^T(\mathbf{x})\mathbf{J}(\mathbf{x})h \tag{A.13}$$

$$= F(\mathbf{x}) + h^T\mathbf{J}^T(\mathbf{x})f(\mathbf{x}) + \frac{1}{2}\mathbf{h}^T\mathbf{J}^T(\mathbf{x})\mathbf{J}(\mathbf{x})\mathbf{h} \tag{A.14}$$

The unconstrained minimum of $L(h)$ solving for the step length is:

$$L'(\mathbf{h}) = \mathbf{J}^T(\mathbf{x})f(\mathbf{x}) + \mathbf{J}^T(\mathbf{x})\mathbf{J}(\mathbf{x})\mathbf{h} = \mathbf{0} \tag{A.15}$$

$$\Leftrightarrow \mathbf{J}^T(\mathbf{x})\mathbf{J}(\mathbf{x})\mathbf{h} = -\mathbf{J}^T(\mathbf{x})f(\mathbf{x}) \tag{A.16}$$

the matrix $\mathbf{L}''(h) = \mathbf{J}^T(\mathbf{x})\mathbf{J}(\mathbf{x})$ is symmetric and positive semidefinite. If $\mathbf{J}(\mathbf{x})$ has full rank (i.e. the columns are linearly independent) then it is also positive definite. In this case the descent direction $\mathbf{h}^T\mathbf{g} < 0$ is satisfied. If the functions $\{f_i\}$ have small curvatures $\{f_i''\}$ or their absolute values are small, then a superlinear convergence is expected, but in general the final convergence is linear.

A.5. Trust regions and damped methods

These methods build a model L of the behaviour of F in the neighbourhood of the current iterate $\mathbf{x}$ and accept the step $\mathbf{h}$, only if the model is a good approximation of the original function. Usually a quadratic model is employed by a second order Taylor approximation:

$$F(\mathbf{x}+\mathbf{h}) \simeq L(\mathbf{h}) = F(\mathbf{x}) + \mathbf{g}\mathbf{h} + \frac{1}{2}\mathbf{h}^T\mathbf{H}(\mathbf{x})\mathbf{h} \tag{A.17}$$

In order to check if the model is adequate, the gain ration between the model and the true function is computed:

$$\rho = \frac{F(\mathbf{x}) - F(\mathbf{x}+\mathbf{h})}{L(\mathbf{0}) - \mathbf{L}(\mathbf{h})} \tag{A.18}$$

A.5.1. Trust region methods

In this case the step is computed by the constrained optimization subproblem:

$$\mathbf{h} = \mathbf{h}_{tr} = argmin_{\|\mathbf{h}\|<\Delta}\{L(\mathbf{h})\} \tag{A.19}$$

A basic algorithm for the trust region problem can be formulated as following:

k := 0, $\Delta := \Delta_0$, $\eta_v = 0.9$, $\eta_s = 0.1$, $\gamma_{inc} = 2.0$, $\gamma_{dec} = 0.5$
while not converged **do**
  Built a model $L(\mathbf{h})$ of $F(\mathbf{x} + \mathbf{h})$
  "Solve" the trust-region subproblem to find $\mathbf{h}_k$ for which $L(\mathbf{h}) < F(\mathbf{x}_k)$ and $\|\mathbf{h}\| < \Delta$ and define $\rho_k = \frac{F(\mathbf{x}_k) - F(\mathbf{x}_k + \mathbf{h}_k)}{L(\mathbf{0}) - \mathbf{L}(\mathbf{h_k})}$
  if $\rho_k \geq \eta_v$ [very successful] **then**
    set $\mathbf{x}_{k+1} = \mathbf{x}_k + \mathbf{h}_k$ and $\Delta_{k+1} = \gamma_{inc}\Delta_k$
  else if $\rho_k \geq \eta_s$ [successful] **then**
    set $\mathbf{x}_{k+1} = \mathbf{x}_k + \mathbf{h}_k$ and $\Delta_{k+1} = \Delta_k$
  else {unsuccessful}
    set $\mathbf{x}_{k+1} = \mathbf{x}_k$ and $\Delta_{k+1} = \gamma_{dec}\Delta_k$
  end if
  k := k + 1
end while

A.5.1.1. Trust region subproblem

If $\mathbf{H}$ is positive definite and it lies in the interior of Δ, then the solution to eq. A.17 is the solution of eq. A.10, i.e. the Newton step. If the solution lies outside the trust region, the solution lies on the boundary of the trust region. Special care has to be paid when $\mathbf{H}$ is indefinite or positive semi-definite and singular, in these cases the solution is not unique. This is denoted as the "hard case" (for the handling please see [22]). For those cases except of the hard case the solution of the subproblem satisfies (for a proof see for instance [3], section 4.1):

$$\begin{aligned} (\mathbf{H} + \lambda\mathbf{I})\mathbf{h} &= -\mathbf{g} \\ \|\mathbf{h}\| &= \Delta \end{aligned} \tag{A.20}$$

This is a non-linear system where λ, the regularization factor (since it pushes the system to be positive definite), and the step $\mathbf{h}$ are the unknowns. For solving this non-linear system it is convenient to decompose $\mathbf{H}$ into its spectral decomposition and also to consider $\|\mathbf{h}\|^2 = \Delta^2$ rather than the second part of eq. A.20.

$$\mathbf{H} = \mathbf{U}^T\Lambda\mathbf{U} \tag{A.21}$$

here U is a matrix of (orthonormal) eigenvectors while the diagonal matrix Λ is made up of eigenvalues $\lambda_1 < \lambda_2 < \lambda_3 < ... < \lambda_m$. Since $\mathbf{H} + \lambda\mathbf{I}$ has to be positive semi-definite, and so the solution (s, λ) to eq. A.20 has to provide a λ which is greater than the smallest eigenvalue λ_1. The first part of eq. A.20 can be transformed to write $\mathbf{h}$ explicitly in terms of λ:

$$\mathbf{h}(\lambda) = (\mathbf{H} + \lambda\mathbf{I})^{-1}\mathbf{g} = -\mathbf{U}^T(\Lambda + \lambda\mathbf{I})^{-1}\mathbf{U}\mathbf{g} \tag{A.22}$$

Now substituting eq. A.22 into the second part of eq. A.20:

$$\psi(\lambda) = \|\mathbf{h}(\lambda)\|^2 = \|\mathbf{U}^T(\Lambda + \lambda\mathbf{I})^{-1}\mathbf{U}\mathbf{g}\|^2 = \sum_{i=1}^{m} \frac{\gamma_i^2}{(\lambda_i + \lambda)^2} = \Delta^2 \tag{A.23}$$

where $\gamma_i = \langle e_i, \mathbf{U}\mathbf{g}\rangle = \left\langle \mathbf{U}^T e_i, \mathbf{g}\right\rangle$ is the component of $\mathbf{g}$ in the direction of the ith eigenvector. Thus to solve the trust-region subproblem is to find a particular root of a univariate nonlinear equation. Since this equation has poles at its eigenvalues, it is more convenient to solve for an equivalent equation, the *secular equation* which has no poles and the Newton method can be applied for the root finding:

$$\phi(\lambda) = \frac{1}{\|\mathbf{h}(\lambda)\|} - \frac{1}{\Delta} = 0 \tag{A.24}$$

The Newton secant method approaches iteratively the root with the correction factor $-\phi(\lambda)/\phi'(\lambda)$.

$$\phi(\lambda) = \frac{1}{(\langle \mathbf{h}(\lambda), \mathbf{h}(\lambda)\rangle)^{.5}} - \frac{1}{\Delta} \tag{A.25}$$

$$\phi'(\lambda) = -\frac{\langle \mathbf{h}(\lambda), \nabla_\lambda \mathbf{h}(\lambda)\rangle}{(\langle \mathbf{h}(\lambda), \mathbf{h}(\lambda)\rangle)^{1.5}} \tag{A.26}$$

In addition by deriving the first part of eq. A.20:

$$(\mathbf{H} + \lambda\mathbf{I})\nabla_\lambda \mathbf{h}(\lambda) + \mathbf{h}(\lambda) = \mathbf{0} \tag{A.27}$$

Now the numerator of eq. A.26 becomes using a Cholesky factorization of $(\mathbf{H}+\lambda\mathbf{I}) = \mathbf{L}(\lambda)\mathbf{L}(\lambda)^T$:

$$\begin{aligned}\langle \mathbf{h}(\lambda), \nabla_\lambda \mathbf{h}(\lambda)\rangle &= -\left\langle \mathbf{h}(\lambda), (\mathbf{H} + \lambda\mathbf{I})^{-1}\mathbf{h}(\lambda)\right\rangle = -\left\langle \mathbf{h}(\lambda), \mathbf{L}(\lambda)^{-T}\mathbf{L}(\lambda)^{-1}\mathbf{h}(\lambda)\right\rangle \\ &= -\left\langle \mathbf{L}(\lambda)^{-1}\mathbf{h}(\lambda), \mathbf{L}(\lambda)^{-1}\mathbf{h}(\lambda)\right\rangle = \|\mathbf{w}\|^2 \end{aligned} \tag{A.28}$$

The Newton method for the secular equation is summarized as following:
$\lambda > \lambda_1$ and $\Delta > 0$
while not converged **do**
  Factorize $(\mathbf{H} + \lambda\mathbf{I}) = \mathbf{L}(\lambda)\mathbf{L}(\lambda)^T$
  Solve $\mathbf{L}(\lambda)\mathbf{L}(\lambda)^T\mathbf{h} = -\mathbf{g}$
  Solve $\mathbf{L}(\lambda)\mathbf{w} = \mathbf{h}$
  $\lambda \leftarrow \lambda + \left(\frac{\|\mathbf{h}\|-\Delta}{\Delta}\right)\left(\frac{\|\mathbf{h}\|^2}{\|\mathbf{w}\|^2}\right)$
end while

This method is not suitable for large scale problems where the Cholesky factorization is expensive. Approximate solutions are e.g.: the conjugate-gradient method [38], Powell's Dog Leg method [68].

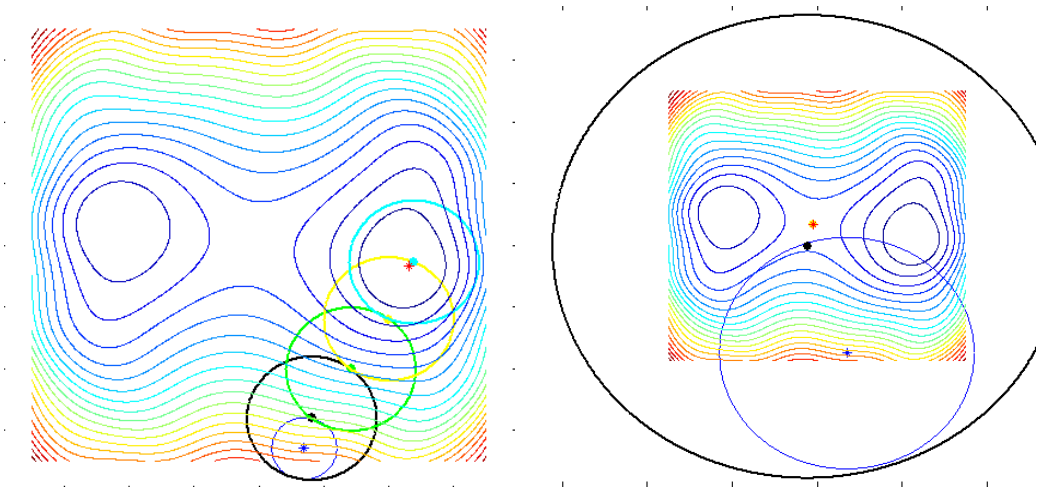

(a) TR with radius .2 (b) TR with radius .5

Figure A.1.: TR examples for a function with two minima and one saddle point. The starting point is marked with a blue star while the end point with a red star. The TR radius is adapted according to how well the model is approximating the function. For visibility only the radii of the first four iterations are shown. The same color encodes the radius corresponding to the actual iteration position. In (a) the algorithm converges to the one minimum while in (b) it converges to the saddle point. This happens due to the fact that the TR radius is in (b) bigger than the first Newton step, and thus the step is accepted.

A.5.2. Damped methods

In a damped method the step update is computed as:

$$\mathbf{h} = argmin\{\mathbf{L}(\mathbf{h}) + \frac{1}{2}\mu\mathbf{h}^T\mathbf{h}\} \tag{A.29}$$

where the damping parameter $\mu \leq 0$ and the term $\frac{1}{2}\mathbf{h}^T\mathbf{h} = \frac{1}{2}\|\mathbf{h}\|^2$ is a regularization term for penalizing large steps. A small factor gain ρ (eq. A.18) indicates that the model does not predict well the true function therefore the damping parameter should be increased, in this way increasing the penalty on large steps. A big factor indicates that the the model is a good approximation and therefore the damping parameter can be decreased.
The step update in this method is then the stationary point of the function as defined in A.29 and can be computed by:

$$\begin{aligned} &\mathbf{L}'(\mathbf{h}) + \mu\mathbf{h} = \mathbf{0} \\ \Leftrightarrow\ &(\mathbf{H}(\mathbf{x}) + \mu\mathbf{I})\mathbf{h} = -\mathbf{g} \end{aligned} \tag{A.30}$$

where $L(\mathbf{h})$ is defined in eq. A.17. If μ is sufficiently large, the matrix $H(\mathbf{x}) + \mu I$ is positive definite and the step is descent direction of L.

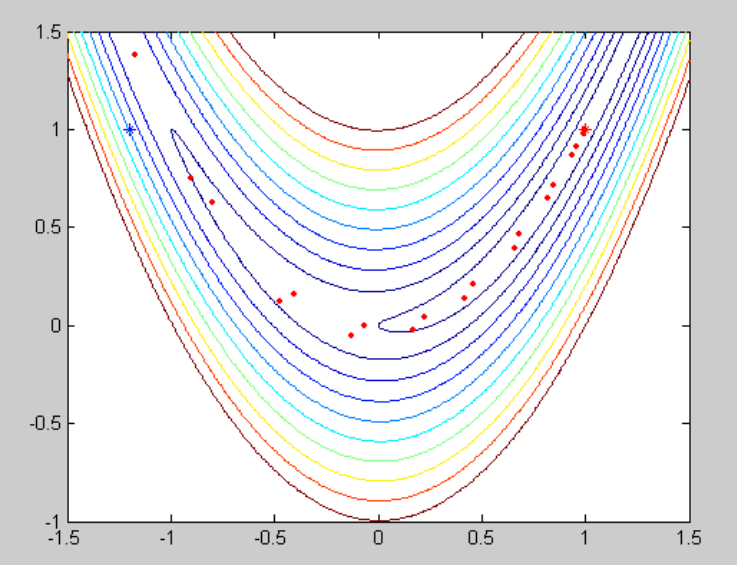

(a) Damped Newton

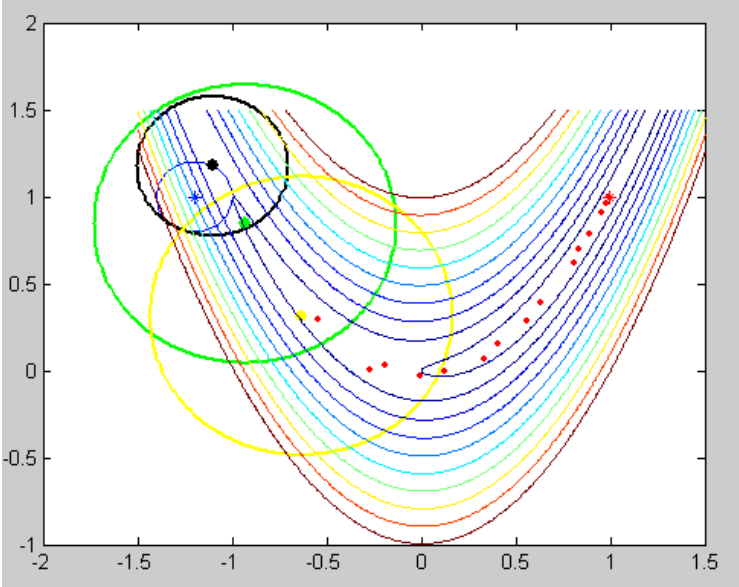

(b) Trust region

Figure A.2.: Rosenbrock function. Starting point is marked with a blue star, while the end point is marked with a red star. Both algorithms are converged to the minimum. In (a) the damping parameter is adapted accordingly, thus robustizing the Newton method. Alternatively, one can use the steepest descent with a line search when the Newton step fails. (b) The Trust region radius is set to .2 in the beginning. The TR radius is adapted according to how well the model is approximating the function. For visibility only the radii of the first three iterations are shown. The same color encodes the radius corresponding to the actual iteration position.

A.6. Levenberg-Marquardt

This method is a *damped Gauss-Newton method*. The modification of eq. A.16 is done by adding the penalty term as described in A.5.2, thus the step update computation resulting in:

$$(\mathbf{J}^T(\mathbf{x})\mathbf{J}(\mathbf{x}) + \mu\mathbf{I})\mathbf{h} = -\mathbf{J}^T(\mathbf{x})f(\mathbf{x}) \tag{A.31}$$

The damping parameter influences both the direction and the size of the step, and this leads to a method without a specific line search. The direction is a descent direction for all $\mu > 0$ since the coefficient matrix is positive definite. If $\mu = 0$ the step is a Gauss-Newton step. If μ is large then the step is a short step in the steepest descent direction $\mathbf{h} = -\frac{1}{\mu}\mathbf{g}$. The starting value of μ should be related to the coefficients of the matrix $\mathbf{J}^T(\mathbf{x})\mathbf{J}(\mathbf{x})$ by taking the maximum of them for instance. The updating is controlled by the gain factor ρ as in eq. A.18 where L is now a linear model as in A.11. A large value of ρ indicates that $L(\mathbf{h})$ is a good approximation to $F(\mathbf{x}+\mathbf{h})$, and μ can be decreased so that the next Levenberg-Marquardt step is closer to the Gauss-Newton step. If ρ is small (maybe even negative), then $L(\mathbf{h})$ is a poor approximation, and μ should be increased with the twofold aim of getting closer to the steepest descent direction and reducing the step length. Strategies for increasing/decreasing μ are described e.g. in [81]

A.7. Sequential Quadratic Optimization

This method is again an iterative method where at each iteration a general quadratic optimization is solved. A quadratic optimization problem has a quadratic cost function and all the constraints are linear. In this section only equality constraints are considered:

$$\begin{aligned} \mathbf{x}^* &= argmin_{x\in P} f(\mathbf{x}) \\ P &= \{\mathbf{x} \in \mathbb{R}^n | \mathbf{c}(\mathbf{x}) = \mathbf{0}\} \end{aligned} \tag{A.32}$$

where $\mathbf{c} : \mathbb{R}^n \mapsto \mathbb{R}^r$ and whose ith component is the ith constraint function c_i. The corresponding Lagrange's function is:

$$L(\mathbf{x}, \boldsymbol{\lambda}) = f(\mathbf{x}) - \boldsymbol{\lambda}^T\mathbf{c}(\mathbf{x}), \tag{A.33}$$

with the gradient

$$\mathbf{L}'(\mathbf{x}, \boldsymbol{\lambda}) = \begin{bmatrix} \mathbf{L}'_x(\mathbf{x}, \boldsymbol{\lambda}) \\ \mathbf{L}'_\lambda(\mathbf{x}, \boldsymbol{\lambda}) \end{bmatrix} = \begin{bmatrix} f'(\mathbf{x}) - \mathbf{J}_c^T\boldsymbol{\lambda}) \\ -\mathbf{c}(\mathbf{x}) \end{bmatrix}, \tag{A.34}$$

where $\mathbf{J}_c$ is the *Jacobian matrix* of the constraint function $\mathbf{c}$:

$$(\mathbf{J}_c)_{ij} = \frac{\partial c_i}{\partial x_j}(\mathbf{x}) \Leftrightarrow \mathbf{J}_c = [c'_1(\mathbf{x})...c'_r(\mathbf{x})]^T. \tag{A.35}$$

Now eq. A.32 can be solved by finding the pair $(\mathbf{x}^*, \boldsymbol{\lambda})$ such that the non-linear system of equations in eq. A.34 is equal to $\mathbf{0}$. By using the Newton-Raphson's method(see also section A.3) to estimate the step $(\mathbf{h}, \boldsymbol{\eta}$ added to the current iterate $(\mathbf{x}, \boldsymbol{\lambda})$ the update equation looks like:

$$\mathbf{L}''(\mathbf{x}, \boldsymbol{\lambda}) \begin{bmatrix} \mathbf{h} \\ \boldsymbol{\eta} \end{bmatrix} = -\mathbf{L}'(\mathbf{x}, \boldsymbol{\lambda}) \tag{A.36}$$

where $\mathbf{L}''$ is the Hessian of the Lagrange function:

$$\mathbf{L}''(\mathbf{x}, \boldsymbol{\lambda}) = \begin{bmatrix} \mathbf{L}''_{xx} & \mathbf{L}''_{x\lambda} \\ \mathbf{L}''_{\lambda x} & \mathbf{L}''_{\lambda\lambda}) \end{bmatrix} = \begin{bmatrix} \mathbf{W} & -\mathbf{J}_c^T \\ -\mathbf{J}_c^T & \mathbf{0} \end{bmatrix}, \tag{A.37}$$

with $\mathbf{W} = \mathbf{L}''_{xx} = f''(\mathbf{x}) - \sum_{i=1}^{r} \lambda_i \mathbf{c}''_i(\mathbf{x})$.
One Newton-Raphson step is:

$$\begin{bmatrix} \mathbf{W} & -\mathbf{J}_c^T \\ -\mathbf{J}_c^T & \mathbf{0} \end{bmatrix} \begin{bmatrix} \mathbf{h} \\ \boldsymbol{\eta} \end{bmatrix} = - \begin{bmatrix} f'(\mathbf{x}) - \mathbf{J}_c^T \boldsymbol{\lambda}) \\ -\mathbf{c}(\mathbf{x}) \end{bmatrix}$$
$$\mathbf{x} := \mathbf{x} + \mathbf{h}; \boldsymbol{\lambda} := \boldsymbol{\lambda} + \boldsymbol{\eta}, \tag{A.38}$$

Replacing $\boldsymbol{\eta}$ with $\boldsymbol{\mu} - \boldsymbol{\lambda}$ the equation system becomes:

$$\begin{bmatrix} \mathbf{W} & -\mathbf{J}_c^T \\ -\mathbf{J}_c^T & \mathbf{0} \end{bmatrix} \begin{bmatrix} \mathbf{h} \\ \boldsymbol{\mu} - \boldsymbol{\lambda} \end{bmatrix} = - \begin{bmatrix} f'(\mathbf{x}) - \mathbf{J}_c^T \boldsymbol{\lambda} \\ -\mathbf{c}(\mathbf{x}) \end{bmatrix}$$
$$\Leftrightarrow \begin{bmatrix} \mathbf{W} & -\mathbf{J}_c^T \\ -\mathbf{J}_c^T & \mathbf{0} \end{bmatrix} \begin{bmatrix} \mathbf{h} \\ \boldsymbol{\mu} \end{bmatrix} + \begin{bmatrix} \mathbf{J}_c^T \boldsymbol{\lambda} \\ \mathbf{0} \end{bmatrix} = - \begin{bmatrix} f'(\mathbf{x}) \\ -\mathbf{c}(\mathbf{x}) \end{bmatrix} + \begin{bmatrix} \mathbf{J}_c^T \boldsymbol{\lambda}) \\ \mathbf{0} \end{bmatrix} \tag{A.39}$$

$$\begin{bmatrix} \mathbf{W} & -\mathbf{J}_c^T \\ -\mathbf{J}_c^T & \mathbf{0} \end{bmatrix} \begin{bmatrix} \mathbf{h} \\ \boldsymbol{\mu} \end{bmatrix} = - \begin{bmatrix} f'(\mathbf{x}) \\ -\mathbf{c}(\mathbf{x}) \end{bmatrix}$$
$$\mathbf{x} := \mathbf{x} + \mathbf{h} \tag{A.40}$$

APPENDIX

B

LIST OF ABREVIATIONS

B.1. Medical Terms

HCC	Hepatocellular Carcinoma
RFA	Radiofrequency Ablation
TACE	Transarterial Chemoembolization

B.2. Medical Imaging Modalities & Medical File Format

CT	Computed Tomography
CT-fluoro	CT fluoroscopy
iMRI	interventional Magnetic Resonance Imaging
MRI	Magnetic Resonance Imaging
US	Ultrasound
DICOM	Digital Imaging and Communications in Medicine

B.3. Similarity Measures

AIF	Adaptive Interaction Function
AM-estimator	Annealing M-estimator
M-estimators	Maximum likelihood estimators
SSD	Sum of Squared Differences

B.4. Mathematical Terms

DOF	Degree of Freedom
GNC	Graduated Non-Convexity
H	Hessian
g	Gradient
J	Jacobian
MST	Minimal Spanning Tree
RMS	Root Mean Square
$\mathbb{SE}(3)$	Special Euclidean Group
$\mathfrak{se}(3)$	Lie Algebra
$\mathbb{SO}(3)$	Special Orthogonal Group
SLERP	Spherical Linear Interpolation
SQUAD	Spherical Cubic Interpolation
TSP	Travelling Salesman Problem

B.5. Miscellaneous

CEP Cost Equivalent Projection

FOV Field of View

GT Ground Truth

VOI Volume of Interest

APPENDIX

C

LIST OF PUBLICATIONS

i. Ruxandra Micu, Tobias Jakobs, Martin Urschler, and Nassir Navab, *A new registration/ visualization paradigm for ct-fluoroscopy guided rf liver ablation.* In J. Sporring R. Larsen, M. Nielsen, editor, Proc. Intl Conf.Medical Image Computing and Computer Assisted Intervention, volume 4190 of Lecture Notes in Computer Science, pages 882-890, 2006.

ii. Ruxandra Micu, Tobias Jakobs, Christoph J. Zech, Nassir Navab, *Subvolume Visualization based on piece-wise 2D-3D Registration*, in 5. Jahrestagung der Deutschen Gesellschaft für Computer-und Roboter-Assistierte Chirurgie (CURAC 2006), Hannover, Germany, October 2006.

iii. Ruxandra Micu, Tobias Jakobs, Christoph J. Zech, Nassir Navab, *Evaluation of different subvolume visualizations in CT-Fluoroscopy guided RF Liver Ablation*, SPIE Medical Imaging 2007, in Medical Imaging 2007: Visualization and Image-Guided Procedures, K. R. Cleary and M. I. Miga, eds., Proceedings of SPIE, San Diego, California, USA, February 2007, volume 6509, pages 51–57.

iv. Ruxandra Lasowski, Selim Benhimane, Jakob Vogel, Tobias F. Jakobs, Christoph J. Zech, Christoph Trumm, Christian Clason, Nassir Navab, *Adaptive visualization for needle guidance in RF Liver Ablation: taking organ deformation into account*, SPIE Medical Imaging 2008, in Medical Imaging 2008: Visualization and Image-Guided Procedures, K. R. Cleary and M. I. Miga, eds., Proceedings of SPIE, San Diego, California, USA, February 2008 (to appear).

v. Ruxandra Lasowski, Selim Benhimane, Jakob Vogel, Tobias F. Jakobs, Christoph J. Zech, Christoph Trumm, Nassir Navab, *Adaptive visualization using the annealing M-estimator*, in Bildverarbeitung für die Medizin 2008, A. Horsch, T. M. Deserno, H. Handels, H.-P. Meinzer, and T. Tolxdoff, eds., Informatik aktuell, Springer Verlag, March 2008

LIST OF FIGURES

LIST OF TABLES

BIBLIOGRAPHY

[1] J. Baker, *An algorithm for the location of transition states*, J. Comput. Chem., 7 (1986), pp. 385–395.

[2] S. Benameur, M. Mignotte, S. Parent, H. Labelle, W. Skallie, and J. de Guise, *3d/2d registration and segmentation of scoliotic vertebrae using statistical models*, Computerized Medical Imaging and Graphics, 27 (2003), pp. 321–337.

[3] F. V. Berghen, *CONDOR: a constrained, non-linear, derivative-free parallel optimizer for continuous, high computing load, noisy objective functions*, PhD thesis, Universite Libre de Bruxelles, 2004.

[4] S. H. Bernhard, *Exploring potential energy surfaces for chemical reactions: An overview of some practical methods*, Journal of computational chemistry, 24 (2001), pp. 1514–1527.

[5] W. Birkfellner, M. Figl, and H. Bergmann, *Stochastic rank correlation for slice-to-volume registration of fluoroct/ct imaging*, in Proceedings of SPIE, Medical Imaging 2007: Visualization, Image-Guided Procedures, and Display, vol. 6509, 2007, pp. 371–375.

[6] W. Birkfellner, M. Figl, J. Kettenbach, J. Hummel, P. Homolka, R. Schernthaner, T. Nau, and H. Bergmann, *Rigid 2D/3D slice-to-volume registration and its application on fluoroscopic CT images*, Med. Phys., 34 (2007), pp. 246–255.

[7] M. Birth, P. Hildebrand, M. Kleemann, and H.-P. Bruch, *Interventionelle therapie von lebermetastasen*, Chir. Gastroenterol, 19 (2003), pp. 349–358.

[8] J. Blackall, G. Penney, A. King, and D. Hawkes, *Alignment of sparse freehand 3-D ultrasound with preoperative images of the liver using models of respiratory motion and deformation*, IEEE Transactions on Medical Imaging (TMI), 24 (2005), pp. 1405–1416.

[9] J. M. Blackall, *Respiratory Motion in Image-Guided Interventions of the Liver*, PhD thesis, King's College London, September 2002.

[10] A. Blake and A. Zisserman, *Visual Reconstruction*, MIT Press, Cambridge, Massachusetts, 1987.

[11] M. Blum, R. Floyd, V. Pratt, R. Rivest, and R. Tarjan, *Time bounds for selection*, I Journal of Computer and System Sciences, 7 (1972), pp. 448–461.

[12] Y. Boykov and G. Funka-Lea, *Graph cuts and efficient n-d image segmentation*, International Journal of Computer Vision (IJCV), 70 (2006), pp. 109–131.

[13] D. E. Breen, *Cost minimization for animated geometric models in computer graphics*, The Journal of Visualization and Computer Animation, 8 (1997), pp. 201–220.

[14] L. G. Brown, *A survey of image registration techniques*, ACM Computing Surveys, 24 (2003), pp. 325–376.

[15] A. Can, C. V. Stewart, B. Roysam, and H. L. Tanenbaum, *A feature-based, robust, hierarchical algorithm for registering pairs of images of the curved human retina*, IEEE Trans. Pattern Analysis Machine Intelligence, 24 (2002), pp. 347–364.

[16] D. M. Cash, T. K. Sinha, C.-C. Chen, B. M. Dawant, W. C. Chapman, M. I. Miga, and R. L. Galloway, Jr., *Identification of deformation using invariant surface information*, in Medical Imaging 2004: Visualization, Image-Guided Procedures, and Display, R. L. Galloway, Jr., ed., vol. 5367 of Presented at the Society of Photo-Optical Instrumentation Engineers (SPIE) Conference, May 2004, pp. 140–150.

[17] A. G. Chandler, T. Netsch, C. A. Cocosco, J. A. Schnabel, and D. J. Hawkes, *Slice-to-volume registration using mutual information between probabilistic image classifications*, in Proceedings of SPIE, Medical Imaging 2004: Visualization, Image-Guided Procedures, and Display, vol. 5370, Galloway, R.L., Jr. (ed.), 2004, pp. 1120–1129.

[18] T. E. Choe and I. Cohen, *Registration of multimodal fluorescein images sequence of the retina*, Proc. Int'l Conf. Comp. Vision (ICCV), 1 (2005), pp. 106 – 113.

[19] J. Clark and D. A. Holton, *A first look at graph theory*, World Scientific Publishing Co. Inc., Teaneck, NJ, 1991.

[20] S. Clasen, A. Boss, D. Schmidt, C. Schraml, J. Fritz, F. Schick, C. D. Claussen, and P. L. Pereira, *Mr-guided radiofrequency ablation*

in a 0.2-t open mr system: Technical success and technique effectiveness in 100 liver tumors, JOURNAL OF MAGNETIC RESONANCE IMAGING, 26 (2007), pp. 1043–1052.

[21] M. Clifford, F. Banovac, E. Levy, and K. Cleary, *Assessment of hepatic motion secondary to respiration for computer assisted interventions*, Computer Aided Surgery, 7 (2002), pp. 291–299.

[22] A. R. Conn, N. I. Gould, and P. L. Toint, *Trust-Region Methods*, MPS-SIAM, Philadelphia, US, 2000.

[23] C. Couinaud, *Le foie, etudes anatomiques et chirurgicales*, Masson & Cie, Paris, 1957.

[24] G. M. Crippen and H. A. Scheraga, *Minimization of polypeptide energy. xi. the method of gentlest ascent.*, Archives of Biochemistry and Biophysics, 144 (1971), pp. 462–466.

[25] E. Dam, M. Koch, and M. Lillholm, *Quaternions, interpolation and animation*, Tech. Report DIKU-TR-98/5, Department of Computer Science, University of Copenhagen, 1998.

[26] K. Daniilidis, *Hand-eye calibration using dual quaternions*, Journal of Robotics Research, 18 (1999), pp. 286–298.

[27] C. de Boor, *A practical guide to splines*, vol. 27 of Applied Mathematical Sciences, Springer-Verlag, New York, revised ed., 2001.

[28] E. W. Dijkstra, *A note on two problems in connexion with graphs*, Numerische Mathematik, 1 (1959), pp. 269–271.

[29] B. Fei, J. L. Duerk, D. T. Boll, J. S. Lewin, and D. L.Wilson, *Slice-to-volume registration and its potential application to interventional mri-guided radio-frequency thermal ablation of prostate cancer*, IEEE Transactions on Medical Imaging (TMI), 22 (2003), pp. 515–525.

[30] J. Feldmar, N. Ayache, and F. Betting, *3d-2d projective registration of free-form curves and surfaces*, in Proc. Int'l Conf. Comp. Vision (ICCV), vol. 20-23, IEEE, 1995, pp. 549–556.

[31] R. Fletcher, *Practical Methods of Optimization*, John Wiley, West Sussex, England, 2003.

[32] M. Fleute and S. Lavallee, *Nonrigid 3-d/2-d registration of images using statistical models*, in Proc. Int'l Conf. Medical Image Computing and Computer Assisted Intervention (MICCAI), London, UK, 1999, Springer, pp. 138–147.

[33] W. Forstner and E. Gulch, *A fast operator for detection and precise location of distinct points, corners and centres of circular features*, ISPRS Intercommission Conference on Fast Processing of Photogrammetric Data, (1987), pp. 281–305.

[34] M. Friedman, I. Mikityansky, A. Kam, S. Libutti, M. M. Walther, Z. Neeman, J. K. Locklin, and B. J. Wood, *Radiofrequency ablation of cancer*, CardioVascular and Interventional Radiology, (2004).

[35] M. R. Gallagher, *Multi-layer Perceptron Error Surfaces: Visualization, Structure and Modelling*, PhD thesis, University of Queensland, Australia, June 1999.

[36] P. E. Gill, W. Murray, and M. H. Wright, *Practical Optimization*, Academic Press, 1981.

[37] S. N. Goldberg and D. Dupuy, *Image-guided radiofrequency tumor ablation: Challenges and opportunities - part i*, J Vasc Interv Radiol, 12 (2001), pp. 1021 – 1032.

[38] N. I. M. Gould and S. Leyffer, *An introduction to algorithms for nonlinear optimization*, Tech. Report RAL-TR-2002-03 (revised), Computational Science and Engineering Department, Rutherford Appleton Laboratory, Oxfordshire, UK, April 2002.

[39] G. M. G.S. Androulakis and M. Vrahatis, *Geometry of learning: Visualizing the performance of neural network supervised training methods*, Nonlinear Analysis, Theory. Methods & Applications, 30 (1997), pp. 4539–4544,.

[40] J. Hajnal, D. Hawkes, and D. Hill, *Medical Image Registration*, CRC Press, 2001.

[41] C. Harris and M. Stephens, *A combined corner and edge detector*, in Alvey Vision Conference, 1988, pp. 147–152.

[42] T. Hartkens, D. Hill, A. Castellano-Smith, D. Hawkes, C. M. Jr., A. Martin, W. Hall, H. Liu, and C. Truwit, *Using points and surfaces to improve voxel-based non-rigid registration*, in Proc. Int'l Conf. Medical Image Computing and Computer Assisted Intervention (MICCAI), Lecture Notes in Computer Science, Springer, 2002, pp. 565–572.

[43] D. Hawkes, D. Barratt, J. Blackall, C. Chan, P. Edwards, K. Rhode, G. Penney, J. McClelland, and D. Hill, *Tissue deformation and shape models in image-guided interventions: a discussion paper*, Medical Image Analysis, 9 (2005), pp. 163–175.

[44] S. Heimann, S. Münzing, H. Meinzer, and I. Wolf, *A shape-guided deformable model with evolutionary algorithm initialization for 3d soft tissue*

segmentation, in Conference on Information Processing in Medical Imaging (IPMI), vol. 4584, Springer, 2007, pp. 1–12.

[45] T. Heimann, I. Wolf, and H.-P. Meinzer, *Active shape models for a fully automated 3d segmentation of the liver - an evaluation on clinical data*, in Proc. Int'l Conf. Medical Image Computing and Computer Assisted Intervention (MICCAI), Springer, 2006, pp. 41–48.

[46] J. H. Hipwell, G. P. Penney, T. C. Cox, J. V. Byrne, and D. J. Hawkes, *2d-3d intensity based registration of dsa and mra - a comparison of similarity measures*, in Proc. Int'l Conf. Medical Image Computing and Computer Assisted Intervention (MICCAI), vol. 2489 of Lecture Notes in Computer Science, Springer, 2002, pp. 501–508.

[47] J. Hladuvka, *Derivatives and Eigensystems for Volume-Data Analysis and Visualization*, PhD thesis, Technische Universität Wien, December 2001.

[48] D. K. Hoffman, R. S. Nord, and K. Ruedenberg, *Gradient extremals*, Theor Chim Acta, 69 (1986), pp. 265–279.

[49] M. Holden, D. L. G. Hill, E. R. E. Denton, J. M. Jarosz, T. C. S. Cox, T. Rohlfing, J. Goodey, and D. J. Hawkes, *Voxel similarity measures for 3-d serial mr brain image registration*, IEEE Transactions on Medical Imaging (TMI), 19 (2000), pp. 94 –102.

[50] N. Holzknecht, T. Helmberger, U. Schoepf, B. Ertl-Wagner, C. Kulinna, A. Stäbler, and M. Reiser, *Evaluation of an electromagnetic virtual target system (ct-guide) for interventional ct-guided procedures*, RöFo - Fortschritte auf dem Gebiet der Röntgenstrahlen und der Bildgebenden Verfahren, 173 (2001), pp. 612–618.

[51] L. Jangland and J. Persliden, *Evaluation of the optimization tool dose tutor: A phantom study*, in Int. Conf. of Medical Physics, 2005.

[52] P. Jannin, J. Fitzpatrick, D. Hawkes, X. Pennec, R. Shahidl, and M. Vannier, *Validation of medical image processing in image-guided therapy*, IEEE Transactions on Medical Imaging (TMI), 21 (2002), pp. 445 – 449.

[53] C. R. Johnson and A. R. Sanderson, *A next step: Visualizing errors and uncertainty*, IEEE Computer Graphics and Applications, 23 (2003), pp. 6–10.

[54] L. Jun and H. Peng-wei, *Smooth interpolation on homogeneous matrix groups for computer animation*, Journal of Zhejiang University, 7 (2006), pp. 1168–1177.

[55] L. Kavan, S. Collins, C. O'Sullivan, and J. Žára, *Dual quaternions for rigid transformation blending*, Tech. Report Technical report TCD-CS-2006-46, Department of Computer Science, Trinity College Dublin, 2006.

[56] L. Kavan, S. Collins, J. Žára, and C. O'Sullivan, *Skinning with dual quaternions*, in I3D '07: Proceedings of the 2007 symposium on Interactive 3D graphics and games, New York, NY, USA, 2007, ACM Press, pp. 39–46.

[57] A. Khamene, P. Bloch, W. Wein, M. Svatos, and F. Sauer, *Automatic registration of portal images and volumetric CT for patient positioning in radiation therapy*, Medical Image Analysis, (2006), pp. 96–112.

[58] S. Kirkpatric, C. D. Gellatt, and M. P. Vecchi, *Optimization by simulated annealing*, Science, 220 (1983), pp. 671–680.

[59] T. Kröger, I. Altrogge, T. Preusser, P. Pereira, D. Schmidt, A. Weihusen, and H. Peitgen, *Numerical simulation of radio frequency ablation with state dependent material parameters in three space dimensions*, in Proc. Int'l Conf. Medical Image Computing and Computer Assisted Intervention (MICCAI), vol. 4191 of Lecture Notes in Computer Science, Springer, 2004, pp. 380–388.

[60] J. Kruskal, *On the shortest spanning subtree and the traveling salesman problem*, IEEE Trans. Pattern Analysis Machine Intelligence, 7 (1956), pp. 48–50.

[61] R. Lasowski, S. Benhimane, J. Vogel, T. F. Jakobs, C. J. Zech, C. Trumm, M. Brokate, and N. Navab, *Adaptive visualization using the annealing m-estimator*, in Bildverarbeitung für die Medizin (BVM), 2008.

[62] R. Lasowski, S. Benhimane, J. Vogel, T. F. Jakobs, C. J. Zech, C. Trumm, C. Clason, and N. Navab, *Adaptive visualization for needle guidance in RF liver ablation: taking organ deformation into account*, in Proceedings of SPIE, Medical Imaging, 2008.

[63] S. Li, *Discontinuity adaptive mrf prior and robust statistics: A comparative study*, Image and Vision Computing, 13 (1995), pp. 227–233.

[64] S. Li, *Robustizing robust m-estimation using deterministic annealing*, Pattern Recognition, 29 (1996), pp. 159–166.

[65] S. Li, H. Wang, and W. Y. C. Soh, *Robust estimation of rotation angles from image sequences using the annealing m-estimator*, Journal of Mathematical Imaging and Vision, 8 (1998), pp. 181–192.

[66] C. Lundstrom, P. Ljung, A. Persson, and A. Ynnerman, *Uncertainty visualization in medical volume rendering using probabilistic animation*, Transactions on Visualization and Computer Graphics, 13 (2007), pp. 1648 – 1655.

[67] F. M., R. K., and S. H.S., *Radial basis functions with compact support for elastic registration of medical images*, Image and Vision Computing, 19 (2001), pp. 87–96.

[68] K. Madsen, H. B. Nielsen, and O. Tingleff, *Methods for non-linear least squares problems, 2nd ed.*, Apr. 2004.

[69] ——, *Optimization with constraints, 2nd ed.*, Mar. 2004.

[70] L. Maier-Hein, D. Maleike, J. Neuhaus, A. Franz, I. Wolf, and H. Meinzer, *Soft tissue navigation using needle-shaped markers: Evaluation of navigation aid tracking accuracy and ct registration*, in Proceedings of SPIE, Medical Imaging 2007: Visualization, Image-Guided Procedures, and Display, vol. 6509, 2007.

[71] L. Maier-Hein, S. Müller, F. Pianka, A. Seitel, B. Müller-Stich, C. Gutt, U. Rietdorf, G. Richter, H.-P. Meinzer, B. M. Schmied, and I.Wolf, *Invitro evaluation of a novel needlebased soft tissue navigation system with a respiratory liver motion simulator*, in Proceedings of SPIE, Medical Imaging 2004: Visualization, Image-Guided Procedures, and Display, vol. 6509, 2007.

[72] J. Maintz and M. Viergever, *A survey of medical image registration*, Medical Image Analysis, 2 (1998), pp. 1–36.

[73] R. A. McLaughlin, J. Hipwell, D. J. Hawkes, J. A. Noble, J. V. Byrne, and T. Cox, *A comparison of 2d-3d intensity-based registration and feature-based registration for neurointerventions*, in Proc. Int'l Conf. Medical Image Computing and Computer Assisted Intervention (MICCAI), vol. 2489 of Lecture Notes in Computer Science, Springer, 2002, pp. 517–524.

[74] R. Micu, T. Jakobs, M. Urschler, and N. Navab, *A new registration/visualization paradigm for CT-fluoroscopy guided RF liver ablation*, in Proc. Int'l Conf.Medical Image Computing and Computer Assisted Intervention, J. S. R. Larsen, M. Nielsen, ed., vol. 4190 of Lecture Notes in Computer Science, 2006, pp. 882–890.

[75] R. Micu, T. Jakobs, C. Zech, and N. Navab, *Evaluation of different subvolume visualizations in CT-fluoroscopy guided RF liver ablation*, in Proceedings of SPIE, Medical Imaging, vol. 6509, 2007, pp. 51–57.

[76] J. Modersitzki, *Numerical methods for image registration*, Oxford University Press, 2004.

[77] S. Nicolau, A. Garcia, X. Pennec, L. Soler, and N. Ayache, *Augmented reality guided radio-frequency tumor ablation*, Computer Animation and Virtual World (previously the Journal of Visualization & Computer Animation), (2004). in press.

[78] S. Nicolau, X. Pennec, L. Soler, and N. Ayache, *Evaluation of a new 3D/2D registration criterion for liver radio-frequencies guided by augmented reality*, in International Symposium on Surgery Simulation and Soft Tissue

Modeling (IS4TM'03), N. Ayache and H. Delingette, eds., vol. 2673 of Lecture Notes in Computer Science, Juan-les-Pins, France, 2003, INRIA Sophia Antipolis, Springer, pp. 270–283.

[79] S. Nicolau, X. Pennec, L. Soler, and N. Ayache, *An accuracy certified augmented reality system for therapy guidance*, in Proc. of the 8th European Conference on Computer Vision (ECCV 04), vol. 3023 of Lecture Notes in Computer Science, Prague, May 2004, Springer, pp. 79–91.

[80] S. Nicolau, X. Pennec, L. Soler, and N. Ayache, *A complete augmented reality guidance system for liver punctures: First clinical evaluation*, in Proc. Int'l Conf. Medical Image Computing and Computer Assisted Intervention (MICCAI), vol. 3749 of Lecture Notes in Computer Science, Springer, 2005, pp. 539–547.

[81] H. Nielsen, *Damping parameter in marquardts method*, Tech. Report IMM-REP-1999-05, IMM Department of mathematical modelling, Technical University of Denmark, Lyngby, Denmark, April 1999.

[82] C. Nikou, F. Heitz, and J. P. Armspach, *Robust voxel similarity metrics for the registration of dissimilar single and multimodal images*, Pattern Recognition, 32 (1999), pp. 1351–1368.

[83] A. T. Pang, C. M. Wittenbrink, and S. K. Lodha, *Approaches to uncertainty visualization*, The Visual Computer, 13 (1997), pp. 370–390.

[84] A. Patriciu, M. Awad, S. Solomon, M. Choti, D. Mazilu, L. Kavoussi, and D. Stoianovici, *Robotic assisted radio-frequency ablation of liver tumors randomized patient study*, in Proc. Int'l Conf. Medical Image Computing and Computer Assisted Intervention (MICCAI), vol. 3750 of Lecture Notes in Computer Science, Springer, 2005, pp. 526–533.

[85] A. Patriciu, S. Solomon, L. Kavoussi, and D. Stoianovici, *Robotic kidney and spine percutaneous procedures using a new laser-based ct registration method*, in Proc. Int'l Conf. Medical Image Computing and Computer Assisted Intervention (MICCAI), vol. 2208 of Lecture Notes in Computer Science, Springer, 2001, pp. 249–257.

[86] V. Pekar, E. Gladilin, and K. Rohr, *An adaptive irregular grid approach for 3-D deformable image registration*, Phys. Med. Biol., 51 (2006), pp. 361–377.

[87] G. Penney, J. Blackall, M. Hamady, T. Sabharwal, A. Adam, and D. Hawkes, *Registration of freehand 3d ultrasound and magnetic resonance liver images*, Medical Image Analysis, 8 (2004), pp. 81–91.

[88] G. P. Penney, P. G. Batchelor, D. L. G. Hill, and D. Hawkes, *Validation of a two- to three-dimensional registration algorithm for aligning*

preoperative ct images and intraoperative fluoroscopy images, Medical Physics, 28 (2001), pp. 1024–1032.

[89] G. P. Penney, J. Weese, J. A. Little, P. Desmedt, D. L. G. Hill, and D. J. Hawkes, *A comparision of similarity measures for use in 2d-3d medical image registration*, IEEE Transactions on Medical Imaging (TMI), 17 (1998), pp. 586–595.

[90] P. Pereira, J. Trübenbach, and D. Schmidt, *Radiofrequency ablation: Basic principles, techniques and challenges*, RöFo - Fortschritte auf dem Gebiet der Röntgenstrahlen und der Bildgebenden Verfahren, 175 (2003), pp. 20–27.

[91] A. Pitiot, G. Malandain, E. Bardinet, and P. Thompson, *Piecewise affine registration of biological images*, in Second International Workshop on Biomedical Image Registration WBIR'03, 2003.

[92] J. P. Pluim, J. A. Maintz, and M. A. Viergever, *Image registration by maximization of combined mutual information and gradient information*, IEEE Transactions on Medical Imaging (TMI), 19 (2000), pp. 1 – 6.

[93] W. Quapp, *Gradient extremals and valley floor bifurcations on potential energy surfaces*, Theor Chim Acta, 75 (1989), pp. 447–460.

[94] ——, *Searching for saddle points of potential energy surfaces by following a reduced gradient*, Journal of Computational Chemistry, 19 (1998), pp. 1087–1100.

[95] ——, *A valley following method*, Optimization, 52 (2003), pp. 317–331.

[96] B. Reitinger, A. Bornik, R. Beichel, and D. Schmalstieg, *Liver surgery planning using virtual reality*, IEEE Computer Graphics and Applications, 26 (2006), pp. 36–47.

[97] A. Roche, G. Malandain, N. Ayache, and S. Prima, *Towards a better comprehension of similarity measures used in medical image registration*, in Proc. Int'l Conf. Medical Image Computing and Computer Assisted Intervention (MICCAI), vol. 1679 of Lecture Notes in Computer Science, Springer, 1999, pp. 555–566.

[98] G. Rohde, A. Aldroubi, and B. Dawant, *The adaptive bases algorithm for intensity-based nonrigid image registration*, IEEE Transactions on Medical Imaging (TMI), 22 (2003), pp. 1470–1479.

[99] T. Rohlfing, C. R. M. Jr., W. O'Dell, and J. Zhong, *Modeling liver motion and deformation during the respiratory cycle using intensity-based nonrigid registration of gated mr images*, in Proceedings of SPIE, Medical Imaging, vol. 4319, 2001, pp. 337–348.

[100] T. Rohlfing, D. Russakoff, M. Murphy, and C. Maurer, *An intensity-based registration algorithm for probabilistic images and its application for 2d to 3d image registration*, in Proceedings of SPIE, Medical Imaging 2004: Visualization, Image-Guided Procedures, and Display, vol. 4684, Galloway, R.L., Jr. (ed.), 2002, pp. 581–591.

[101] D. Rueckert, L. Sonoda, C. Hayes, D. Hill, M. Leach, and D. Hawkes, *Nonrigid registration using free-form deformations: application to breast mr images*, IEEE Transactions on Medical Imaging (TMI), 18 (1999), pp. 712 – 721.

[102] N. V. Ruiter, *Registration of X-ray Mammograms and MR-Volumes*, PhD thesis, Universität Mannheim, October 2003.

[103] D. Russakoff, T. Rohlfing, A. Ho, D. Kim, R. Shahidi, J. J.R. Adler, and J. C. R. Maurer, *Evaluation of intensity-based 2d-3d spine image registration using clinical gold-standard data*, in Workshop on Biomedical Image Registration (WBIR), vol. 2717 of LNCS, 2003, pp. 151–160.

[104] D. A. Russakoff, T. Rohlfing, and C. R. M. Jr., *Fast intensity-based 2d-3d image registration of clinical data using light fields*, in Proc. Int'l Conf. Comp. Vision (ICCV), 2003.

[105] D. B. Russakoff, T. Rohlfing, R. Shahidi, D. H. Kim, J. R. A. Jr., and C. R. M. Jr., *Intensity-based 2d-3d spine image registration incorporating one fiducial marker*, in Proc. Int'l Conf. Medical Image Computing and Computer Assisted Intervention (MICCAI), vol. 2878 of Lecture Notes in Computer Science, Springer, 2003, pp. 287–294.

[106] O. Sadowsky, K. Ramamurthi, L. M. Ellingsen, G. Chintalapani, J. L. Prince, and R. H. Taylor, *Atlas-assisted tomography: Registration of a deformable atlas to compensate for limited-angle cone-beam trajectory*, in IEEE International Symposium on Biomedical Imaging (ISBI), 2006, pp. 1244 – 1247.

[107] M. Scheuering, *Fusion of Medical Video Images And Tomographic Volumes*, PhD thesis, Universität Erlangen-Nürnberg, May 2003.

[108] J. Shewchuk, *An introduction to the conjugate gradient method without the agonizing pain*, Tech. Report CMU-CS-94-125, School of Computer Science, Carnegie Mellon University, Pittsburgh, Philadelphia, March 1994.

[109] K. Shoemake, *Animating rotation with quaternion curves*, Siggraph, 19 (1985), pp. 245–254.

[110] A. L. Simpson, B. Ma, E. C. S. Chen, R. E. Ellis, and A. J. Stewart, *Using registration uncertainty visualization in a user study of a simple surgical task*, in Proc. Int'l Conf. Medical Image Computing and Computer Assisted

Intervention (MICCAI), vol. 4191 of Lecture Notes in Computer Science, 2006, pp. 397–404.

[111] C. Sminchisescu and B. Triggs, *Building roadmaps of minima and transitions in visual models*, Int'l J. of Comp. Vision, 61 (2005), pp. 81–101.

[112] C. V. Stewart, *Robust parameter estimation in computer vision*, SIAM Rev., 41 (1999), pp. 513–537.

[113] C. V. Stewart, C.-L. Tsai, and A. G. A. Perera, *A view-based approach to registration: Theory and application to vascular image registration*, in Conference on Information Processing in Medical Imaging (IPMI), 2003, pp. 475–486.

[114] T. S. Y. Tang and R. E. Ellis, *2d/3d deformable registration using a hybrid atlas*, in Proc. Int'l Conf. Medical Image Computing and Computer Assisted Intervention (MICCAI), vol. 3750 of Lecture Notes in Computer Science, Springer, 2005, pp. 223–230.

[115] J. P. Thirion, *Building roadmaps of minima and transitions in visual models*, Medical Image Analysis, 2 (1998), pp. 243–260.

[116] S. Ulzheimer and C. Leidecker, *Syngo explorer image reconstruction(ir) taskcard, bericht zur validierung der option 'addition von rauschen'*, VAMP Verfahren und Apparate der Medizinischen Physik, 8 (2004).

[117] M. Urschler and H. Bischof, *Assessing breathing motion by shape matching of lung and diaphragm surfaces*, in Proceedings of SPIE, Medical Imaging 2005: Visualization, Image-Guided Procedures, and Display, Galloway, R.L., Jr. (ed.), 2005, pp. 440–452.

[118] B. Vemuri, J. Yea, Y. Chen, and C. Leonard, *Image registration via level-set motion: Applications to atlas-based segmentation*, Medical Image Analysis, 7 (2003), pp. 1–20.

[119] V. Venkatraman, M. H. V. Horn, S. Weeks, and E. Bullitt, *Liver motion due to needle pressure, cardiac and respiratory motion during the tips procedure*, in Proc. Int'l Conf. Medical Image Computing and Computer Assisted Intervention (MICCAI), vol. 3217 of Lecture Notes in Computer Science, Springer, 2004, pp. 66–72.

[120] M. Vetter, I. Wolf, P. Hassenpflug, M. Hastenteufel, R. Ludwig, L. Grenacher, G. M. Richter, W. Uhl, M. W. Büchler, and H.-P. Meinzer, *Navigation aids and real-time deformation modeling for open liver surgery*, in Medical Imaging 2003: Visualization, Image-Guided Procedures, and Display. Edited by Galloway, Robert L., Jr. Proceedings of the SPIE, Volume 5029, pp. 58-68 (2003)., R. L. Galloway, Jr., ed., vol. 5029 of Presented

at the Society of Photo-Optical Instrumentation Engineers (SPIE) Conference, May 2003, pp. 58–68.

[121] von Siebenthal, M., G. Székely, U. Gamper, P. Boesiger, A. Lomax, and P. Cattin, *4D MR imaging of respiratory organ motion and its variability*, Phys. Med. Biol., 52 (2007), pp. 1547–1564.

[122] M. von Siebenthal, G. Székely, A. Lomax, and P. Cattin, *Systematic errors in respiratory gating due to intrafraction deformations of the liver*, Medical Physics, (2007).

[123] M. Walker, L. Shao, and R. Volz, *Estimating 3-d location parameters using dual number quaternions*, CVGIP: Image Understanding, 54 (1991), pp. 358–367.

[124] S. K. Warfield, A. Nabavi, T. Butz, K. Tuncali, S. G. Silverman, P. Black, F. A. Jolesz, and R. Kikinis, *Intraoperative segmentation and nonrigid registration for image guided therapy*, in Proc. Int'l Conf. Medical Image Computing and Computer Assisted Intervention (MICCAI), Springer, 2000, pp. 176–185.

[125] A. Weihusen, F. Ritter, T. Kröger, T. Preusser, S. Zidowitz, and H.-O. Peitgen, *Workflow oriented software support for image guided radiofrequency ablation of focal liver malignancies*, in Proceedings of SPIE, Medical Imaging 2004: Visualization, Image-Guided Procedures, and Display, vol. 6509, Galloway, R.L., Jr. (ed.), 2007, pp. 9191 – 9199.

[126] W. Wein, *Intensity based rigid 2d-3d registration algorithms for radiation therapy*, master's thesis, Technical University Munich, 2003.

[127] W. Wein, B. Röper, and N. Navab, *Automatic registration and fusion of ultrasound with CT for radiotherapy*, in MICCAI 2005 Proceedings, Lecture Notes in Computer Science, Springer, Oct. 2005.

[128] W. Wein, B. Röper, and N. Navab, *Integrating diagnostic B-mode ultrasonography into CT-based radiation treatment planning*, IEEE Transactions on Medical Imaging (TMI), 26 (2007), pp. 866–879.

[129] J. Wessling, R. Fischbach, R. Esseling, R. Raupach, and W. Heindel, *Effect of dose reduction and noise reduction filters on detection of liver lesions using multi-detector row ct*, in Proceedings of Radiological Society of North America (RSNA), 2005.

[130] S. Xu, G. Fichtinger, R. H. Taylor, and K. R. Cleary, *3d motion tracking of pulmonary lesions using ct fluoroscopy images for robotically assisted lung biopsy*, in Proceedings of SPIE, Medical Imaging 2004: Visualization, Image-Guided Procedures, and Display, vol. 5367, Galloway, R.L., Jr. (ed.), 2004, pp. 394–402.

[131] S. Xu, R. Taylor, G. Fichtinger, and K. Cleary, *Lung deformation estimation and four-dimensional ct lung reconstruction*, in Proc. Int'l Conf. Medical Image Computing and Computer Assisted Intervention (MICCAI), vol. 3750 of Lecture Notes in Computer Science, Springer, 2005, pp. 312–319.

[132] Z. Yaniv and K. Cleary, *Image-guided procedures: A review*, Tech. Report CAIMR TR-2006-3, Imaging Science and Information Systems Center, Departement of Radiology, Georgetown University Medical Center, 2006.

[133] Z. Yaniv, R. Stenzel, K. Cleary, and F. Banovac, *A realistic simulation framework for assessing deformable slice-to-volume (CT-fluoroscopy/CT) registration*, in Proceedings of SPIE, Medical Imaging, vol. 6141, 2006, pp. 116–123.

[134] J. Yao and R. Taylor, *Assessing accuracy factors in deformable 2d/3d medical image registration using a statistical pelvis model*, Proc. Int'l Conf. Comp. Vision (ICCV), 02 (2003), p. 1329.

[135] M. Zefran, V. Kumar, and C. Croke, *On the generation of smooth three-dimensional rigid body motions*, IEEE Trans. on Robotics and Automation, 14 (1998), pp. 576–589.

[136] D. Zikic, W. Wein, A. Khamene, D. Clevert, and N. Navab, *Fast deformable registration of 3d-ultrasound data using a variational approach*, in Proc. Int'l Conf. Medical Image Computing and Computer Assisted Intervention (MICCAI), vol. 4190 of Lecture Notes in Computer Science, 2006, pp. 915–923.

[137] B. Zitova and J. Flusser, *Image registration methods: a survey*, Image and Vision Computing, 21 (2003), pp. 977–1000.

[138] L. Zollei, E. Grimson, A. Norbash, and W. Wells, *2d-3d rigid registration of x-ray fluoroscopy and ct images using mutual information and sparsely sampled histogram estimators*, Proc. IEEE Conf. Computer Vision and Pattern Recognition (CVPR), 02 (2001), p. 696.